

Dielectric Characterization of Skin-Mimicking Phantoms in the Microwave Range: Towards a Diagnostic Tool for Skin Cancer

Jasmine Boparai



McGill

Department of Electrical & Computer Engineering
McGill University
Montréal, Québec, Canada

March 11, 2023

A thesis submitted to McGill University in partial fulfillment of the requirements of the degree of

Doctor of Philosophy

© 2023 Jasmine Boparai

Abstract

Skin cancer is the most common form of cancer in the world. A report by the skin cancer foundation estimates that one in five Americans will develop skin cancer by the age of 70. Melanoma, which is considered to be the deadliest type of skin cancer, causes the majority of fatalities. The other type is non-melanoma, which is further classified as basal cell carcinoma (BCC) and squamous cell carcinoma (SCC), affects millions of human lives every year.

Early-stage diagnosis of all skin cancers, including melanoma, results in a better prognosis and improved survival rate for the patient. The current method of diagnosis relies on the visual inspection and therefore, implicitly, on the skill and experience of the dermatologist. They inspect the color, size, shape, irregularities in borders, bleeding in lesions, or if lesion is raised or hard to touch. In case of a suspicious lesion, a biopsy is required, so that the sample can be tested in a cell pathology lab. These methods of visual inspection are vulnerable to human error and vary in interpretation according to the dermatologist's experience.

As a result, a significant research effort is underway to develop diagnostic tools for skin cancer. Due to the reported inherent difference in electrical properties between healthy and

cancerous tissues, microwave-based techniques hold promise for skin cancer detection.

Therefore, the main focus of this research is systematic design and development of experimental tissue-mimicking phantoms which are extensively required to check the viability and performance of the designed tools in a controlled laboratory environment and prior to *in vivo* trials. The thesis describes the mathematical modeling and construction of series of phantom models and comprehensive dielectric property characterization of skin and skin cancer tissue-mimicking phantoms by measuring their reflectance properties in the microwave region. In addition, the work contributes with the estimation of the Cole-Cole function parameters for experimental values that gives the best fit with the computed results. Sensing depth of the probe is quantified by realizing realistic phantoms of different thicknesses. Lastly, the dielectric probe was numerically simulated to estimate the specific absorption rate (SAR) in order to confirm the compliance with the safety standards.

Abrégé

Le cancer de la peau est la forme de cancer la plus répandue dans le monde. Un rapport de Skin Cancer Foundation estime qu'un Américain sur cinq développera un cancer de la peau avant l'âge de 70 ans. Le mélanome, qui est considéré comme le type de cancer de la peau le plus mortel, est à l'origine de la majorité des décès. L'autre type, le non-mélanome, qui se subdivise en carcinome basocellulaire (BCC) et en carcinome spinocellulaire (SCC), affecte des millions de vies humaines chaque année.

Le diagnostic précoce de tous les cancers de la peau, y compris le mélanome, permet d'améliorer le pronostic et le taux de survie du patient. La méthode actuelle de diagnostic repose sur l'inspection visuelle et donc, implicitement, sur les compétences et l'expérience du dermatologue. Il inspecte la couleur, la taille, la forme, les irrégularités des bords, les saignements dans les lésions, ou si les lésions sont en relief ou dures au toucher. En cas de lésion suspecte, une biopsie est nécessaire, afin que l'échantillon puisse être analysé dans un laboratoire de pathologie cellulaire. Ces méthodes d'inspection visuelle sont vulnérables à l'erreur humaine et leur interprétation varie en fonction de l'expérience du dermatologue.

C'est pourquoi un effort de recherche important est en cours pour développer des outils de diagnostic du cancer de la peau. En raison de la différence inhérente aux propriétés électriques entre les tissus sains et cancéreux, les techniques basées sur les micro-ondes sont prometteuses pour la détection et le diagnostic du cancer de la peau.

Par conséquent, l'objectif principal de cette recherche est la conception et le développement systématiques de fantômes expérimentaux imitant les tissus, qui sont largement nécessaires pour vérifier la viabilité et les performances de l'outil conçu dans un environnement de laboratoire contrôlé et avant les essais *in vivo*. La thèse décrit la modélisation mathématique et la construction d'une série de modèles de fantômes et la caractérisation complète des propriétés diélectriques de fantômes imitant les tissus de la peau et du cancer de la peau en mesurant leurs propriétés de réflectance dans la région des micro-ondes. En outre, le travail contribue à l'estimation des paramètres de la fonction Cole-Cole pour les valeurs expérimentales qui donnent le meilleur ajustement avec les résultats calculés. La profondeur de détection de la sonde est quantifiée en réalisant des fantômes réalistes de différentes épaisseurs. Enfin, la sonde diélectrique a été simulée numériquement pour estimer le débit d'absorption spécifique (DAS) afin de confirmer la conformité avec les normes de sécurité.

Acknowledgements

First and foremost, I would like to thank my supervisor and mentor, Prof. Milica Popović for her invaluable guidance, continuous support, and encouragement throughout my PhD. She has been an amazing supervisor, without whom this work would not have been possible. Her expert tips on written communication greatly improved my presentation and writing skills.

I am also grateful to Prof. Dennis Giannacopoulos and Prof. Sharmistha Bhadra for taking time to serve on my dissertation committee and for providing constructive feedbacks. A big thanks to Prof. Thomas Szkopek for giving me the opportunity to use his lab facility for phantom fabrication and to Prof. Emily Porter, who always answered my queries regarding the project. Further, I would also like to acknowledge my fellow PhD students Leonardo Fortaleza, Milad MokhtariSangdehi, Shangyang Shang for interesting discussions related to electromagnetics.

The research presented in this thesis was financially supported by McGill Engineering Doctoral Award (MEDA), Natural Sciences and Engineering Research Council of Canada

(NSERC) Discovery under grant (RGPIN-2019-05850) and by Collaborative Research and Development under grant (CRD 521870 – 17).

Special thanks to undergraduate students Rachel Tchinov, Oliver Miller, Yanis Jallouli, Leon Hovsep Baronijan, Yi Wei with whom I had a pleasure to work with, during their SURE summer internship.

Finally, I would like to express my deepest gratitude to my parents, in-laws, brother, husband and my dearest son-Sahir. I appreciate their incredible support and understanding during this period. It would be impossible for me to complete this work without their love. Special thanks to my maternal uncle Hardip Singh Bhatti and my dearest friend Bhupinder who were always there to give me push to work harder.

Contents

1	Introduction	1
1.1	Motivation	1
1.2	Thesis Contribution	4
1.2.1	List of Publications	6
1.3	Thesis Outline	9
2	Background	12
2.1	Skin Anatomy	13
2.1.1	Epidermis	13
2.1.2	Dermis	14
2.1.3	Subcutaneous Tissue	15
2.2	Skin Cancer	15
2.2.1	Non-melanoma	16
2.2.2	Melanoma	19

2.3	Dermoscopy and Clinical Diagnosis	21
2.4	Dielectric Properties	28
2.5	Measurement Techniques	31
2.5.1	Transmission Line Method	31
2.5.2	Open-Ended Coaxial Probe Method	32
2.5.3	Free-space Measurement Method	36
2.5.4	Resonant Cavity Method	36
2.6	Specific Absorption Rate	38
3	Dielectric Properties of Skin-Mimicking Tissue Models in the 5 – 20 GHz	
	Range	40
3.1	Introduction	43
3.2	Materials	43
3.3	Experimental Set-up	44
3.3.1	Calibration and Validation	44
3.3.2	Measurements of Dielectric Properties	45
3.4	Results	46
3.5	Conclusion	48
3.6	Acknowledgment	48
3.7	References	49

4	Development and Characterization of Skin Phantoms at Microwave Frequencies	51
4.1	Introduction	53
4.2	Materials and Procedures	57
4.2.1	Tissue-Mimicking Phantom Materials	57
4.2.2	Fabrication of Skin Phantoms with Tumor Inclusions	57
4.2.3	Measurement Setup and Procedure	60
4.2.4	Method	64
4.3	Results And Discussions	64
4.3.1	Experiment 1: Tumor in Align with Thick Skin Surface	65
4.3.2	Experiment 2: Tumor in Align with Thin Skin Surface	67
4.3.3	Experiment 3: Tumor Raised out of Thick and Thin Skin	68
4.3.4	Experiment 4: Tumor Inside Thick and Thin Skin	70
4.3.5	Experiment 5: Tumor with Irregular Border	72
4.4	Conclusion	77
4.5	Acknowledgment	78
4.6	References	79
5	Heterogeneous Skin Phantoms for Experimental Validation of Microwave-Based Diagnostic Tools	87
5.1	Introduction	89

5.2	Materials and Methods	93
5.2.1	Modeling of phantoms	93
5.2.2	Characterization Methodology	96
5.2.3	Results and Discussion	99
5.2.4	Study 1: Tumors Embedded within the Fat–Skin Layer—Liposarcoma	101
5.2.5	Study 2: Multiple-Lesion Arrangement on the Skin Surface	104
5.2.6	Study 3: Testing Two Skin Phantoms: Oil–Gelatin and Probingon AB	106
5.3	Conclusion	108
5.4	References	112
6	Numerical and Experimental Models of Melanoma Growth for Assessment of Microwave-Based Diagnostic Tool	120
6.1	Introduction	122
6.2	Materials and Methods	126
6.2.1	Tumor Progression Model	127
6.2.2	Phantom Design and Development	132
6.2.3	Measurement Set-up	134
6.3	Experimental Results and Discussion	138
6.3.1	Tumor profile across a linear segment	139
6.3.2	Tumor profile across the grid	142
6.4	Conclusion	144

6.5	Acknowledgment	146
7	Numerical Analysis of Characterized Skin Phantoms and SAR Evaluation	156
7.1	Introduction	157
7.2	Methodology	159
7.2.1	Simulation Setup and Permittivity Extraction	159
7.2.2	Probe Aperture Size Variation and SAR Evaluation	162
7.2.3	Results and Discussion	163
7.3	Conclusion	169
7.4	References	169
8	Conclusion and Future Work	172
8.1	Key Contributions	173
8.2	Discussion	175
8.3	Future Work	177

List of Figures

2.1	Skin anatomy: epidermis, dermis and subcutaneous layers [20].	14
2.2	Skin cancer cells: basal cells, squamous cells and melanocytes [28].	16
2.3	Basal Cell Carcinoma lesions [29].	18
2.4	Squamous Cell Carcinoma lesions [29].	19
2.5	Melanoma lesions [29].	20
2.6	Transmission line method for dielectric property measurement [58].	33
2.7	Coaxial probe method for measurement of dielectric properties [58].	34
2.8	Keysight N1501A (a) High temperature probe, (b) Slim form probes and (c) Performance probe [59]; Speag (e) DAK 12 (4 MHz – 3 GHz), (f) DAK 3.5 (200 MHz – 20 GHz), (g) DAK 1.2E (5 MHz – 67 GHz) [60].	35
2.9	Free-space method for measurement of the dielectric properties [58].	37
2.10	Resonant cavity system for measurement of dielectric properties [58].	38

3.1	Experimental Setup: Keysight performance probe with 2mm Probingon skin phantom and FieldFox vector network analyzer.	45
3.2	Relative permittivity of (a) Probingon phantom in 2 mm, 20 mm and 2 mm on carbon fat phantom. (b) Carbon-based phantom in 2 mm, 20 mm and 2 mm on carbon fat phantom.	46
3.3	Conductivity of (a) Probingon phantom in 2 mm, 20 mm and 2 mm on carbon fat phantom. (b) Carbon-based phantom in 2 mm, 20 mm and 2 mm on carbon fat phantom.	47
4.1	Illustration of each preparation step in the process of phantom fabrication: (a) Mixture of p-toluic acid and n-propanol in a beaker placed over the hot plate. (b) The resultant solution of mixture obtained in (a), deionized water and gelatin after heating. (c) Oil heated to 50 °C in a beaker over hot plate to which resultant solution from (b) is added. (d) Final mixture on adding formaldehyde and liquid surfactant to mixture obtained in (c). (e) Solidified heterogeneous phantoms shown in molds.	58
4.2	Sketch and photograph of skin phantom samples with: (a) tumor leveled with the surface of skin (b) tumor raised out of skin (c) subcutaneously located tumor. d and t are diameter and thickness of skin, d1 and h are diameter and thickness of tumor. t1 and t2 are thickness of Layers 1 and 2, respectively.	60

-
- 4.3 Photograph of fabricated gel-based tumors, indicating variation in size: 10, 8, 6, 4, and 2 mm. 61
- 4.4 Experimental Setup: On the left, material under test (MUT) is placed on scissor lift jack, over it is the performance probe, on right is the FieldFox handheld vector network analyzer which is connected to laptop for analyzing data. Probe and VNA are connected with coaxial cable. 63
- 4.5 Dielectric measurements of tumor in align with thick skin surface compared with reference BCC and SCC tissues [36]. (a) Real relative permittivity, and (b) conductivity of tumors measured at the center, (c) Real relative permittivity and (d) conductivity of tumors measured at the border. 66
- 4.6 Dielectric measurements of tumor in align with thin skin surface compared with reference BCC and SCC tissues [36]. (a) Real relative permittivity, and (b) conductivity of tumors measured at the center, (c) Real relative permittivity and (d) conductivity of tumors measured at the border. 69
- 4.7 Dielectric measurements of tumor raised out of skin compared with reference BCC and SCC tissues [36]. (a) Real relative permittivity, (b) conductivity of raised tumors with thick underlying skin, (c) real relative permittivity, and (d) conductivity of raised tumors with thin underlying skin. 71

4.8	Dielectric measurements of tumor inside the skin compared with reference BCC and SCC tissues [36]. (a) Real relative permittivity and (b) conductivity of tumors inside the thick skin (c) Real relative permittivity and (d) conductivity of tumors inside the thin skin.	73
4.9	Dielectric measurements of tumor with irregular border in thick and thin skin compared with reference BCC and SCC [36]. (a) Real relative permittivity and (b) conductivity measured at the center and border of tumor.	74
4.10	Comparison of dielectric properties of the measured skin and tumor phantoms (10 mm tumor, planarly aligned with, raised out and embedded inside skin) (a) real relative permittivity (b) conductivity.	76
5.1	Illustration of fabrication procedure for proposed oil–gelatin phantoms. . . .	93
5.2	Oil–gelatin phantoms, with sketches shown on the top and the top-view photograph on the bottom: (a) Tumor (10 mm) embedded in fat underneath the skin and (b) multiple tumors in skin.	95
5.3	Photograph (top view) of oil–gelatin tumor phantoms in (a–f) oil–gelatin and (g–l) Probingon AB skin. Two tumor sizes in three arrangements are shown: 10 mm diameter (a,g) raised out of skin; (c,i) aligned with the skin surface; (e,k) embedded within the skin; with the same arrangements are shown for the smaller 2 mm tumor in figures (b,h); (d,j); (f,l), respectively.	97

-
- 5.4 Dielectric measurement setup showing the open-ended performance coaxial probe (left) and a FieldFox vector network analyzer; material under test (MUT) is placed on scissor jack. 98
- 5.5 (a) Relative permittivity and (b) conductivity measurements of tumors present in the fat underneath the skin and adjoining skin compared with the reference BCC and fat data from [39,40]. For each phantom model, two tumor sizes are taken: 10 mm and 2 mm. 103
- 5.6 (a) Relative permittivity and (b) conductivity measurements at the center of each tumor, at the border of each tumor and in-between the tumors compared with the reference data from [39]. The diameter of both tumors is 10 mm. . . 105
- 5.7 (a) Relative permittivity and (b) conductivity measurements of tumors present in two types of skin: oil-gelatin and Probingon AB. The results are compared with the reference data from [39]. For each case, measurements are performed with two tumor sizes (10 mm and 2 mm in diameter) and the tumor is in alignment with the top surface of the skin. 107
- 5.8 (a) Relative permittivity and (b) conductivity measurements of tumors present in two types of skin: oil-gelatin and Probingon AB. The results are compared with the reference data from [39]. For each case, measurements are performed with two tumor sizes (10 mm and 2 mm in diameter) and the tumor is embedded within the skin. 109

5.9	(a) Relative permittivity and (b) conductivity measurements of tumors present in two types of skin: oil–gelatin and Probingon AB. The results are compared with the reference data from [39]. For each case, measurements are performed with two tumor sizes (10 mm and 2 mm in diameter) and the tumor is raised out of skin.	110
6.1	Schematic of stages of melanoma progression with respect to radial and vertical growth.	124
6.2	Model for the MIS tumor phantom.	128
6.3	General model for melanoma tumor progression.	128
6.4	MATLAB-generated progression plots of tumor with bimonthly radial and vertical growth.	130
6.5	(a) Fabricated skin phantom with tumor inclusion of diameter, $D = 6.5$ mm and thickness, $t = 2.2$ mm (b) Slim-form probe placed at the adjoining skin of tumor.	135
6.6	Schematic representation of measurement setup with inset of pictorial view of actual sample under test lying on manually adjustable XYZ-stage.	136
6.7	Measurements across the linear segment over the tumor.	140
6.8	Measured relative permittivity and conductivity of tumor with radial and vertical growth in Month 0 (a) and (b), Month 6 (c) and (d), Month 8 (e) and (f), Month 12 (g) and (h), Month 16 (i) and (j) and Month 22 (k) and (l).	142

6.9	Measurement of tumor profile along the points of a grid.	143
6.10	Dielectric permittivity (a) and conductivity maps (b) for suspected region in the Months 0, 6, 8, 12, 16 and 22.	145
7.1	Fabricated skin phantoms with thickness varying 0.5 – 5 mm with 0.5 mm increments and 8 mm thick control skin phantom (top left), 3D printed cylindrical molds (bottom) and skin mimicking material poured into 3D printed molds at final fabrication step (top right).	158
7.2	(a) Schematic geometry of the modeled probe in contact with the skin-fat sample under investigation and (b) dimensions (a is the radius of the inner conductor, b is the radius of the outer conductor) and material of the probe.	160
7.3	Measured (a) Relative Permittivity and (b) Conductivity variation as a function of frequency at varying skin phantom thicknesses placed on fat phantom.	164
7.4	Simulated (a) Relative Permittivity and (b) Conductivity variation as a function of frequency at varying skin phantom thicknesses placed on fat phantom.	165
7.5	Maximum 1-g average Specific Absorbance Rate (SAR) for the input power of -10 dBm as a function of frequency in the tissue for different probe sizes. .	167

7.6 E -field distribution (V m^{-1}) at 15 GHz for the input power of -10 dBm inside the tissue for different probe sizes: (a) small probe, (b) medium probe and (c) large probe. 168

List of Tables

2.1	Clark’s classification of level of invasion of melanoma [35]	21
2.2	Summary of research work done in skin cancer detection at microwave and millimeter waves	27
4.1	Ingredients used in the proposed phantoms [37]	59
4.2	Experiments summary	62
4.3	Uncertainty budget of measured dielectric properties of deionized water . . .	63
4.4	One pole cole-cole parameters to compute dielectric measurements of reference data [36]	65
4.5	Cole-cole parameters of the dielectric properties of the fabricated phantoms .	75
5.1	A summary of steps for constructing oil-in-gelatin-based phantoms.	94
5.2	Composition used in the fabrication of phantoms shown in Fig. 5.2 [31]. . . .	96
5.3	One pole cole-cole parameters to compute dielectric data of malignant BCC and fat from literature.	100

6.1	Tumor progression: biological and physiological parameters	131
6.2	MATLAB generated theoretical set of bimonthly tumor phantoms	132
6.3	Dimensions of the proposed melanoma tumor phantoms	135
7.1	Probe dimensions for parametric analysis.	162

List of Acronyms

BCC	Basal Cell Carcinoma
SCC	Squamous Cell Carcinoma
CT	Computed Tomography
MRI	Magnetic Resonance Imaging
SAR	Specific Absorption Rate
SSM	Superficial Spreading Melanoma
NM	Nodular Melanoma
ALM	Acral Lentiginous Melanoma
LMM	Lentigo Maligna Melanoma
AJCC	American Joint Committee on Cancer
CAD	Computer Aided Diagnostic

CNN	Convolutional Neural Networks
OCT	Optical Coherence Tomography
NRW	Nicholson Ross Weir
NIST	National Institute of Standards and Technology
ANSI	American National Standards Institute
IEEE	The Institute of Electrical and Electronics Engineers
ICNIRP	The International Commission on Non-Ionizing Radiation Protection
FCC	Federal Communications Commission
MM	Malignant Melanoma
VNA	Vector Network Analyzer
MIS	Melanoma in-situ
ROG	Rate of Growth
HFSS	High-Frequency Structure Simulator
FEM	Finite Element Method

Chapter 1

Introduction

1.1 Motivation

More than 3 million people are affected by non-melanoma skin cancer, including basal cell carcinoma (BCC) and squamous cell carcinoma (SCC) each year, and 197,700 melanoma skin cancer (of which approximately 50% are invasive), are estimated to be diagnosed in 2022 in United States, as per American Cancer Society [1–3]. Though melanoma accounts for only 1% of all skin cancer cases, it is the leading cause of deaths with an estimate of 7,650 people dying in 2022 [1]. Over the past years, the skin cancer rate has been increasing rapidly [2].

Identification of skin cancer at early stage, before metastasis occurs, is a key for successful treatment and reduced mortality rate [4,5]. This is facilitated by various screening programs

that include visual skin examination at clinic. As per the U.S. preventive service task force, there is not sufficient evidence to recommend for or against routine screening for early detection of skin cancer [6, 7]. Moreover, visual inspection is not completely reliable as it depends on the experience of the physician, particularly in the case when the tumor grows in depth [8]. In that case, biopsy, followed by histology and pathology examinations are considered to be gold standards for diagnosis of skin cancer. These processes sometimes delay the treatment which can be fatal for the patient. Furthermore, with patients having several abnormal looking moles, it is almost impractical to do surgical excisions of each lesion for the determination of its malignancy [9]. Several techniques such as X-rays, MRIs, CT scans are also used to aid the dermatologists, but these have their own disadvantages. X-rays and CT scans uses harmful ionizing radiations and MRI is expensive [10, 11].

A more objective way of discriminating healthy skin from the cancerous one, is to utilize the dielectric contrast between healthy and malignant tissues, which forms the basis of microwave detection techniques [12]. This difference in the dielectric properties is due to the water content in the tissues which is higher in cancerous cells than normal tissues, as reported by various studies [13]. Microwave techniques are increasingly researched in a number of biomedical applications (detection of breast cancer, lung cancer, brain stroke) due to their numerous advantages such as use of non-ionizing radiation, low cost and non-invasive nature [14–16]. The development and performance evaluation of microwave-based skin cancer diagnostic modalities require experimental phantom sets

before doing experiments with volunteers. Thus, the overall aim of the research presented in this thesis is to design, model and characterize a substantial set of phantoms representing multiple scenarios and conditions to analyze the sensitivity of a microwave-based skin cancer diagnostic device. This work mainly focuses on the following specific objectives:

- Consistent comparison of fabricated and commercially obtained skin phantoms for providing guidance for selection of skin phantom depending on the anticipated dielectric properties, ease of fabrication and cost.
- Systematic development and characterization of multiple experimental skin phantoms with tumor inclusions realizing different scenarios such as an increment in tumor size, variation in location and shape of the tumor and representation of some rare conditions such as liposarcoma and non syndromic multiple basal cell carcinoma, for successful performance evaluation of emerging microwave skin cancer diagnostic prototypes.
- Mathematical modeling of the radial and vertical growth of a melanoma tumor at set time intervals and following the model, development and evaluation of phantom models for dielectric properties variation in respect to variation in the radial and vertical size of tumor.
- Extensive investigation of the impact of skin thickness variation on dielectric properties measurements and estimation of the sensing depth of the dielectric probe.

- Numerical modeling of a probe for comparative analysis of simulated and measured results obtained with skin thickness variation experiments and evaluation of SAR values.

1.2 Thesis Contribution

The primary contributions of the work presented in this thesis are outlined in the following section.

1. Two types of fabricated and one type of commercially procured phantom were characterized and compared with three different configurations. The comparison was done to provide common ground to weigh pro's and con's of these phantoms in terms of fabrication procedure, complexity and stability for repeated measurements.
2. A new set of skin phantoms was fabricated with tumor inclusions in a range of geometrical arrangements. A substantial set of anatomically and dielectrically realistic skin phantoms with variation in tumor sizes, locations and border irregularities were realized that can aid in identifying the detection limits and sensitivity of the emerging microwave based diagnostic prototypes. Phantoms representing malignant skin lesions such as liposarcoma and nonsyndromic multiple basal cell carcinoma were also developed yielding insight into factors that could affect the performance of diagnostic and detection tools. The measured results were then

- successfully validated with reference values obtained from literature.
3. Another outcome of my research is the development of a malignant melanoma tumor progression model. Malignant melanoma is associated with two growth patterns: a radial growth phase and a vertical growth phase which can be described by sequential stages of tumor progression. For accurate diagnosis of melanoma in a clinical setting, identification of both growth patterns is important. Therefore, a tumor progression model that quantitatively provides the radial and vertical growth of melanoma at set time intervals, is developed with the help of mathematical functions. Then following this model, oil-in-gelatin based phantom models were developed and characterized. Measurements indicate that the microwave-based techniques have the potential to distinguish malignant tissues from healthy tissues.
 4. Since skin thickness varies with a number of factors such as age, gender and most notably body location, the impact of skin thickness variation on dielectric properties measurements was extensively investigated by designing and developing phantom models with thickness ranging from 0.5 to 5 mm with 0.5 mm increments. The accurate thickness was achieved by designing and developing 3D printed molds. The sensing depth of the probe was also estimated.
 5. Lastly, numerical modeling of a dielectric probe was accomplished for comparison between simulated and measured results of experiments performed with thickness

variation and to observe the power deposited in a volume of tissues, the specific absorption rate (SAR) was estimated for the dielectric probe to confirm its compliance with the safety standards.

The contents of this thesis are based on the following papers published in peer-reviewed journals and conferences.

1.2.1 List of Publications

- [1] J. Boparai and M. Popović, “Heterogeneous Skin Phantoms for Experimental Validation of Microwave-Based Diagnostic Tools,” *Sensors*, vol. 22, no. 5, 2022, doi: 10.3390/s22051955.

I have contributed to all aspects of this research paper. Prof. Popović’s role in this publication was purely supervisory.

- [2] J. Boparai and M. Popović, “Development and Characterization of Skin Phantoms at Microwave Frequencies,” *IEEE Journal of Electromagnetics, RF and Microwaves in Medicine and Biology*, vol. 6, no. 3, pp. 296-304, September 2022.

I have contributed to all aspects of this research paper. Prof. Popović’s role in this publication was purely supervisory.

- [3] L. Kranold, J. Boparai, L. Fortaleza, M. Popović, “Skin Phantoms for Microwave Breast Cancer Detection: A Comparative Study,” *IEEE Journal of Electromagnetics,*

RF and Microwaves in Medicine and Biology, vol. 6, no. 2, pp. 175-181, June 2022, doi: 10.1109/JERM.2021.3084126.

I have contributed with dielectric measurements and data analysis of this research paper. Ms. Kranold and Mr. Fortaleza contributed during phantom construction and dielectric measurements. Prof. Popović's role in this publication was purely supervisory.

- [4] J. Boparai, Y. Jallouli, O. Miller, R. Tchinov and M. Popović, "Microwave Characterization and Probe Sensing: Parametric Study with Skin Phantom Thickness," *2022 IEEE MTT-S International Microwave Biomedical Conference (IMBioC)*, 16-18 May 2022, pp. 138-140, doi: 10.1109/IMBioC52515.2022.9790129.

I have contributed to all aspects of this research paper. Y. Jallouli contributed to phantom fabrication, dielectric measurements, and data analysis. O. Miller fabricated 3D printed molds and contributed during phantom fabrication. R. Tchinov performed literature review and phantom fabrication. Prof. Popović's role in this publication was purely supervisory.

- [5] L. Kranold, J. Boparai, L. Fortaleza, and M. Popović, "Comparative Study of Tissue-Mimicking Phantoms for Microwave Breast Cancer Screening Systems," *2020 IEEE MTT-S International Microwave Biomedical Conference (IMBioC)*, 14-17 December 2020, pp. 1-3, doi: 10.1109/IMBioC47321.2020.9385029.

I have contributed with dielectric measurements and data analysis of this research paper. Ms. Kranold and Mr. Fortaleza contributed during phantom construction and dielectric measurements. Prof. Popović's role in this publication was purely supervisory.

- [6] L. Kranold, J. Boparai, L. Fortaleza, and M. Popović, "A Comparative Study of Skin Phantoms for Microwave Applications," *2020 42nd Annual International Conference of the IEEE Engineering in Medicine & Biology Society (EMBC)*, 20-24 July 2020, pp. 4462-4465, doi: 10.1109/EMBC44109.2020.9175857.

I have contributed with dielectric measurements, data analysis, writing and presentation of this research paper. Ms. Kranold and Mr. Fortaleza contributed during phantom construction and dielectric measurements. Prof. Milica Popović role in the publication was purely supervisory.

- [7] J. Boparai, L. Kranold, L. Fortaleza, and M. Popović, "Dielectric Properties of Skin-Mimicking Tissue Models in the 5 – 20 GHz Range," *2020 IEEE International Symposium on Antennas and Propagation and North American Radio Science Meeting*, 5-10 July 2020, pp. 1623-1624, doi:10.1109/IEEECONF35879.2020.9329585.

I have contributed to all aspects of this research paper. Ms. Kranold and Mr. Fortaleza contributed during phantom construction and dielectric measurements. Prof. Popović's role in this publication was purely supervisory.

- [8] J. Boparai*, R. Tchinov*, O. Miller, Y. Jallouli and M. Popović, “Numerical and Experimental Models of Melanoma Growth for Assessment of Microwave-Based Diagnostic Tool,” in submission to the *IEEE Transactions on Biomedical Engineering*.

Rachel Tchinov, with whom I share the first co-authorship of this manuscript, contributed with the mathematical and theoretical model for tumor progression. I coordinated this with efforts of the rest of the team to design an experiment that will follow this model, and allow for spectroscopy of mimicked tumor progression.

- [9] J. Boparai, Y. Wei, M. Mokhtari and M. Popović, “Numerical Analysis of Characterized Skin Phantoms and SAR Evaluation,” in submission to the *IEEE Microwave and Wireless Components Letters*.

I have contributed to all aspects of this research paper. Mr. Wei and Mr. Mokhtari contributed in the simulations of dielectric properties and SAR evaluation experiments. Prof. Popović’s role in this publication was purely supervisory.

1.3 Thesis Outline

This thesis includes eight chapters along with references. The thesis work is organised as follows:

Chapter 1 provides the context of this thesis that includes a brief summary of the

research background, challenges in the field of skin cancer diagnosis, motivation and objectives of the thesis. An overview of contributions and structure of the thesis is also presented.

Chapter 2 presents the detailed review of the background related to the presented work. This includes description of skin anatomy, skin cancer, current technologies available for the diagnosis of skin cancer, and various measurement techniques. The fundamentals of dielectric spectroscopy and concept of SAR is also presented.

Chapter 3 outlines the comparison of fabricated and commercially obtained skin mimicking phantoms. It explains the factors such as fabrication procedure, complexity, cost and stability on the basis of which, skin phantoms can be chosen for a particular application.

Chapter 4 presents the development and fabrication of an array of anatomically and dielectrically realistic phantom models with systematic variation in tumor sizes, location and shape, which has not been investigated in previous studies. The substantial set of developed phantoms can provide an excellent test domain for emerging prototypes for skin cancer diagnosis.

Chapter 5 presents the realization of phantoms simulating conditions like liposarcoma and nonsyndromic multiple basal cell carcinoma. Moreover, to realize a range of anatomically realistic scenarios and meaningful comparison of different

phantoms, cancer-mimicking tumors were inserted in two different skin types. Validation of the results with reference models of literature indicate that the fabricated models can be used for testing and validation of microwave skin cancer detection prototypes.

Chapter 6 demonstrates tumor progression models representing radial and vertical growth patterns of malignant melanoma. Using oil-in-gelatin based material compositions, phantom models were developed based on the mathematical model of tumor progression. These phantoms provide dielectric properties difference in between healthy and cancerous skin, with variation in tumor thickness and radial diameter, thus will provide a valuable platform for testing the medical systems.

Chapter 7 demonstrates the designing of phantoms with thickness variation from 0.5 to 5 mm with 5 mm increments to analyze the effect of thickness variation on dielectric properties measurements. This also provides an estimation of the sensing depth of the probe. Next, numerical modeling of a dielectric probe terminated with a skin-fat model was performed for comparative analysis of experimental and simulated results. It also shows computation of the Specific Absorption Value (SAR) of probe to see the influence of electromagnetic waves on the biological tissues.

Chapter 8 concludes the work presented in this thesis and discusses the main results. It then suggests promising directions for future work.

Chapter 2

Background

The knowledge of skin structure and composition is essential to assess the interaction of external electromagnetic fields with the human tissues. The invasion of cancer leads to variation in structural, physiological state (e.g. increase in water content) and biochemistry (e.g. change in metal concentration) of tissues. This knowledge is further useful in the design and development of tissue-mimicking phantoms for the analysis and validation of emerging microwave-based medical imaging and diagnostic systems. Moreover, interaction mechanisms of electromagnetic waves with biological systems provide information about the dielectric properties of the material.

The following section gives the brief overview of anatomy of skin, various types of skin cancers and fundamentals of dielectric properties. The current technologies and clinical practice for diagnosis of skin cancer, their limitations and various characterization techniques

are also presented in the background section of the thesis.

2.1 Skin Anatomy

The entire external surface of the human body is covered by the skin, which forms the largest body organ. This is the main interface where body interacts with the external environment. Skin protects internal organs from injuries, infections, ultraviolet radiation exposure and helps regulate temperature and fluid loss [17, 18]. Human skin is a complex structure consisting of two primary layers, epidermis and dermis layers which lie on a fatty subcutaneous layer (also known as the hypodermis or the subcutis layer) [19] as depicted in Fig. 2.1. Each layer has different composition and function. The thickness of skin varies based on several factors including age, gender and anatomical location [21–23]. Skin is thinnest on the eyelid and thickest (1 – 4 mm) on the palms of the hands and soles of the feet [24].

2.1.1 Epidermis

The epidermis is the outermost layer of the skin. This layer is primarily comprised of keratinocytes cells that produce a protein known as keratin which provides natural protection from external factors. Another type of cell in the epidermis are melanocytes cells. These generate a protein known as melanin whose function is to give color to the skin and it provides protection from the sun. There are two more types of cells located in the epidermis: the

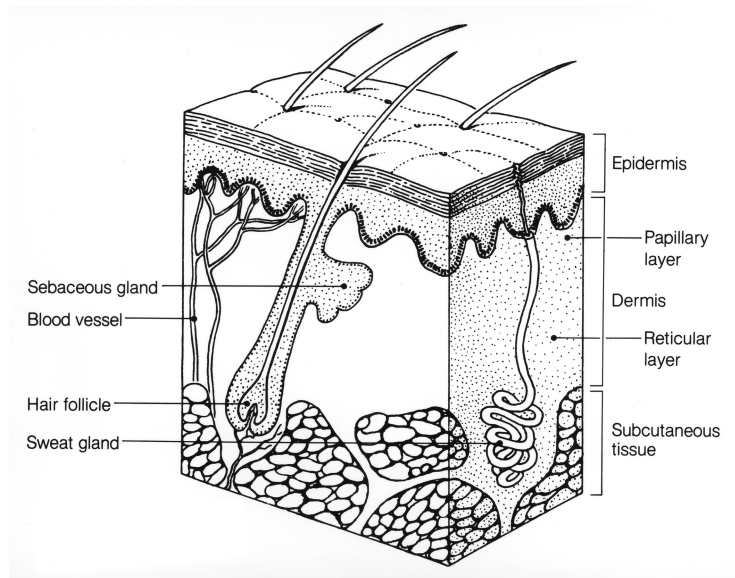


Fig. 2.1: Skin anatomy: epidermis, dermis and subcutaneous layers [20].

Merkel cells, which give sensory functions and Langerhans cells, that are a part of the immune system and help fight infections. The epidermis is divided into many sublayers. Stratum corneum is the surface layer, containing mainly flat dead cells and viable epidermis [25]. Stratum corneum has a low water content, which increases towards the inner epidermis [26].

2.1.2 Dermis

Right below the epidermis is the dermis layer, generally thicker than the epidermis layer. Its main composition is the dense network of collagen and elastin fibres whose function is to provide mechanical strength and elasticity to the skin. The dermis is composed of two layers: papillary dermis and reticular dermis. The papillary dermis layer lies directly under the epidermis and consists of elastic fibres and loose connective tissues which contain capillaries

and collagen. The reticular dermis is thick, having dense connective tissues containing larger blood vessels, coarse collagens and bundles of elastin fiber. This layer has special cells called fibroblasts which generate procollagen and elastin fiber and mast cells which moderate immune and inflammatory processes. Sebaceous glands, sweat glands, apocrine glands, mammary glands and hair follicles are also found deep within the dermis [25].

2.1.3 Subcutaneous Tissue

The deepest layer of the skin is the subcutaneous layer, made of fat cells and connective tissues. Fat protects muscles and bones from injuries acting as a shock absorber. It contains blood vessels and lymphatic vessels which connect the subcutis to the rest of the body [25].

2.2 Skin Cancer

Metastasis occurs when abnormal cells divide uncontrollably and spread to other parts of the body. Normally, new skin cells develop all the time to replace the older ones and their growth and multiplication occur in an orderly manner. If these cells grow out of control, they create a mass to which we refer as a “tumor”. Tumors can be of two types: **ab benign tumor**, usually not considered as a cancer since it remains limited to a few cell layers and does not attack other surrounding tissues and organs; on the other side, the **malignant tumor** spreads to other layers or organs [27]. Malignancy of skin can be classified into three

main types – basal cell carcinoma, squamous cell carcinoma and melanoma which is due to development of different types of cells of the epidermis: basal cells, squamous cells and melanocytes, respectively [28]. These cells are shown in Fig. 2.2.

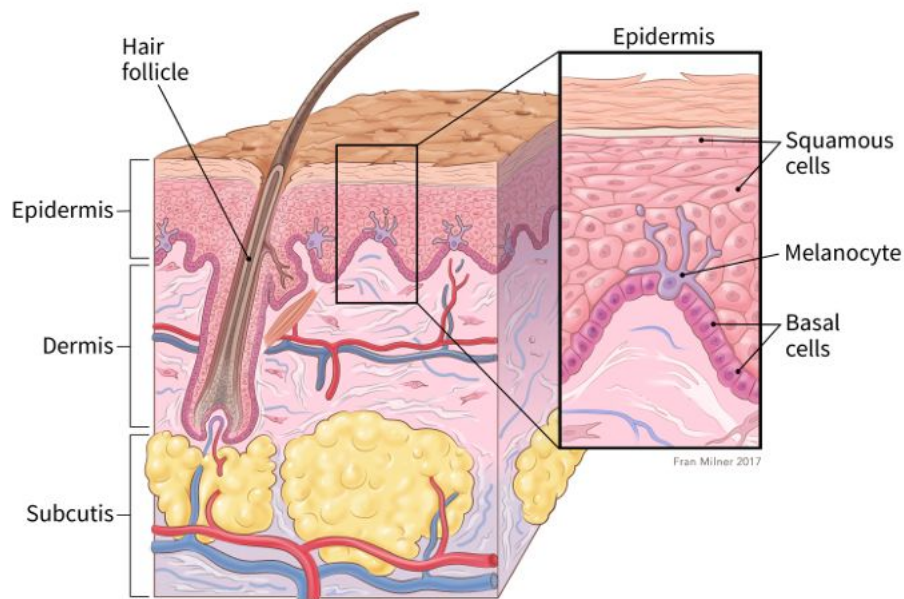


Fig. 2.2: Skin cancer cells: basal cells, squamous cells and melanocytes [28].

2.2.1 Non-melanoma

Skin cancer types such as basal cell carcinoma and squamous cell carcinoma are collectively known as non-melanoma skin cancer. Non-melanoma skin cancers are the most common form of skin cancers, which often begin in the epidermis layer of the skin. The incidence rate of non-melanoma skin cancer is continuously increasing [29].

Basal cell carcinoma (BCC) is the most prevalent form of skin cancer. This type of

cancer originates in the basal keratinocyte cells whose function is the new cell production. The growth of BCC is slow, and it rarely spreads beyond the original lesion site. But if they are not treated timely, they can locally invade and eventually cause disfigurement and degradation of surrounding skin by growing wider and deeper into the skin [30]. BCC usually develops on the sun-exposed areas like face, neck and head. Individuals having BCC can more easily develop other cancers like SCC and melanoma.

There are many subtypes of BCC depending upon the clinical appearance and history of the tumor. The first type is nodular BCC in which the tumor looks like a pimple, often bleeding, with inability to heal. There will be the formation of pit at the center of the tumor and border will remain translucent and pearl-colored. With further growth of the tumor, there could be severe tissue destruction. The second type is superficial BCC which looks like a pink or red patch of scaly skin and is often mistaken as eczema. This kind of tumor rarely bleeds and has raised borders. The third BCC type, with the appearance of a scar or plaque of scleroderma is known as Morpheaform BCC. It is very aggressive and can occur at any body location. Finally, infiltrative BCC is highly aggressive and leads to severe destruction. These lesions have high rate of recurrence and appear as flat, slightly raised and have irregular shape [30]. Some examples of basal cell carcinoma lesions are illustrated in the Fig. 2.3.

Squamous cell carcinoma (SCC) is the second most common type of non-melanoma skin cancer [31]. SCC arises in the flat cells that are located in the upper part of the



Fig. 2.3: Basal Cell Carcinoma lesions [29].

epidermis. SCC grows slowly but unlike other cancer types, it has a tendency to spread to the tissues, bones and nearby lymph nodes and could thus be life-threatening. SCC sometimes grows from precancerous skin growth named as actinic keratosis. This cancer is most common in people with fair skin due to sun exposure. Depending upon the size of the lesion, the invasion depth of the lesion, immunity of the patient, the location of the lesion, there is a high probability of recurrence of SCC. These tumors appear in numerous forms such as rough, flat, scaly or lumpy [32]. Some of the examples are illustrated in Fig. 2.4.



Fig. 2.4: Squamous Cell Carcinoma lesions [29].

2.2.2 Melanoma

Melanoma arises from abnormal growth of melanocytes, pigment-producing cells found in the epidermis. Melanoma is less common than other two types i.e., basal cell carcinoma and squamous cell carcinoma, but has more tendency to spread to other sites of the body. Melanoma is the leading cause of skin cancer fatality. Melanomas often start as benign lesions which are known as “nevi” or more commonly known as “moles”. Nevi are clusters of melanocytes surrounded by a matrix of connective tissues. When there is an abnormal growth of melanocytes, these non-cancerous nevi turn into cancerous melanoma. Melanoma tumors mainly appear as a brown or black lesion due to extra production of melanin by melanocytes [33], and are classified into types based on clinical and pathological features.

The first and the most common type is the superficial spreading melanoma (SSM). These tumors grow radially and can occur anywhere on the skin. They appear as raised tumors with brown color. The second one is nodular melanoma (NM) which can occur on all body regions and is often brown or black in color. These types of tumors grow quickly into the deeper layers of the skin. Acral lentiginous melanoma (ALM) are flat tumors that mainly develop on hands and feet while lentigo maligna melanoma (LMM) are mainly confined to the epidermis layer and are most commonly occurs on the face or neck of the individual [34]. Some of the examples are shown in Fig. 2.5.



Fig. 2.5: Melanoma lesions [29].

As long as melanocytes cells grow in the epidermis layer, melanoma is known to be in situ. When melanoma starts invading deeper layers it becomes invasive. To learn about the depth of invasion, cancerous tissue is excised and sent for histopathological analysis. There are two studies for measuring invasion depths: Breslow Depth and Clark Level [35,36].The

American Joint Committee on Cancer (AJCC) staging system has replaced the Breslow Depth. It gives the stage based on tumor type, node, metastasis (TMN) scores and other prognostic factors [37]. Clark assigned five levels for determination of the depth of invasion as illustrated in Table 2.1.

Table 2.1: Clark’s classification of level of invasion of melanoma [35]

Level	Anatomic Depth
Level 1	Melanoma confined to epidermis (in situ)
Level 2	Invasion into the papillary dermis
Level 3	Invasion to the junction of the papillary and reticular dermis
Level 4	Invasion into the reticular dermis
Level 5	Invasion into the subcutaneous fat

2.3 Dermoscopy and Clinical Diagnosis

Diagnosis of all types of skin cancers at early stages is important for effective and successful treatment and to increase the survival rate of patients. Visual inspection is the first step adopted by dermatologists for the clinical diagnosis of skin cancer. The diagnosis is performed following the ABCDE rule where the dermatologist looks at specific visual features. These are described as follows [38]:

- A is for asymmetry where one half of the mole does not look similar to the other half.
- B is for irregularity of the border of mole, i.e., the edges are ragged, blurred or irregular.

- C is for variability of color which means that the color of the mole is not the same all over but includes different shades.
- D is for diameter as if the mole is larger than 6 mm across, typically the size of a pencil eraser.
- E is for evolution, i.e., the mole is changing in shape, color or size.

However, this visual inspection varies with the experience of the dermatologist [13]. The accuracy of visual examination is further improved using dermoscopy [39]. Dermoscopy, which is also known as dermatoscopy, uses a magnifying lens for viewing the lesions but, again, it depends on the expertise of the practitioner. In the next step, on suspecting the lesion to be cancerous, the doctor calls for the biopsy and histopathological examination [10]. Biopsy is an invasive procedure which can lead to discomfort and anxiety of the patient and the histopathological procedure is time-consuming.

Computer-aided diagnostic (CAD) systems using convolutional neural networks (CNN) have recently been adopted for the diagnosis of skin cancer. These networks have high sensitivity, but specificity rates are low [40]. Numerous other technologies have been proposed such as optical coherence tomography (OCT), Reflectance confocal microscopy, ultrasonography, computed tomography (CT) and magnetic resonance imaging (MRI). OCT is not effective in producing quality images of lesions with crust and hyperkeratosis and also misdiagnoses the amelanotic melanoma for BCC. Ultrasonography has difficulty in

measurement of very thin and thick melanomas. Reflectance confocal microscopy requires expensive equipment and has limited depth of visualization [41]. CT tomography generates ionizing radiation and MRI is expensive [42].

Microwave techniques based on the dielectric contrast between healthy and malignant tissues have been widely explored in medical applications. Breast cancer detection utilizing microwave imaging techniques has been particular focus of interest since several years. A large-scale study was conducted by Lazebnik *et al.* [43] for determining the dielectric properties of several normal, benign and malignant breast tissues collected from cancer surgeries in the frequency range of 0.5 to 20 GHz using a coaxial probe. They observed the microwave dielectric contrast between normal adipose breast tissues and malignant tissues to be as large as 10:1 and between normal glandular/fibroconnective and malignant breast tissue to be not more than 10%. Sugitani *et al.* [44] presented report on dielectric properties of excised normal, malignant and adipose breast tissues for the frequency range of 0.5 – 20 GHz. They obtained tissue samples from cancer surgeries conducted on 35 patients whose age range was 33 – 88 years. They observed that variability in complex permittivity of tumorous samples depends on the volume fraction of cancerous cells existing in the volume measured. The microwave-based techniques have also been used for dielectric characterization of healthy and malignant colon, liver and lung tissue and utilized in other applications such as blood glucose monitoring, skin hydration evaluation and burn degree diagnosis. In 2016, Fornes-Leal *et al.* [45] characterized healthy and malignant *in*

vitro human colon tissues in 0.5 to 18 GHz frequency range with a coaxial probe. They performed excision surgery on 20 patients and obtained healthy and malignant colon tissues from them. They found that the relative permittivity of malignant tissues was significantly higher than healthy colon tissues. The average contrast observed between healthy and malignant tissues was computed to be 8.8% in terms of permittivity and 10.6% in terms of conductivity. Characterization of dielectric properties of *in vivo* and *ex vivo* normal, malignant and cirrhotic human was performed in the 0.5 – 20 GHz frequency band. It was observed that the differences in dielectric properties of *in vivo* and *ex vivo* normal and malignant liver tissues is not statistically significant. Only at frequencies 915 MHz, in case of *ex vivo*, difference of 28% was observed between normal and malignant tissues in terms of conductivity. While in case of *in vivo*, difference is 16% [46]. For detection of lung cancer, a frequency-domain microwave imaging algorithm was presented. The imaging system operating frequency was 1.5 – 3 GHz and artificial torso phantoms were taken for experiments. They validated the ability of device to detect lung cancer inserted into the torso phantom [15]. Choi *et al.* [47] presented a microwave noninvasive and continuous glucose monitoring sensor and its interference test. They compared their sensor with commercial sensors and found their sensor's performance to be encouraging. They validated their sensor with both *in vivo* and *in vitro* interference tests. The study [48] presents a wearable device based on microwave reflectometry technique for real-time skin hydration monitoring. They validated the system with numerical analysis and then

experimental tests were conducted. The investigation of dielectric properties of *in vivo* human skin was done using time-domain reflectometry method. They observed free water content of skin and applied this to the study of skin burns. They found that free water content gives good indication of skin health [49]. A number of researchers also utilized the principle of dielectric contrast between healthy and malignant tissues in skin cancer diagnostic applications at microwave and millimeter waves. Mehta *et al.* [5] investigated microwave reflectometry as a diagnostic tool for detection of skin cancer. Measurements were conducted on human subject's palm, wrist and forearm and they observed that technique is able to distinguish between benign and cancerous lesions. They also made an important observation that normal and cancerous tissues have different dielectric properties is due to difference in water content between them. In another work [50], reflection coefficients of BCC tumor samples taken from 15 cancer patients were measured using a customized WR-22 waveguide at frequency 42 GHz and 70 GHz. Large difference was observed between normal and cancerous skin tissues. For the study of reflection coefficients, they used large and flange probe and therefore the contact established between probe and skin tissues is not consistent leading to inconsistencies in measurements. Moreover, the measurements were performed on a small scale. In another work, Fritzi Topfer *et al.* [51] designed a near-field probe for diagnosis of small and shallow skin tumors in the frequency range of 75 – 110 GHz. They evaluated the performance of probe with phantoms such as micromachines silicon samples, agar-based samples and by doing *in vivo*

measurements on human skin and murine skin. It was observed that the probe was able to discriminate malignant melanoma tumors from healthy skin. The study has limitations as they employed small number of patients to evaluate the capability of probe. In addition, they consider only one type of cancer that is malignant melanoma. In [52], Mayrovitz *et al.* investigated if a handheld device at 300 MHz can differentiate between skin cancer lesions and non-cancerous lesions by doing *in vivo* dielectric constant measurements. The measurements were targeted on BCC and benign lesions. It was observed that BCC lesions have values 42.2% and non-cancerous lesions have 50.2% less than corresponding control skin. The study is limited to only BCC samples. In addition, frequency considered is lower which contradicts with other study, as according to other studies the higher frequency gives higher resolution. Moreover, with 300 MHz frequency, penetration depth would be very large and effect of underlying tissues will also be observed. A comprehensive study was performed by Amir Mirbeik *et al.* [40] on the dielectric properties of freshly excised BCC, SCC and adjacent healthy skin using slim-form open-ended coaxial probe over 0.5 – 50 GHz frequency range. They developed three stable and wideband oil-gelatin phantoms mimicking dielectric properties of malignant BCC, malignant SCC and normal human skin. They successfully delineate early-stage skin tumors with developed ultrahigh-resolution mm-wave imaging system. The limitation of this study is that they investigate only non-melanoma type of skin cancer and simple phantom models, while more sophisticated models are required to determine the feasibility of the system. Moreover, they did

measurements on excised samples which sometimes reported to be different in properties from *in vivo* tissues due to dehydration of sample, temperature difference, anesthesia. Summary of groups doing research in skin cancer detection at microwave and millimeter is given in Table 2.2.

Table 2.2: Summary of research work done in skin cancer detection at microwave and millimeter waves

Study	Frequency	Samples	Type	Probe	Remarks
Mehta <i>et al.</i> (2006)	0.3–6 GHz	Human skin (<i>in vivo</i>)	Normal, Benign, Melanoma	Coaxial	Small dataset was taken.
Taeb <i>et al.</i> (2013)	42 GHz, 70 GHz	Human skin (<i>in vivo</i>)	Normal, BCC	Waveguide	Probe uses flange which increases measurement inconsistencies
Fritzi Topfer <i>et al.</i> (2015)	75–110 GHz	Silicon samples, agar phantoms, human and murine skin (<i>in vivo</i>)	Malignant melanoma	Customized	One type of cancer was analyzed and small dataset is taken.
Mayrovitz <i>et al.</i> (2018)	300 MHz	Human skin (<i>in vivo</i>)	Normal, BCC	Sensor	At this frequency, penetration depth will be more and less resolution
Mirbeik <i>et al.</i> (2019)	0.5–50 GHz	Human skin (<i>ex vivo</i>), oil gelatin phantoms	Normal, BCC, SCC	Coaxial	Only non-malignant cancer type and excised samples are analyzed
This work	0.5–26.5 GHz	Oil-gelatin, Probingon AB, carbon polyurethane phantoms	Normal, BCC, SCC, malignant melanoma	Coaxial	Systematic testing with multiple geometrical configurations and different cancer types.

2.4 Dielectric Properties

The dielectric properties give a measure of the response of a specific biological tissue to electrical stimulation. In other words, dielectric properties give the information of how biological tissues interact with the applied electromagnetic waves. The dielectric properties are directly related to the water content, bulk density, structure, sodium and protein content of tissues and any pathological and physiological changes in the tissues can lead to variation in dielectric properties [13]. The dielectric properties of biological tissues are described in terms of complex permittivity, ε_r^* , which describes both magnitude and phase shift of the polarization on application of electric field. The real and the imaginary terms of the complex relative permittivity are given as:

$$\varepsilon_r^* = \varepsilon_r' - j\varepsilon_r'' \quad (2.1)$$

The real part of the complex permittivity, ε_r' is called the “dielectric constant” or “relative permittivity”. It expresses the measure of energy stored. The imaginary part of permittivity, ε_r'' is called the “loss factor”. It reflects the measure of energy loss. The conductivity, σ , is related to the imaginary part of the complex permittivity as:

$$\varepsilon_r'' = \frac{\sigma}{2\pi f \varepsilon_0} \quad (2.2)$$

f is the frequency (in Hz) and $\varepsilon_0 = 8.85 \times 10^{-12}$ F/m is the permittivity of free space. The relative complex permittivity of tissues is dependent on the frequency. The relative permittivity of tissues decreases, and conductivity increases with increase in frequency. Biological tissues exhibit various polarization mechanisms that result in relaxation processes, also known as dispersion phenomena in different frequency bands. There are three major dispersion regions α , β and γ and one minor dispersion region δ . The α -dispersion occurs at low frequencies, due to diffusion of ions at cell membranes of the tissues and is characterized by large permittivity values. The β -dispersion occurs at radio frequencies and is caused by capacitive charging of cellular membranes and due to dipolar orientation of tissue proteins and other organic macromolecules. The γ -dispersion happens due to relaxation of water molecules of tissues in the GHz frequency range. δ -dispersion occurs between β - and γ -dispersions, due to dipolar relaxation of bound water molecules.

Dielectric behavior of biological tissues is modeled using mathematical functions. With the help of these models, the measurement data points are reduced to form of equations and graphical representations. There are many models which describe the electrical behaviour of tissues such as Debye, Cole-Cole, and Cole-Davidson models. The dielectric response due to single polarization mechanism is the Debye model:

$$\varepsilon^* = \varepsilon_\infty + \frac{\varepsilon_s - \varepsilon_\infty}{1 + j\omega\tau}, \quad (2.3)$$

where ω and τ are angular frequency and time constant, respectively. The time constant

τ is related to the relaxation frequency f_c as $\tau = \frac{1}{2\pi f_c}$. ε_∞ is the permittivity at infinite frequencies and ε_s is the static permittivity at low frequency. In addition to the relaxation process, the static conductivity of tissue leads to dissipation of energy. These losses occur at lower frequencies and therefore as included in the Equation 2.3 as:

$$\varepsilon^* = \varepsilon_\infty + \frac{\varepsilon_s - \varepsilon_\infty}{1 + j\omega\tau} + \frac{\sigma_s}{j\omega\varepsilon_0} \quad (2.4)$$

The conductivity approaches to zero at infinite frequencies, therefore Equation 2.4 does not show the conductivity term at infinite frequencies.

The Cole-Cole model is a modified form of the Debye model, and is widely used to give physics-based representation of wideband frequency-dependent dielectric properties. An empirical variable α is added in the Cole-Cole first order equation to describe the statistical distribution of the relaxation time. The first order Cole-Cole equation is represented as:

$$\varepsilon^* = \varepsilon_\infty + \frac{\varepsilon_s - \varepsilon_\infty}{1 + (j\omega\tau)^{1-\alpha}}, \quad (0 < \alpha < 1) \quad (2.5)$$

And the Cole-Davidson model includes β empirical variable and expressed as:

$$\varepsilon^* = \varepsilon_\infty + \frac{\varepsilon_s - \varepsilon_\infty}{1 + (j\omega\tau)^\beta}, \quad (0 < \beta < 1) \quad (2.6)$$

All three models, Debye, Cole-Cole and Cole-Davidson, can be collectively given by the

Havriliak-Negami relaxation as follows:

$$\varepsilon^* = \varepsilon_\infty + \frac{\varepsilon_s - \varepsilon_\infty}{[1 + (j\omega\tau)^{1-\alpha}]^\beta}, \quad (0 < \alpha < 1), (0 < \beta < 1) \quad (2.7)$$

Havriliak-Negami accounts for asymmetry and broadness of dielectric dispersion curve. Multiple Cole-Cole dispersions are generally used to describe dielectric properties of biological tissues [53, 54].

2.5 Measurement Techniques

A number of methods have been developed for the characterization of biological tissues in the microwave frequency range. Based on the implemented measurement structure, these techniques are classified as transmission line, coaxial probe, resonant cavity and free space method. These techniques are selected depending on sample size, frequency range, type of material and temperature range.

2.5.1 Transmission Line Method

In the transmission line measurement method, the dielectric sample is placed inside the section of enclosed transmission line. The line section is either a rectangular waveguide or coaxial cable. Two ports of a vector network analyzer are connected to the transmission line. An electromagnetic wave is incident at the sample and the scattering parameters

(S11 and S21) are acquired and are then converted into the complex permittivity of the tissue. The conversion of transmission and reflection coefficients into dielectric parameters is accomplished automatically by the software available with the system. The Nicholson-Ross-Weir (NRW) method and the NIST iterative method are the most commonly used conversion algorithms [55]. With the transmission line method, measurements can be performed over a broader frequency range, but samples are required to have certain shape before they need to be placed in the line. Moreover, the samples must properly fit inside the section of transmission line, so that there is no air gap. This technique is suitable for excised sample measurements and is not suitable for *in vivo* measurements. In one of the works by Shibata *et al.*, transmission line method was used to measure properties of tissue-mimicking liquid phantoms [56]. In another study, Reinecke *et al.*, used transmission line techniques to measure edema in brain tissue [57]. The setup using the transmission line method is shown in Fig. 2.6.

2.5.2 Open-Ended Coaxial Probe Method

The open-ended coaxial probe method is widely adapted for the characterization of biological tissues in the microwave range of frequencies. It consists of a truncated section of transmission line which is further connected to a vector network analyzer. The probe is placed on the surface of the material to be measured if it is solid or semi-solid or is immersed into the liquid. The electromagnetic wave travels through the transmission line

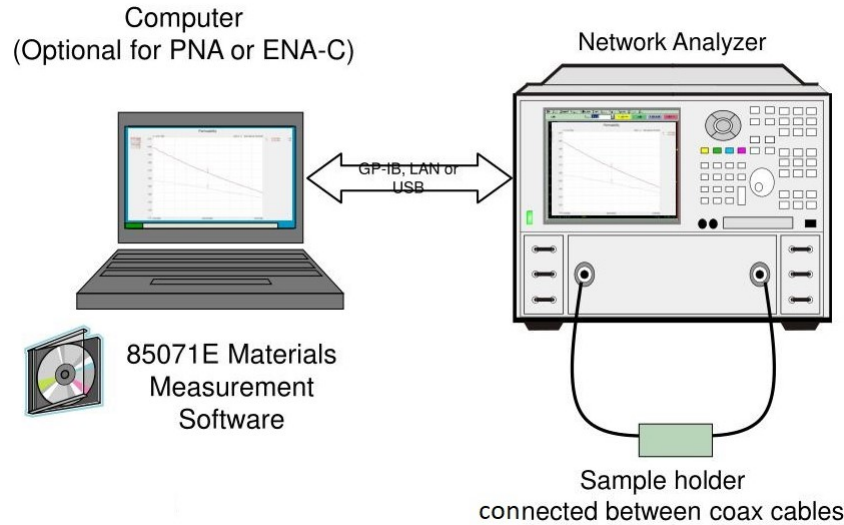


Fig. 2.6: Transmission line method for dielectric property measurement [58].

and strikes at the material; some of the wave is absorbed and some is reflected back. The reflected signal is expressed as scattering parameter S_{11} which is then converted to complex permittivity automatically with the software available with the system. Dielectric properties are different for each material as their reflection response will be different. This technique has several advantages for example, sample requirement is minimum and measurements can be performed over a broader frequency range [59]. The setup for coaxial probe method is shown in Fig. 2.7. Dielectric probe configurations (from Keysight and Speag) are available for the measurements which are shown in Fig. 2.8.

High-performance probe: The high temperature probe has a rugged design with a hermetic glass-to-metal seal that protects the probe from corrosive and abrasive chemicals. This probe has the ability to withstand temperature of the range -40 to 200 °C. The probe

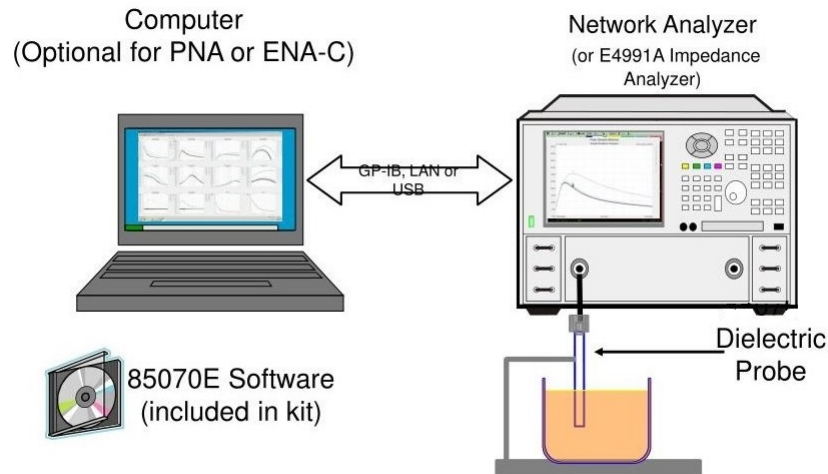


Fig. 2.7: Coaxial probe method for measurement of dielectric properties [58].

has a large flange which helps in the measurement of flat-surfaced solid materials. The probe is also suitable for the measurements of liquids and soft semi-solids. The probe can operate over a wide frequency range of 200 MHz to 20 GHz with a vector network analyzer. This probe has the larger sensing volume as it has a 3.5 mm aperture.

Slim probes: Slim probe is the most widely used probe for the dielectric measurements of biological tissues. It has a small diameter of 2.2 mm making it more suitable for measurement of small sample sizes. The probe can be used to measure liquid, semi-solid and flat surfaced solid materials. The probe can operate over the frequency range of 500 MHz to 50 GHz.

Performance probe: Third type of probe is the performance probe which combines features of both high temperature and slim form probes. This probe can perform over high

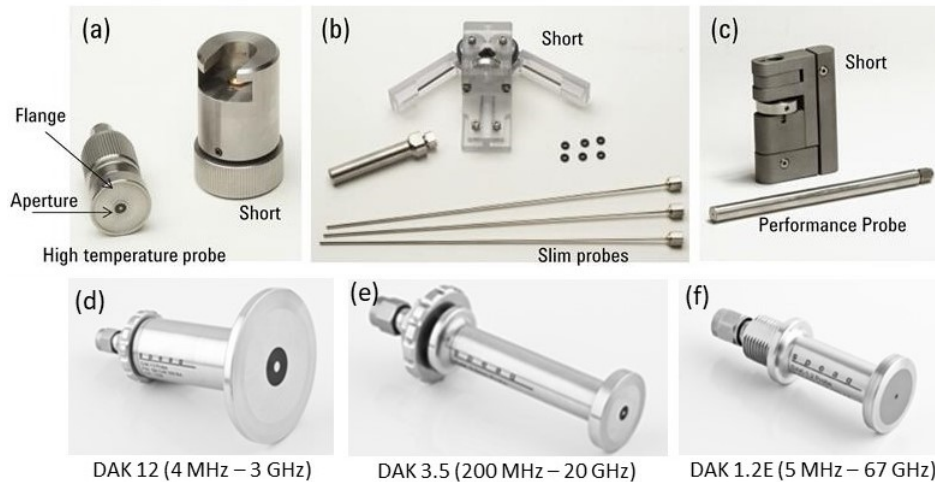


Fig. 2.8: Keysight N1501A (a) High temperature probe, (b) Slim form probes and (c) Performance probe [59]; Speag (e) DAK 12 (4 MHz – 3 GHz), (f) DAK 3.5 (200 MHz – 20 GHz), (g) DAK 1.2E (5 MHz – 67 GHz) [60].

temperature (-40 to 200 °C) and over wide frequency range (500 MHz to 50 GHz). The probe is useful for measurements in food, medical and chemical industries as it is hermetically sealed at both probe ends [59].

DAK 12 (4 MHz – 3 GHz): Probe has high resistance to corrosive materials. It has operating temperature range of 0 – 60 °C. The outer conductor inside diameter is 12 mm and inner conductor diameter is 3.8 mm. Flange has diameter of 18 mm and it is made up of stainless steel.

DAK 3.5 (200 MHz – 20 GHz): The probe is robust and have high measurement repeatability. The outer and inner conductor diameter of probe is 3.5 mm and 0.93 mm respectively. The operating temperature range is 0 – 60 °C.

DAK 1.2E (5 MHz – 67 GHz): The probe is robust with operating temperature

range of 0 – 50 °C. The outer and inner conductor diameter of probe is 1.2 mm and 0.28 mm respectively.

2.5.3 Free-space Measurement Method

In free-space measurement methods, two antennas facing each other are connected to the vector network analyzer and the sample to be measured is placed in the holder that lies in between the antennas. The dielectric properties of the sample are obtained from the reflection and/or transmission coefficients with the inbuilt software of the system. The samples required for these methods should be planar with constant thickness and should be large enough to intercept the entire beam. Moreover, this method is non-contacting and allows measurements at high temperature and in hostile environments. The potential problem associated with this method is that multiple reflections occur between the sample and antennas and between samples, which reduces the accuracy of the measurement [59]. The free-space measurement setup is illustrated in Fig. 2.9.

2.5.4 Resonant Cavity Method

A resonant cavity system is comprised of a resonant cavity fixture that is connected between two ports of a vector network analyzer through coaxial cables as shown in Fig. 2.10. This method works on the fact that there will be shift in the resonant frequency (f) and quality factor (Q) of a tuned cavity with a placement of lossy sample into it. The

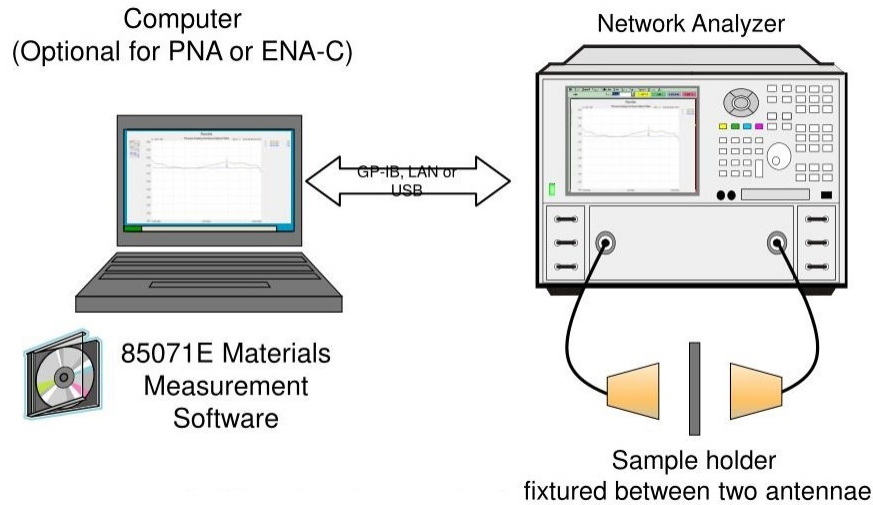


Fig. 2.9: Free-space method for measurement of the dielectric properties [58].

dielectric properties are calculated by measuring resonant frequency and quality factor which is altered on inserting the sample into the cavity. The volume of the sample and the empty cavity are also considered for the calculations. The measurements are automatically performed with the help of a VNA. This is the most accurate method for dielectric measurements, but it provides complex permittivity of the material at a single frequency. The sample preparation for it is not simple. The excised sample needs to be precisely sized and shaped so that it can fit in the cavity. This can lead to air gaps between sample and cavity, fluid loss in the tissue while shaping and can increase the density of the tissue while pushing it inside the cavity. All these factors eventually can affect the dielectric properties of the tissue and result in errors in the measurements. Very few studies used resonant cavity methods for characterization of biological tissues. Campbell *et al.*, studied dielectric

difference between healthy and malignant breast tissues using resonant cavity methods [61].

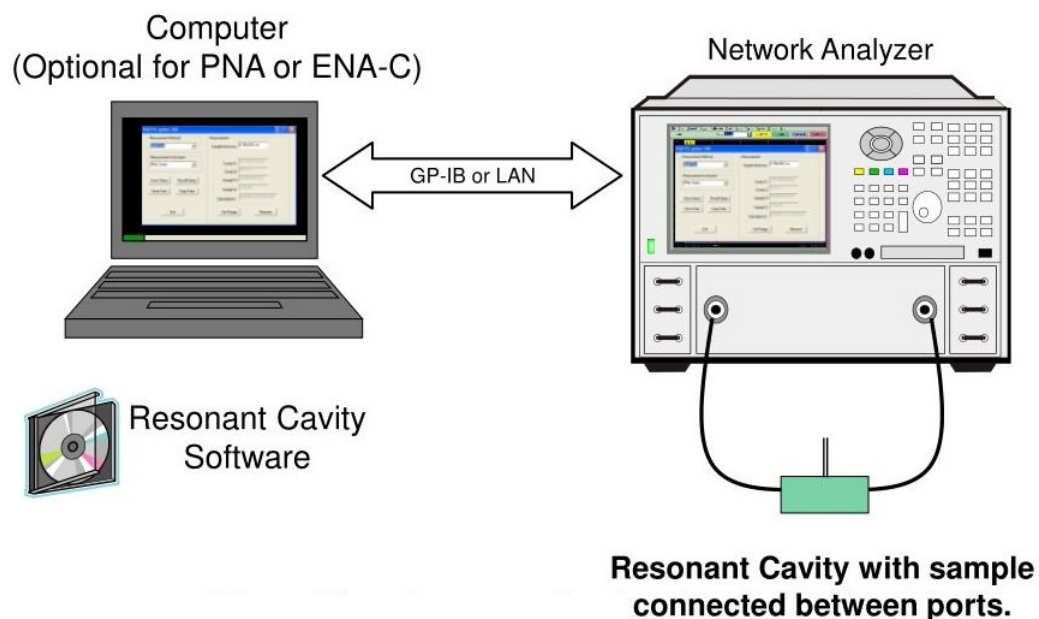


Fig. 2.10: Resonant cavity system for measurement of dielectric properties [58].

2.6 Specific Absorption Rate

Electromagnetics is widely explored in medical applications both in diagnostics and therapeutics. Due to their non-invasive and non-ionizing nature, these technologies are the main focus of researchers. When electromagnetic radiations interact with the biological tissues, some of the energy is absorbed in the tissues causing thermal effects. This is quantified by the specific absorption rate (SAR). SAR is defined as the power absorbed per

unit mass of tissue, with units of Watt per kilogram (W/kg). The local SAR is expressed as:

$$\text{SAR} = \frac{\sigma |E|^2}{\rho}, \text{ [W/kg]} \quad (2.8)$$

where E is the electric field strength [V/m], σ is the conductivity [S/m] and ρ is the mass density of the tissue [kg/m³].

Prolonged exposure to electromagnetic radiations may cause adverse effects on human health and potential damage to the radiated tissues. Therefore, a SAR evaluation needs to be performed for safety validation of medical devices. Several guidelines and regulations based on scientific evidence have been formulated to avoid harmful effects. A number of worldwide organizations such as American National Standards Institute (ANSI), the Institute of Electrical and Electronics Engineers (IEEE) [62], the International Commission on Non-Ionizing Radiation Protection (ICNIRP) [63], and the Federal Communications Commission (FCC) [64] set regulations and standards for measurement of SAR and maximum acceptable values. IEEE standard C95.1 specifies peak 10 g SAR < 2.0 W/kg and peak 1 g SAR < 1.6 W/kg. FCC sets SAR limit to be 1.6 W/kg [65].

Chapter 3

Dielectric Properties of Skin-Mimicking Tissue Models in the 5 – 20 GHz Range

This chapter is based on the following publication:

J. Boparai, L. Kranold, L. Fortaleza and M. Popović, “Dielectric Properties of Skin-Mimicking Tissue Models in the 5 – 20 GHz Range,” *IEEE International Symposium on Antennas and Propagation and North American Radio Science Meeting*, 2020, pp. 1623-1624.

Preface to Chapter 3: The development and systematic evaluation of emerging skin cancer diagnostic prototypes require tissue-mimicking phantoms with accurate dielectric representation of human tissues for repeated testing before performing actual measurements on humans. Therefore, we performed a study of different skin-mimicking tissue-phantoms with the same measurement instrumentation and environmental

conditions, thus providing common ground to compare them and eventually give guidance in selecting a suitable skin phantom depending upon the application and possible constraints. The dielectric measurements were performed with Keysight 1501A performance probe and FieldFox N9918A handheld vector network analyzer based on the reflection measurements approach. The input signal power was set at -10 dBm and measurements were performed over 1001 frequency points, over the range 5 – 20 GHz.

For consistent comparison, we analyzed dielectric properties of two types of skin-mimicking phantoms: fabricated carbon-polyurethane-based and commercially available skin phantoms obtained from Probingon AB. Carbon-polyurethane phantoms remain stable for a longer period of time but their fabrication process is complex. Probingon AB phantoms are stable for longer period of time if they are sealed and refrigerated. Chapter 3 describes investigation of these two types of skin phantoms in three different configurations for analyzing their dielectric properties:

- Configuration 1 is the investigation of a thicker block of 20-mm skin phantom
- Configuration 2 is thinner skin phantom of 2-mm thickness
- Finally, for configuration 3, both types of skin sample are taken with 2-mm thickness and are placed on fat-mimicking tissue phantom

The purpose of choosing these three configurations was to observe how variation of thickness of skin phantoms and layering of skin phantoms with fat phantom affects the

dielectric property measurements, since skin thickness varies with different locations on the body and there is a presence of a subcutaneous fat layer.

This chapter illustrates that the choice of phantoms which represent the skin well in a dielectric sense, depend on the thickness and configuration of the skin and fat layers. Additional factors to be considered when selecting the phantom type are complexity, stability and cost.

Abstract—The research of microwave-based medical systems requires accurate knowledge of dielectric properties of biological tissues. For the development and validation of such systems, tissue-mimicking models (phantoms) are needed for controlled laboratory experiments. This study investigates the dielectric properties of two commonly used skin-mimicking phantoms which are composed of different material configurations. The dielectric properties are characterized using a performance probe over the frequency range of 5 – 20 GHz. We observe the relative permittivity and conductivity in the range of interest for three different configurations of each tissue phantom: a thicker, “block” geometry and a thinner 2-mm sample representative of the human skin in its thickness and positioned on a fat-mimicking phantom layer.

Keywords—skin mimicking phantoms, Probingon, carbon, dielectric properties

3.1 Introduction

The accurate dielectric characterization of biological tissues is critical in order to develop diagnostic tools for the detection of abnormalities such as skin melanoma. The detection of these biological abnormalities using microwave diagnostic technologies has attracted a significant attention due to their non-invasive and non-ionizing nature. Different prototypes using microwaves have been reported in the recent years [1, 2] with efforts to detect cancerous tissues, burns and other malignancies.

The dielectric properties of skin vary at different body locations [3]. This is due to differences in skin tissue thickness and presence of underlying tissues. In this study, we investigate the effect of thickness variation and layered phantoms on the dielectric properties for these tissue mimicking materials. Hence, we considered two different skin phantoms that have been reported as suitable representations of human skin [4, 5]. In addition to measuring both phantoms at different thicknesses, the 2-mm thin phantoms were placed on the same fat-mimicking material.

3.2 Materials

The measurement samples included two different types of skin phantoms and one fat-mimicking phantom. The first skin phantom is based on carbon black, polyurethane and graphite. By varying the ratio of these three components, different dispersive dielectric

properties can be achieved, and the phantoms are reported to be stable over the course of several months [4]. The second type of skin-mimicking phantom was acquired from Probingon AB and reported to have a shelf-life of two months if preserved accordingly [6]. For the evaluation of the dielectric properties of both skin phantom types, three dielectric configurations were considered. First, we measured a 2-mm sample of each skin phantom. Second, a cylindrical block of minimum 20-mm thickness was investigated. The third case was the 2-mm homogenous samples placed on a homogeneous block of fat-mimicking carbon-based phantom.

3.3 Experimental Set-up

The materials under investigation were characterized using a Keysight N1500A Performance Probe Kit operated with a FieldFox Vector Network Analyzer [7]. The phantom properties were studied in the frequency range of 5 – 20 GHz and the experimental setup is shown in Fig. 3.1.

3.3.1 Calibration and Validation

Before performing the measurements on these phantoms, the system was calibrated using the standard air-short-water procedure. Additionally, validation measurements were performed before and after each phantom characterization. Therefore, materials of known dielectric properties were measured: De-ionized water and air. All experiments were performed at

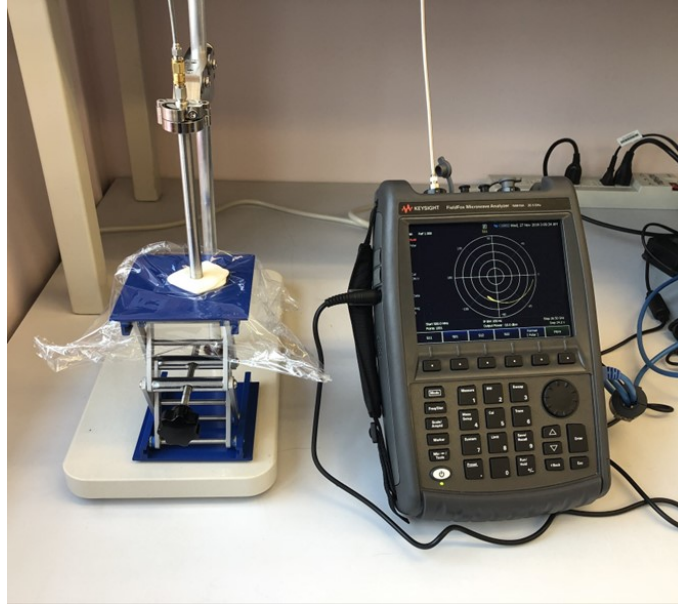


Fig. 3.1: Experimental Setup: Keysight performance probe with 2mm Probingon skin phantom and FieldFox vector network analyzer.

room temperature.

3.3.2 Measurements of Dielectric Properties

Dielectric properties of the materials under test (MUT) were investigated by taking ten consecutive measurements in the frequency range of 5 – 20 GHz. Full contact between the surface of material to be tested and the probe was ensured and mean as well as standard deviation of the consecutive measurements were calculated.

3.4 Results

Fig. 3.2 (a) and (b) show the measured relative permittivity for each material and for the following configurations: 2-mm (solid blue line), 20-mm (dot-dashed pink line), and 2-mm on fat phantom (dashed brown line). Fig. 3.3 (a) and (b) graph the associated measured conductivity values. The results were recorded in the temperature range of 22.9 – 23.4 °C.

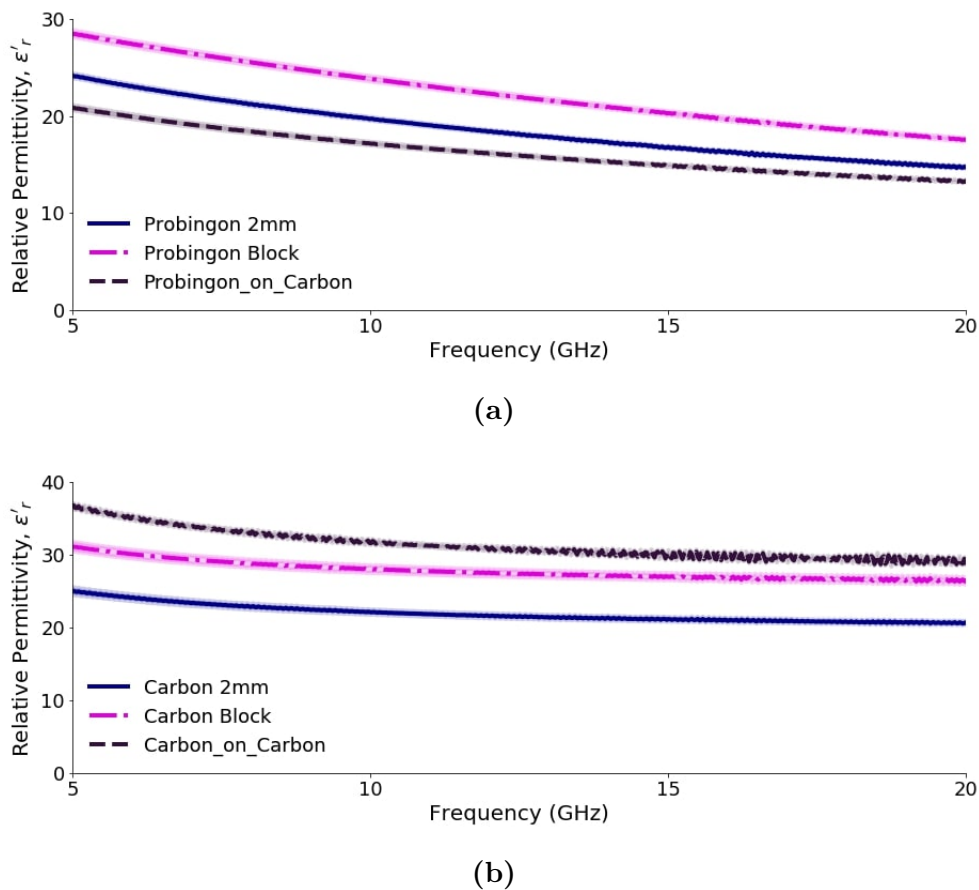
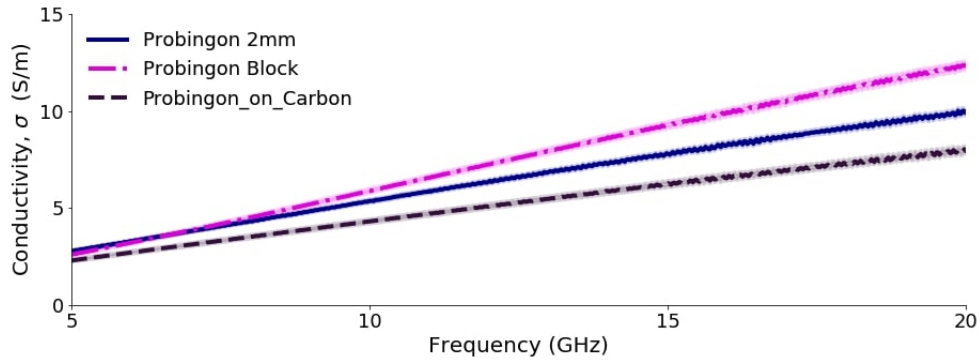
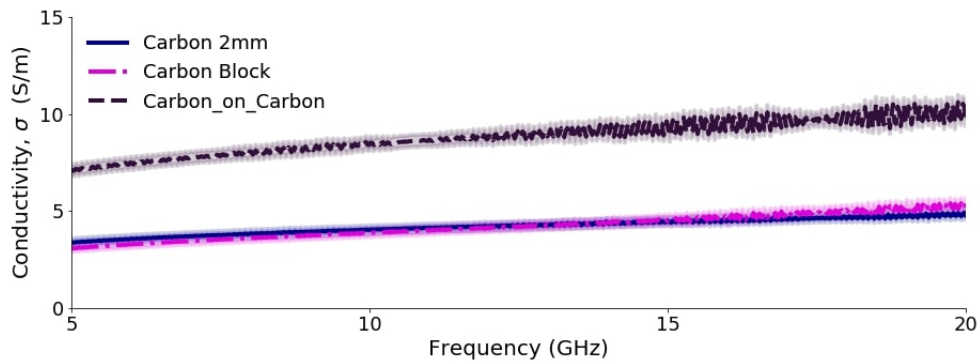


Fig. 3.2: Relative permittivity of (a) Probingon phantom in 2 mm, 20 mm and 2 mm on carbon fat phantom. (b) Carbon-based phantom in 2 mm, 20 mm and 2 mm on carbon fat phantom.



(a)



(b)

Fig. 3.3: Conductivity of (a) Probingon phantom in 2 mm, 20 mm and 2 mm on carbon fat phantom. (b) Carbon-based phantom in 2 mm, 20 mm and 2 mm on carbon fat phantom.

We observe that the relative permittivity of the 20-mm Probingon phantom is higher than the 2-mm thin sample or if placed on a block of fat-mimicking material. In contrast, for the carbon-based phantoms, the permittivity is higher if placed on the fat-mimicking material and lowest for the 2-mm thin sample. Furthermore, the behavior of the conductivity of the Probingon phantom is similar to the permittivity. The 20-mm thick sample shows the highest conductivity and if placed on fat-mimicking material the sample has low conductivity.

The conductivity of the carbon-polyurethane phantom is similar for the samples at different thickness, however, it is significantly higher when placed on the fat-mimicking material. Most importantly, these measurements suggest that care should be taken when selecting the phantoms for their application depending on desired parameters, stability requirements and geometry.

3.5 Conclusion

In this report, we compare two types of skin-mimicking phantoms. Although properties of these materials have been reported in the past, they were usually characterized with varying equipment, making the result comparison challenging. The dielectric properties of these phantoms have been compared with varying thickness and with an underlying fat phantom layer. We conclude that the choice of suitable phantom depends on the application, and both phantoms lie within the range of human skin measurements.

3.6 Acknowledgment

This work was supported by Natural Sciences and Engineering Research Council of Canada (NSERC) Discovery (NSERC RGPIN-2019-05850) and Collaborative Research and Development (CRDPJ 521870 – 17) grants.

3.7 References

- [1] E. C. Fear et al, “Microwave breast imaging with a monostatic radarbased system: A study of application to patients,” *IEEE Trans. Microw. Theory Tech.*, vol. 61, no. 5, pp. 2119–2128, May 2013.
- [2] A. Santorelli, et al, “A time-domain microwave system for breast cancer detection using a flexible circuit board,” *IEEE Trans. Instrum. Meas.*, vol. 64, no. 11, pp. 2986-2994, Nov. 2015.
- [3] P. F. M. Smulders, ”Analysis of human skin tissue by millimeter-wave reflectometry”, *Skin Res. Technol.*, vol. 19, no. 1, pp. 209-216, Feb. 2013.
- [4] J. Garrett, “Average dielectric property analysis of non-uniform structures: Tissue phantom development, ultra-wideband transmission measurements, and signal processing techniques”, Master’s Thesis, University of Calgary, Calgary, Canada, 2014.
- [5] L. Joseph, M. Perez, R. Augustine, “Development of 500 MHz – 20 GHz Ultra-Wideband Multi-Layered Heterogeneous Phantom of Different Human Soft Tissues for Various Microwaves Based Biomedical Applications”, *Proc. 13th European Conference on Antennas and Propagation (EUCAP2019)*, Krakow, Poland, Mar 31 – Apr 5, 2019.

[6] Probingon AB, Patient Centered Diagnostics, 2019, [Online], Available: <https://www.probingon.com/> [Accessed 13.12.2019].

[7] Keysight Technologies, N1501A Dielectric Probe Kit, 2020, [Online], Available: <https://www.keysight.com/en/pd-2492144-pn-N1501A/dielectric-probe-kit?nid=-536902475.1128377&cc=CA&lc=eng> [Accessed 09.01.2020].

Chapter 4

Development and Characterization of Skin Phantoms at Microwave Frequencies

This chapter is based on the following publication:

J. Boparai and M. Popović, “Development and Characterization of Skin Phantoms at Microwave Frequencies,” *IEEE Journal of Electromagnetics, RF and Microwaves in Medicine and Biology*, vol. 6, no. 3, pp. 296-304, Sept. 2022.

Preface to Chapter 4: After performing consistent comparison of the dielectric properties of different skin-mimicking phantoms with different geometrical layouts described in chapter 3, our next goal was the systematic development and validation of several skin phantoms with tumor inclusions in the 0.5–26.5 GHz frequency range.

The idea was to provide a comprehensive set of anatomically and dielectrically realistic phantoms for experimental validation of emerging microwave-based systems for skin cancer

diagnosis. Chapter 4 describes the proposed set of phantoms developed using inexpensive, stable and readily available oil-in-gelatin materials which incorporates tumor inclusions with varying sizes, locations and shapes, thus providing a range of anatomical representations which are required for proper testing and analyzing the feasibility of the diagnostic tools under development. To analyze the effect of underlying skin on dielectric properties, two skin thicknesses (8 mm and 2.5 mm) were also considered

Moreover, the dielectric properties of the realized phantoms display good agreement with the excised malignant human tissues reported in the literature.

Abstract—Realistic tissue-mimicking phantoms are required for experimental evaluation and validation of microwave reflectometry prototype systems for skin cancer detection before performing any tests on human subjects. These phantoms must accurately emulate the dielectric properties for both healthy and malignant skin tissues. In this work, we develop and experimentally investigate multiple skin phantoms with tumor inclusions in the frequency range of 0.5–26.5 GHz. These heterogeneous phantoms are realized by varying the tumor size and placement relative to the skin. The tumors with irregular borders are also investigated. For analyzing the effect of underlying skin on dielectric properties, two skin thicknesses are considered: 8 mm and 2.5 mm. The proposed heterogeneous phantoms are developed using inexpensive materials: oil, gelatin, deionized water and formaldehyde. The dielectric properties of fabricated phantoms are characterized

with Keysight performance probe connected with a FieldFox handheld vector network analyzer. Our results demonstrate that the dielectric properties of the developed phantoms closely agree with those of the excised malignant human tissues reported in the literature over the entire frequency range of 0.5–26.5 GHz and can be hence reliably used for experimental validation in studies towards microwave-based diagnostics of skin lesions.

Index Terms—Dielectric properties, microwave reflectometry, skin cancer, tissue-mimicking phantom, tumor.

4.1 Introduction

Skin cancer is the fastest growing cancer worldwide. The malignant melanoma (MM), basal cell carcinoma (BCC) and squamous cell carcinoma (SCC) are the most common forms where BCC and SCC are collectively referred to as *non-melanoma* skin cancer [1]. Melanoma is considered to be the most aggressive of skin cancers, however, even BCC and SCC can lead to metastasis if left undiagnosed and untreated [2].

Early-stage diagnosis is vital to successful treatment of all skin cancer forms. The physicians usually perform visual examination based on the ABCDE rule (asymmetry, border, color, diameter and evolution) and sometimes use visual aid like dermatoscope to identify the suspicious lesion [3], [4]. Consequently, the clinician’s expertise and experience are determining factors for an accurate diagnosis. With any suspicious lesion, biopsy or surgical excision is advised, followed by the laboratory pathology analysis of the sample.

Several techniques such as sonography, thermal imaging, 3D photography, CT scan, ultrasound, MRI and confocal microscopy [5], [6] have been explored in the past for diagnosis of skin cancer. Most of these techniques suffer from certain limitations. Confocal microscopy and thermal imaging have high cost and limited visualization depth [7]. With sonography, it is difficult to measure very thin and very thick melanomas. Ultrasound is inherently operator-dependent, thus requiring trained experts [8]. CT scanning uses ionizing radiations while 3D photography and MRI are expensive and time-consuming processes, involving some discomfort to the patient [9]. Furthermore, computer-aided diagnosis systems based on machine learning algorithms for identification of skin lesions have been proposed [10], [11] but these techniques lack clinical trials and image samples that cover rare tumor conditions [12]. Recently, significant strides in research have been reported on the use of microwave reflectometry and spectroscopy techniques for diagnosis of breast cancer, lung cancer and brain stroke [13], [14] that rely on the reported inherent dielectric contrast between malignant and normal tissues [15]. The non-ionizing, non-invasive nature and low cost have all played part in the appeal of researching the possibility of using low-power microwaves for diagnostic purposes [16]. Additionally, these techniques have higher sensitivity and can generate high-resolution images, thereby promising to detect tumors at early stages [17].

For successful evaluation of emerging microwave prototype systems, phantom models faithfully representing human tissues in dielectric sense and in the frequency range of interest

are required. Several tissue-mimicking phantoms based on different material compositions such as liquid [18], solid [19] and semi-solid [20]–[22] have been developed in the past. Liquid phantoms are subject to dehydration while solid phantoms have complex fabrication process. The semi-solid phantoms may be less durable but their capability of accurately mimicking dielectric properties of tissues over the wide frequency range, ease of fabrication and potential of forming heterogeneous samples makes them a favorable choice in the fabrication of skin phantoms. Researchers also used 3D printing techniques for developing phantoms or molds which are later filled with tissue-mimicking materials [23]–[25]. Limited substrate choices and inability to accurately mimic tissue dielectric properties of biological tissues and complex process are main disadvantages of these techniques [26].

Numerous homogeneous skin phantom configurations have been reported in the literature [27]–[30] but a very limited number of phantom models with malignant configurations have been investigated. In ref. [31], phantoms mimicking dielectric properties of human skin, malignant BCC, and malignant SCC tissues were realized over 0.5–50 GHz frequency range. Other studies report inclusion of tumors into skin phantoms [32], [33]. These studies, however, do not show investigations with systematic variation of tumor size or location. In our previous work, we did consistent comparison of the dielectric properties of three different types of skin mimicking tissue phantoms in the 0.5–26.5 GHz frequency range using same instrumentation and under same environmental conditions. Three different geometrical layouts were considered such as thick homogeneous block, 2

mm thin skin and 2 mm thin skin placed on fat material phantom [34], [35]. The work here reported builds on these foundations but explores a range of skin-tumor geometries representative of anatomical structure.

The main goal of this work is to systematically develop and evaluate multiple experimental skin phantoms with tumor inclusions for accurately mimicking dielectric properties of human tissues over the frequency range of 0.5–26.5 GHz. Tumor phantoms with various sizes are combined with skin in a range of geometrical arrangements. To analyze the effect of irregular borders, tumors with irregular borders were also fabricated. Two different skin sizes are considered to analyze the effect of underlying skin on measured dielectric properties. Thus, in total, 32 heterogeneous models have been developed, with three possible tumor placements and tumor diameter sizes ranging from 2 mm to 10 mm. The dielectric properties are measured with Keysight performance probe connected to vector network analyzer (VNA). The measurements are compared with the values of excised malignant BCC and SCC tissues obtained from the literature [36]. Thus, a substantial set of anatomically and dielectrically realistic phantoms provide an excellent test domain for emerging microwave-based skin cancer diagnostic systems. The increments in tumor size, but also variations in its location and shape, can aid in identifying the detection limits of the diagnostic prototype.

4.2 Materials and Procedures

4.2.1 Tissue-Mimicking Phantom Materials

The skin phantoms (combined epidermis-dermis single layer) with tumors are fabricated by following the procedure described in [22], [37] and each preparation step in the fabrication process is illustrated in Fig. 4.1. All chemical ingredients used in fabrication (shown in Table 4.1) were purchased from Sigma-Aldrich, Oakville, Canada. The Ultra Ivory detergent was a product of the Procter and Gamble (P&G) brand. These oil-gelatin based phantoms are reported to be stable over 9 weeks of time after preparation if stored properly in airtight containers [22].

4.2.2 Fabrication of Skin Phantoms with Tumor Inclusions

Heterogeneous skin phantoms with tumor inclusions are fabricated in three configurations as illustrated in Fig. 4.2. These configurations were selected to represent often encountered tumor-skin anatomical geometries.

For the first case, tumor is embedded so that its top surface is visible in the top view and leveled with the surrounding skin layer as illustrated in Fig. 4.2(a). In the fabrication process, the skin-equivalent material is poured into cylindrically shaped container, allowed to solidify for 24 hours. A ring-shaped hollow mold is used to create a small hollow volume

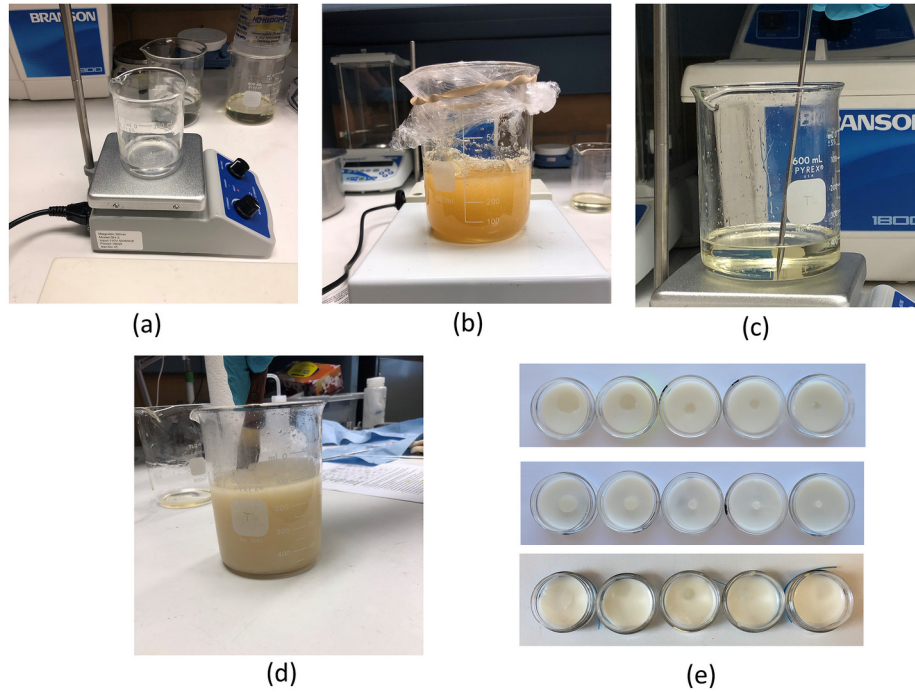


Fig. 4.1: Illustration of each preparation step in the process of phantom fabrication: (a) Mixture of p-toluic acid and n-propanol in a beaker placed over the hot plate. (b) The resultant solution of mixture obtained in (a), deionized water and gelatin after heating. (c) Oil heated to 50 °C in a beaker over hot plate to which resultant solution from (b) is added. (d) Final mixture on adding formaldehyde and liquid surfactant to mixture obtained in (c). (e) Solidified heterogeneous phantoms shown in molds.

in the skin surface, reserved for tumor material to be added at a later stage.

For the second case (Fig. 4.2(b)), the tumor surface is raised out of the skin, following the same procedure as described above, but here a ring-shaped hollow mold is placed at the top of skin surface to which tumor material is finally added.

In the third case (Fig. 4.2(c)), tumor is within the skin layer. This phantom arrangement is fabricated in three steps. First two steps are similar to first case. In the third step, another

Table 4.1: Ingredients used in the proposed phantoms [37]

	Amounts Taken	
	Skin	Tumor
p-toluic acid (g)	0.294	0.346
n-propanol (mL)	28.69	17.00
deionized water (mL)	279.5	328.0
200 Bloom gelatin (g)	50.02	58.67
Formaldehyde (37% by wt) (g)	3.33	3.72
oil (mL)	98.6	38.4
Ultra-Ivory detergent (mL)	5.86	2.00

wt: weight.

skin layer is poured over the tumor and allowed to solidify. This arrangement represents the subcutaneously occurring tumors.

To investigate the variability of the measured properties as a factor of size (diameter and thickness) of underlying skin, all phantom combinations are characterized with two different sizes of skin: 1) skin layer of diameter 38.5 mm and height 8 mm; and 2) skin layer of diameter 29 mm and height 2.5 mm, referred to as thick and thin skin, respectively [38], [39].

Further the diameter of tumor (2 mm in thickness) is varied as 10 mm, 8 mm, 6 mm, 4 mm and 2 mm [40]–[44]. With 3 cases (shown in Fig. 4.2), each having two skin sizes and five tumor diameter variation (Fig. 4.3), there is a total of 30 combinations. In order to analyze the effect of irregular border of tumor, additional cases are considered, where a 10 mm tumor with irregular border is combined with thick and thin skin.

The Table 4.2 summarizes the experimental plan constructed to examine the probe

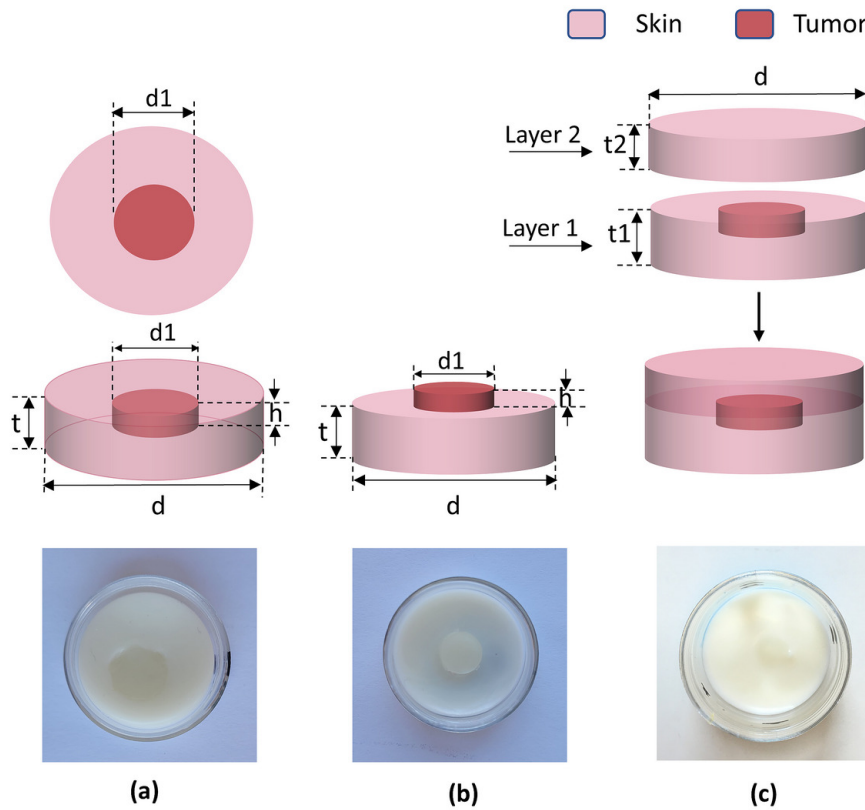


Fig. 4.2: Sketch and photograph of skin phantom samples with: (a) tumor leveled with the surface of skin (b) tumor raised out of skin (c) subcutaneously located tumor. d and t are diameter and thickness of skin, d_1 and h are diameter and thickness of tumor. t_1 and t_2 are thickness of Layers 1 and 2, respectively.

response to different tumor-skin arrangements.

4.2.3 Measurement Setup and Procedure

The dielectric properties (real relative permittivity and conductivity) of the fabricated set of tissue-mimicking phantoms were determined using the open-ended coaxial probe technique. The setup is comprised of a Keysight N1500A performance probe and a

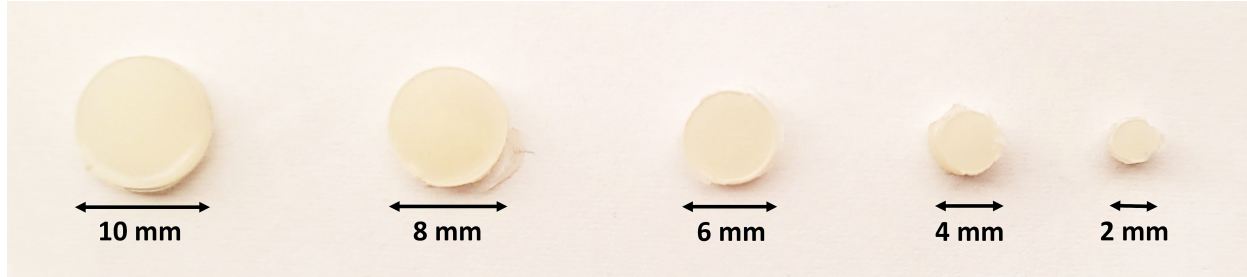
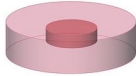
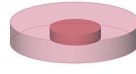





Fig. 4.3: Photograph of fabricated gel-based tumors, indicating variation in size: 10, 8, 6, 4, and 2 mm.

Keysight N9918A FieldFox handheld vector network analyzer. The phantoms are characterized at room temperature (24 °C). The temperature of deionized water used for calibration and validation and material under test (MUT) is monitored using a digital thermometer (Thermopro) by inserting the tip into the material throughout the experiments. Aiming for low-power probing fields, eventually required for safety reasons, an incident signal power was set at -10 dBm, with a 100 Hz intermediate frequency bandwidth and with 1001 frequency points, over the range 0.5–26.5 GHz. The dielectric probe was calibrated with the three-standard calibration method, namely air, short and deionized water. The measurement setup is shown in the Fig. 4.4.

The performance of the probe is validated before and after measurement of each sample by measuring the dielectric properties of known materials i.e., deionized water and air over the frequency range of 0.5 to 26.5 GHz. For evaluating the uncertainty of the measurement system, the dielectric properties of validation material (deionized water) are measured. We considered random errors and systematic errors at each frequency point. Random errors are

Table 4.2: Experiments summary

Experiment	Underlying skin thickness (Type)	Tumor Location	Tumor sizes (mm)	Phantom Drawing
Experiment 1	8 mm (thick)	Tumor surface in align with skin surface	10, 8,6,4,2	
Experiment 2	2.5 mm (thin)	Tumor surface in align with skin surface	10, 8,6,4,2	
Experiment 3	8 mm (thick)/ 2.5 mm (thin)	Tumor raised out of the skin	10, 8,6,4,2	
Experiment 4	8 mm (thick)/ 2.5 mm (thin)	Tumor inside the skin	10, 8,6,4,2	
Experiment 5	8 mm (thick)/ 2.5 mm (thin)	Irregular size tumor with surface in align with skin surface	10	

quantified in terms of repeatability. The 10 repeated measurements on deionized water were taken and mean and standard deviation of mean were computed for both permittivity and conductivity at each frequency point. Then, the average over the complete frequency range is calculated. For the evaluation of systematic errors, the mean of characterized data was compared with the known model of deionized water. Third possible type of error known as drift error was assumed to be negligible as we performed recalibration of VNA several times between the sessions. Error due to cable movement is also considered negligible as we are using lift jack to move the material under test towards the probe. Following the guidelines of [45] and [46], total combined uncertainty was computed as square root of the sum of squared values of individual uncertainties. Thus, total combined uncertainty values,

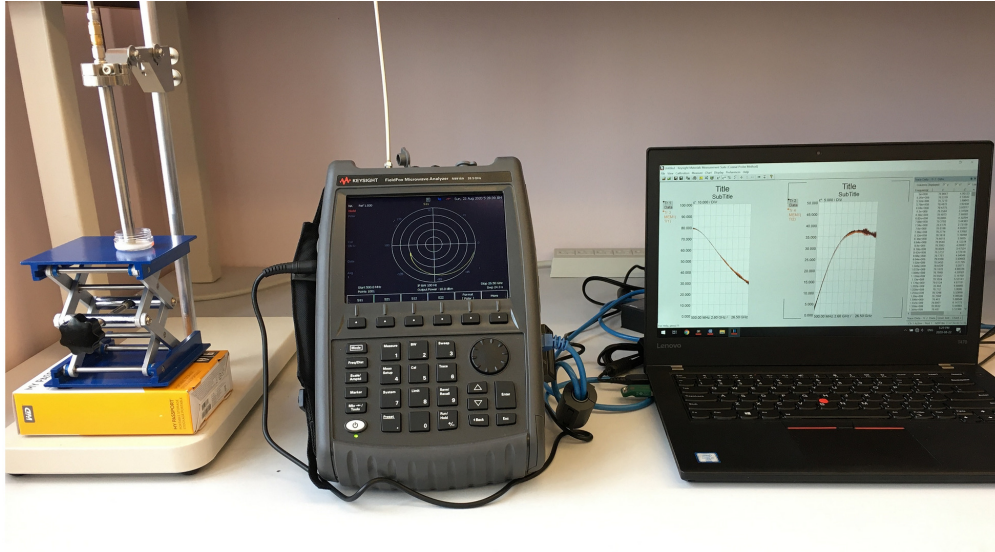


Fig. 4.4: Experimental Setup: On the left, material under test (MUT) is placed on scissor lift jack, over it is the performance probe, on right is the FieldFox handheld vector network analyzer which is connected to laptop for analyzing data. Probe and VNA are connected with coaxial cable.

calculated for permittivity and conductivity, are given in the Table 4.3. The expanded uncertainty was calculated with a coverage factor of $k = 2$ which is obtained by multiplying the total combined uncertainty by 2, resulting in the required confidence level of $\sim 95\%$.

Table 4.3: Uncertainty budget of measured dielectric properties of deionized water

Uncertainty Parameters	Dielectric Properties	
	ϵ_r'	σ (S/m)
Repeatability (SDM) %	0.26	0.45
Deviation from Reference (%)	1.78	1.47
Total Combined Uncertainty (%)	1.8	1.5
Expanded Uncertainty, $k = 2$ (%)	3.6	3

4.2.4 Method

The dielectric properties of the constructed phantoms are analyzed by placing the probe at one position and taking ten consecutive measurements. Then, the mean and two standard deviations (95.5% confidence interval) are calculated and displayed in plots over the frequency range of 0.5–26.5 GHz. The measurements are compared to reference values of the excised tissues of BCC and SCC using one-pole Cole-Cole model described by the equation 4.1 and corresponding Cole-Cole parameters for dielectric properties computation are given in Table 4.4 [36].

$$\varepsilon_r(\omega) = \varepsilon_\infty + \frac{\Delta\varepsilon}{(1 + j\omega\tau)^{1-\alpha}} + \frac{\sigma_s}{j\omega\varepsilon_0} \quad (4.1)$$

where $\omega = 2\pi f$ (f is the frequency of operation), $j = (-1)^{1/2}$, τ is the relaxation time, $\Delta\varepsilon$ is the magnitude of the dielectric dispersion of the skin, ε_∞ is the permittivity of skin at optical frequencies, ε_0 is the permittivity of free space, α is a measure of the broadening of the dispersion, and σ_s is the conductivity of the skin.

4.3 Results And Discussions

In this section, the results are analyzed by plotting the real relative permittivity and conductivity for five different experiments over the entire frequency range of 0.5–26.5 GHz.

Table 4.4: One pole cole-cole parameters to compute dielectric measurements of reference data [36]

Parameter	BCC	SCC
ε_∞	6	10
$\Delta\varepsilon$	43.04	32.99
$\tau(ps)$	7.66	3.04
$\sigma_s(S/m)$	0.05	0.01
α	0.08	0.11

In each plot, the mean is represented by line and the shaded areas gives the 95.5% confidence interval.

4.3.1 Experiment 1: Tumor in Align with Thick Skin Surface

For the first experiment, dielectric properties of phantoms with 8 mm thick skin with tumor inclusions varying from 10 mm down to 2 mm are measured. The relative permittivity and conductivity of tumors measured at the center is shown in Fig. 4.5(a) and (b); those measured at the border is graphed in Fig. 4.5(c) and (d).

We observed that, when measurement is taken at the center of tumors, the permittivity and conductivity remain unchanged for all tumor sizes. In contrast, when measurement is performed at the border of tumors, permittivity and conductivity vary with size of the tumor. Tumors with sizes 10 mm and 8 mm have higher permittivity and conductivity compared to tumors with sizes 6 mm, 4 mm and 2 mm. This investigation suggests that, for smaller tumors, the dielectric characteristics of the surrounding skin dominate the sensing volume

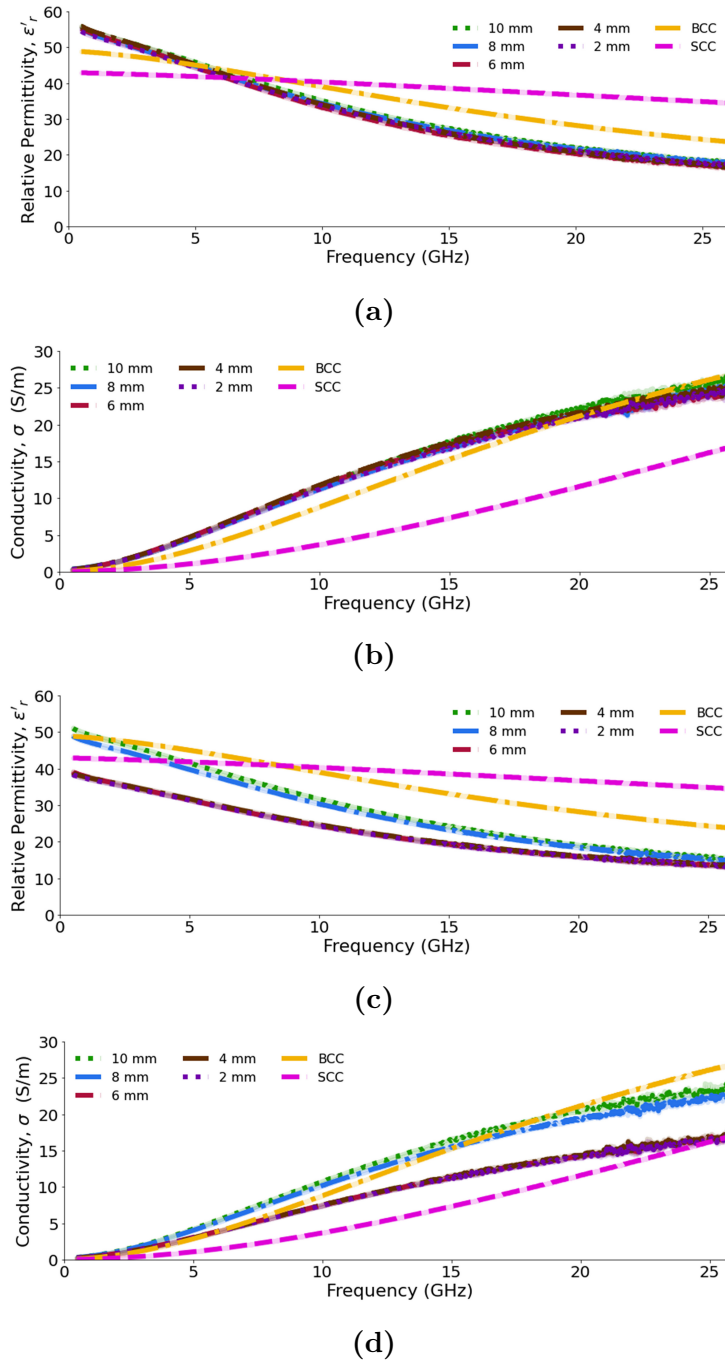


Fig. 4.5: Dielectric measurements of tumor in align with thick skin surface compared with reference BCC and SCC tissues [36]. (a) Real relative permittivity, and (b) conductivity of tumors measured at the center, (c) Real relative permittivity and (d) conductivity of tumors measured at the border.

around the probe [47]. The dielectric measurements are validated by comparing them with excised BCC and SCC tissues taken from literature [36]. Here, we note that the fabricated phantoms have dielectric property values closer to reported values of BCC when measured at the center. In case where the tumor is measured at its border, 10 mm and 8 mm tumor phantoms match closely the reference permittivity values for BCC. The 6 mm, 4 mm and 2 mm tumor phantoms have lower permittivity relative to the value reported for BCC and SCC. For the conductivity, tumors with sizes of 10 mm and 8 mm match the reference BCC, while 6 mm, 4 mm and 2 mm tumors have values better matched to those of the reference SCC.

4.3.2 Experiment 2: Tumor in Align with Thin Skin Surface

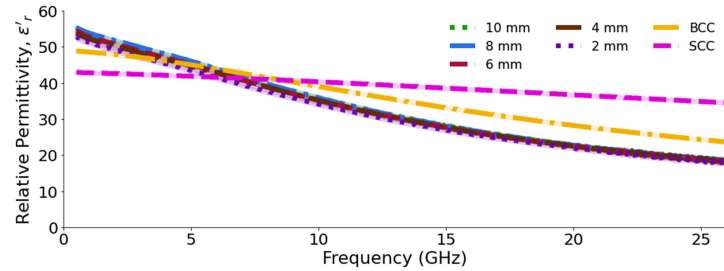
In the second experiment, thin skin phantoms with 2 mm – 10 mm tumor inclusions are considered. The top surface of the tumor is flush with the surface of the skin phantom. The dielectric measurements were performed, first at the center of the tumor (Fig. 4.6(a) and (b)) and then at the border (Fig. 4.6(c) and (d)) of the tumor. We note that, similar to experiment 1, the permittivity and conductivity remain unaltered despite change in the size of the tumor, when measured at the center of tumor. However, when the measurement is performed at the border of tumors, permittivity and conductivity varies with the decrease in tumor size. At border, tumors with bigger size such as 10 mm and 8 mm have higher permittivity and conductivity than small tumors with sizes 6 mm, 4 mm and 2 mm. In this

case as well, measured results give close representation of excised BCC samples. Only the small size tumors (6 mm, 4 mm and 2 mm), when measured at border, have permittivity value smaller than that of the reference BCC and SCC and conductivity is better matched to that of the reported SCC value. This happens because, with the smaller tumors, the sensing volume of the probe is likely to include limited skin volume, and averaging its properties with those of the tumor, which results in a lower permittivity than that of the sensed volume where the tumor material will dominate.

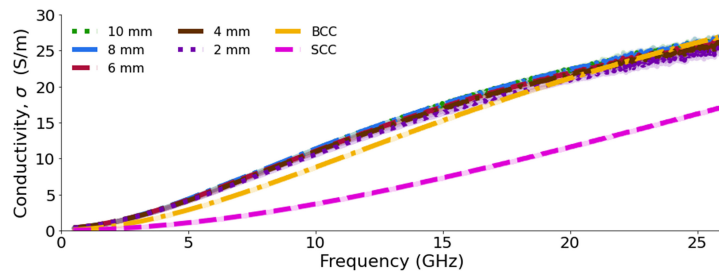
When we compare experiments 1 and 2, we observe that the thickness of the underlying skin layer does not play a vital role in the variation of the results.

4.3.3 Experiment 3: Tumor Raised out of Thick and Thin Skin

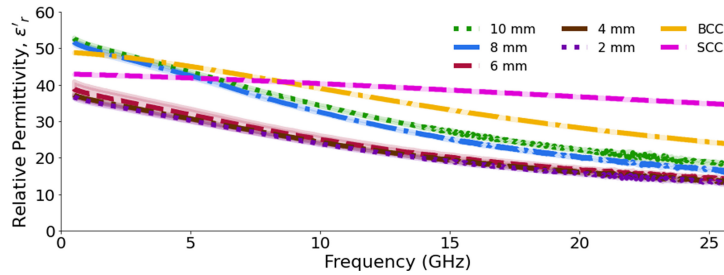
In experiment 3, tumor raised out of skin is taken with tumor size variation from 10 mm to 2 mm. Two cases of underlying skin (thick and thin) are considered for case of each size of the tumor. The relative permittivity and conductivity of tumor with thick underlying skin are given in Fig. 4.7(a) and (b), respectively; permittivity and conductivity of tumor with thin underlying skin are given in 4.7(c) and (d), respectively. It is observed that, for thick skin, tumor with sizes 10 mm, 8 mm and 6 mm have higher permittivity and conductivity than smaller tumors (4 mm tumor and 2 mm lesion). For all tumor sizes, the permittivity values indicate that the phantom materials are closer dielectric representation of the BCC but have lower permittivity than SCC. On the other hand, the conductivity of all tumors



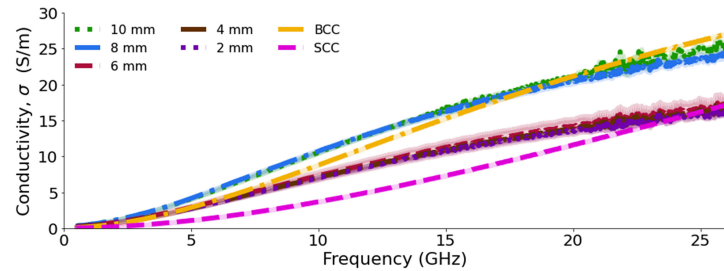
(a)



(b)



(c)



(d)

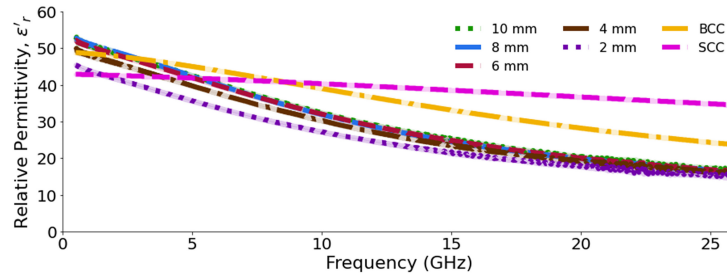
Fig. 4.6: Dielectric measurements of tumor in align with thin skin surface compared with reference BCC and SCC tissues [36]. (a) Real relative permittivity, and (b) conductivity of tumors measured at the center, (c) Real relative permittivity and (d) conductivity of tumors measured at the border.

with larger sizes (10 mm, 8 mm and 6 mm) is similar to the reference values for BCC.

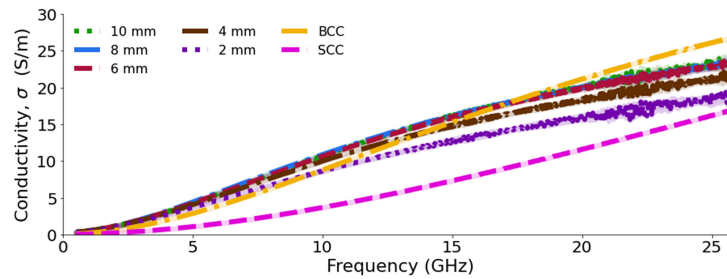
For the thin skin model, tumors with sizes 10 mm, 8 mm, 6 mm and 4 mm have higher permittivity than the measured 2 mm tumors. This raises the question of the probe sensing radius, as it is possible that, for very small tumors, the probe is sensing the tumor permittivity in combination with that of the surrounding skin. In terms of comparison with reported excised tumor values, the permittivity is close to that of BCC. For phantom tumor sizes, 10 mm, 8 mm, 6 mm and 4 mm, the measured conductivity matches closely to that of the reference for BCC well. The small 2 mm tumor has measured values closer to those reported for the SCC value.

4.3.4 Experiment 4: Tumor Inside Thick and Thin Skin

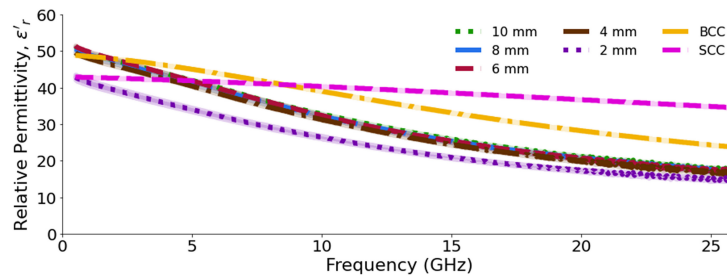
In this experiment, tumor is embedded within the skin. Two cases are considered for the construction of the skin, having in mind the layers surrounding the tumor (Layer 1, with thickness t_1 , and Layer 2 of thickness t_2 , as indicated in Fig. 4.2(c)): the first case, with $t_1 = 8$ mm (thick skin); the other, with $t_1 = 2.5$ mm (thin skin). The upper layer is kept at $t_2 = 1$ mm. The tumor size is varied 2 –10 mm. The relative permittivity and conductivity with thick skin are shown in Fig. 4.8(a) and (b), while for thin skin, the values are shown in Fig. 4.8(c) and (d). We observed that permittivity and conductivity are same for both skin thicknesses under investigation and all tumor sizes, but when compared to experiments 1 and 2, permittivity and conductivity of tumor inside skin is less than tumor at the surface.



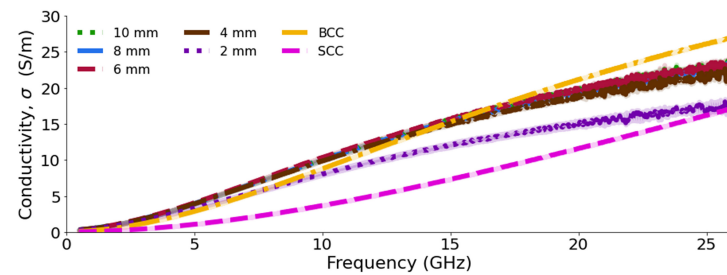
(a)



(b)



(c)



(d)

Fig. 4.7: Dielectric measurements of tumor raised out of skin compared with reference BCC and SCC tissues [36]. (a) Real relative permittivity, (b) conductivity of raised tumors with thick underlying skin, (c) real relative permittivity, and (d) conductivity of raised tumors with thin underlying skin.

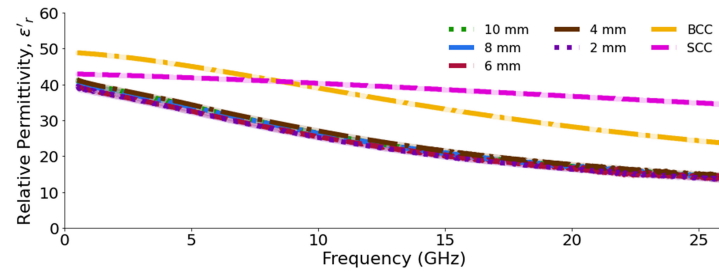
This is to be expected, as the probe now strives to measure combined dielectric property of the skin layer, with which it is in contact, and the underlying tumor lesion. As can be observed in Fig. 4.8, the dielectric response of the tumor in both thick and thin skin is closer to the BCC response in terms of conductivity at lower frequencies. Hence, the lower frequencies can be exploited for detection of subcutaneous tumor.

4.3.5 Experiment 5: Tumor with Irregular Border

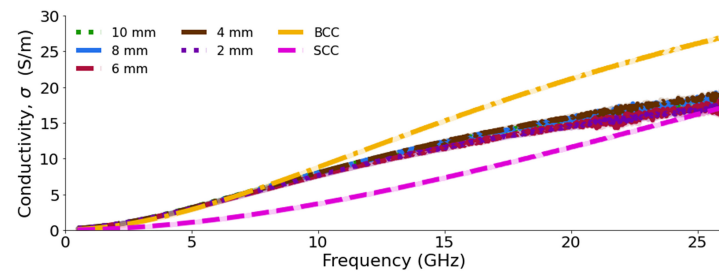
In this experiment, dielectric properties of tumor with irregular border are investigated. Two cases are taken in which tumor of diameter 10 mm and thickness of 2 mm with irregular border is placed within thick and thin underlying skin, flush with the skin surface in both cases.

Measurements are performed at the center and border of the tumor as shown in Fig. 4.9(a) and (b). For both thick and thin skin, it is observed that when tumor is measured at the center, it has higher permittivity and conductivity than tumor measured at the border. This could be because, when measured at the border, probe is sensing the surrounding skin dielectric properties along with the properties of tumor. When measured at the center, permittivity of tumors in both thick and thin skin shows close representation to BCC. Both tumors in thick and thin skin when measured at the border have permittivity less than both BCC and SCC but have conductivity closer to SCC value.

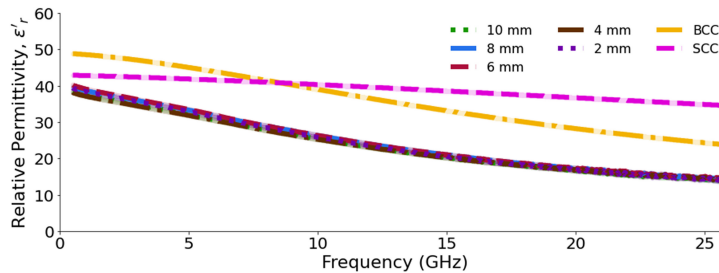
In this work, the measured skin phantom and tumor phantoms (10 mm (diameter) tumor



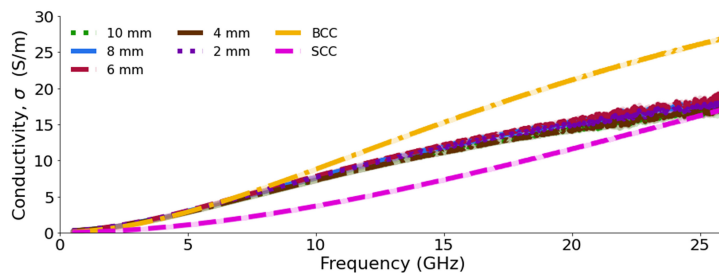
(a)



(b)



(c)



(d)

Fig. 4.8: Dielectric measurements of tumor inside the skin compared with reference BCC and SCC tissues [36]. (a) Real relative permittivity and (b) conductivity of tumors inside the thick skin (c) Real relative permittivity and (d) conductivity of tumors inside the thin skin.

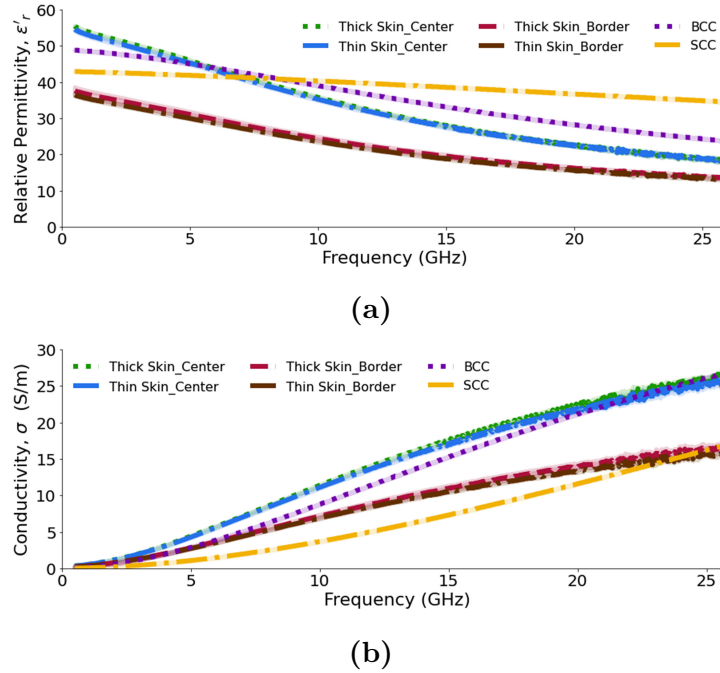


Fig. 4.9: Dielectric measurements of tumor with irregular border in thick and thin skin compared with reference BCC and SCC [36]. (a) Real relative permittivity and (b) conductivity measured at the center and border of tumor.

in align with thick (8 mm) skin and a 10 mm tumor in align with a thin (2.5 mm) skin, 10 mm tumor raised out of thick (8 mm) and thin (2.5 mm) skin and tumor inside thick (8 mm) and thin (2.5 mm) skin) are expressed by single pole Cole-Cole fitting as given in the equation 4.1. The fitting procedure was accomplished in MATLAB using `lsqcurvefit` and Levenberg-Marquardt algorithm. Calculated parameters are given in the Table 4.5.

The measured dielectric properties of skin and tumor phantoms are compared with the literature values for the skin (dry) from findings of Gabriel *et al.* [45] and reference dielectric data for BCC tumor tissue from [36]. It is observed that the mean measured

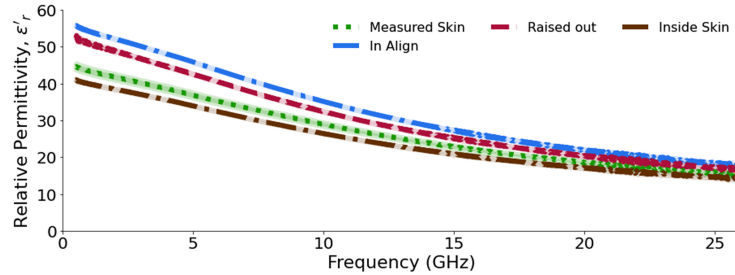
Table 4.5: Cole-cole parameters of the dielectric properties of the fabricated phantoms

Parameters	ε_{∞}	$\Delta\varepsilon$	τ (ps)	α	σ_s (S/m)
Skin	5.5510	38.0372	11.9338	0.0989	0.2045
Tumor in Align with Thick Skin	5.9774	48.6493	12.4133	0.0906	0.2597
Tumor in Align with Thin Skin	6.0522	47.8979	11.7061	0.0879	0.2754
Raised Tumor in Thick Skin	6.1730	45.1454	12.9771	0.0972	0.2471
Raised Tumor in Thin Skin	6.2264	43.5519	12.0248	0.1019	0.2447
Tumor inside Thick Skin	6.1698	33.8710	12.5115	0.0893	0.1756
Tumor inside Thin Skin	6.2744	31.1731	12.0570	0.0919	0.1743

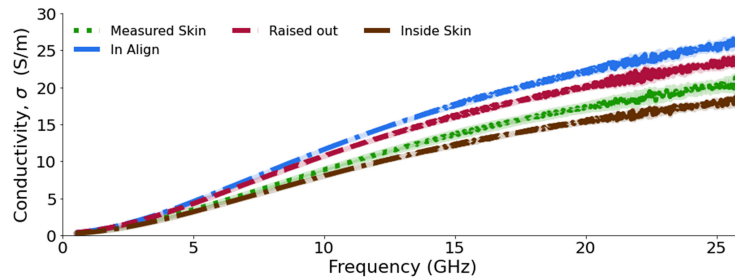
dielectric properties of skin phantoms make a close match with the reference dielectric properties. The average percentage difference was computed between real relative permittivity and conductivity of reference skin tissues and those of the skin phantom over 0.5–26.5 GHz, resulting in 11.1% for relative permittivity and 11.9% for conductivity.

In all tumor arrangements (10 mm tumor in alignment with the skin, raised out of the skin and embedded in the skin), the tumor phantoms have dielectric permittivity lower than the reference values. The average percentage difference between the relative permittivity and conductivity of reference data and proposed phantoms was found to be 14.8% and 33.5% for tumor in align with the skin, 18.9% and 28.3% for tumor raised out of the skin and 33.3% and 23.2% for tumor placed within the skin, respectively.

It is observed from the Fig. 4.10(a) and (b) that there is a contrast between dielectric properties of measured skin phantom and tumor phantoms. Tumor, with its surface planarly aligned with the skin and tumor surface raised out of the skin has higher dielectric properties



(a)



(b)

Fig. 4.10: Comparison of dielectric properties of the measured skin and tumor phantoms (10 mm tumor, planarly aligned with, raised out and embedded inside skin) (a) real relative permittivity (b) conductivity.

than measured skin phantoms. In the case of tumor embedded in the skin, the dielectric properties are lower than the measured skin phantom properties. This is because, the probe is averaging the tumor properties to those of the skin, with which it is in the immediate contact. The average percentage difference between the relative permittivity and conductivity of measured skin phantom and tumor phantoms are obtained to be 22.2% and 32%, respectively for tumor in align with the skin; 13.6% and 21.7%, respectively, for tumor raised out of the skin; 6.8% and 8.4%, respectively, for the case of the tumor embedded in the skin.

4.4 Conclusion

In this paper, a set of 32 experimental phantoms have been characterized in which tumors are combined with skin allowing suitable evaluation and validation of new prototypes for skin cancer detection.

The phantoms are fabricated using appropriate compositions of tissue-mimicking materials like oil, gelatin, deionized water and formaldehyde. These materials are selected due to their advantages as inexpensive, conformable to any shape and their utilization in heterogeneous phantom fabrication by combining materials without diffusion due to osmotic effects. The dielectric measurements of fabricated set of phantoms is carried out with Keysight performance probe which is further connected to vector network analyzer over the frequency range of 0.5–26.5 GHz.

Three cases have been investigated in which tumors are placed in align with the skin surface, raised out of skin and within the skin. In each of the cases described, five different tumor sizes (10 mm, 8 mm, 6 mm, 4 mm and 2 mm in diameter) are investigated for dielectric properties. To understand the effect of size (diameter and thickness) of underlying skin, two different sizes of skin were considered for each of the above-mentioned cases (8 mm – thick, and 2.5 mm – thin, skin). Lastly, a 10 mm tumor with irregular border was placed in both thick and thin skin and its dielectric properties were analyzed, thus making a total of 32 samples representing a variety of anatomical geometries. Thus, this work provides an array

of anatomically and dielectrically realistic phantom configurations with systematic variation in size of tumor, location and shape, not captured by previous experimental studies.

From the computed results, we observed that each fabricated phantom presents acceptable representation of reference excised samples obtained from literature. The validation of results indicate that the fabricated phantoms can be used for testing and development of new microwave skin cancer detection prototypes. Future studies will focus on numerical modeling of the dielectric probe for estimation of SAR (specific absorption rate) levels to confirm the compliance with the safety standards. This step will be vital for our near-future trials of skin and tumor lesions *in vivo*.

4.5 Acknowledgment

The authors are grateful to Analog Devices and Andre Beaulieu from Keysight for their support and training on the dielectric probe. We thank Leonardo Fortaleza (PhD student, McGill University) and Yanis Jallouli (Undergraduate student, McGill University) for their help in data analysis.

4.6 References

- [1] V. Madan, J. T. Lear, and R. M. Szeimies, “Non-melanoma skin cancer,” *Lancet*, vol. 375, no. 9715, pp. 673–685, Feb. 2010.
- [2] Skin Cancer Facts & Statistics, Skin Cancer Foundation, 2022, Accessed: Feb. 4, 2022. [Online]. Available: <https://www.skincancer.org/skin-cancer-information/skin-cancer-facts/>
- [3] R. P. Braun, J. Mangana, S. Goldinger, L. French, R. Dummer, and A. A. Marghoob, “Electrical impedance spectroscopy in skin cancer diagnosis,” *Dermatologic Clin.*, vol. 35, no. 4, pp. 489–493, Oct. 2017.
- [4] M. E. Vestergaard, P. Macaskill, P. E. Holt, and S. W. Menzies, “Dermoscopy compared with naked eye examination for the diagnosis of primary melanoma: A meta-analysis of studies performed in a clinical setting,” *Br J. Dermatol.*, vol. 159, no. 3, pp. 669–676, Sep. 2008.
- [5] C. R. Hill and G. R. Ter Haar, “High intensity focused ultrasound-potential for cancer treatment,” *Brit. J. Radiol.*, vol. 68, no. 816, pp. 1296–1303, Dec. 1995.
- [6] A. C. Kak and M. Slaney, “Principles of computerized tomographic imaging,” in *Classics in Applied Mathematics*, R. F. Cotellessa, Ed., New York, NY, USA: IEEE Press, 1988.

-
- [7] V. Narayanamurthy et al., “Skin cancer detection using non-invasive techniques,” *RSC Adv.*, vol. 8, no. 49, pp. 28095–28130, Aug. 2018, doi: 10.1039/C8RA04164D.
- [8] H. D. Heibel, L. Hooey, and C. J. Cockerell, “A review of noninvasive techniques for skin cancer detection in dermatology,” *Amer. J. Clin. Dermatol.*, vol. 21, no. 4, pp. 513–524, Aug. 2020, doi: 10.1007/s40257-020-00517-z.
- [9] S. K. Parsons et al., “Noninvasive diagnostic techniques for the detection of skin cancers,” *Effective Health Care Program*, vol. 11, no. 11, pp. 1–41, Sep. 2011.
- [10] R. Ashraf et al., “Region-of-interest based transfer learning assisted framework for skin cancer detection,” *IEEE Access*, vol. 8, pp. 147858–147871, Aug. 2020, doi: 10.1109/ACCESS.2020.3014701.
- [11] C. Barata, M. E. Celebi, and J. S. Marques, “A survey of feature extraction in dermoscopy image analysis of skin cancer,” *IEEE J. Biomed. Health Inform.*, vol. 23, no. 3, pp. 1096–1109, May 2019, doi: 10.1109/JBHI.2018.2845939.
- [12] Y. Fujisawa, S. Inoue, and Y. Nakamura, “The possibility of deep learningbased, computer-aided skin tumor classifiers,” *Front. Med.*, vol. 6, Aug. 2019, Art. no. 191.
- [13] M. Patlak, S. J. Nass, I. C. Henderson, and J. C. Lashof, Eds. *Mammography and Beyond: Developing Techniques for The Early Detection of Breast Cancer*. Washington, DC, USA: National Academies Press., 2001.

- [14] B. J. Mohammed, A. M. Abbosh, S. Mustafa, and D. Ireland, "Microwave system for head imaging," *IEEE Trans. Instrum. Meas.*, vol. 63, no. 1, pp. 117–123, Jan. 2014, doi: 10.1109/TIM.2013.2277562.
- [15] E. C. Fear, J. Bourqui, C. Curtis, D. Mew, B. Docktor, and C. Romano, "Microwave breast imaging with a monostatic radarbased system: A study of application to patients," *IEEE Trans. Microw. Theory Techn.*, vol. 61, no. 5, pp. 2119–2128, May 2013, doi: 10.1109/TMTT.2013.2255884.
- [16] C. Dachena, A. Fedeli, A. Fanti, M. B. Lodi, M. Pastorino, and A. Randazzo, "Microwave imaging for the diagnosis of cervical diseases: feasibility analysis," *IEEE J. Electromagn., RF Microw. Med. Biol.*, vol. 5, no. 3, pp. 277–285, Sep. 2021.
- [17] S. Alani, Z. Zakaria, T. Saeidi, A. Ahmad, M. A. Imran, and Q. H. Abbasi, "Microwave imaging of breast skin utilizing elliptical UWB antenna and reverse problems algorithm," *Micromachines*, vol. 12, no. 6, pp. 647–663, May 2021.
- [18] S. Castelló-Palacios, C. Garcia-Pardo, A. Fornes-Leal, N. Cardona, and A. Vallés-Lluch, "Tailor-made tissue phantoms based on acetonitrile solutions for microwave applications up to 18 GHz," *IEEE Trans. Microw. Theory Techn.*, vol. 64, no. 11, pp. 3987–3994, Nov. 2016, doi: 10.1109/TMTT.2016.2608890.
- [19] A. R. Guraliuc, M. Zhadobov, O. De Sagazan, and R. Sauleau, "Solid phantom for body-centric propagation measurements at 60 GHz," *IEEE Trans. Microw. Theory*

- Techn.*, vol. 62, no. 6, pp. 1373–1380, Jun. 2014, doi: 10.1109/TMTT.2014.2320691.
- [20] S. Di Meo et al., “Tissue-mimicking materials for breast phantoms up to 50 GHz,” *Phys. Med. Biol.*, vol. 64, no. 5, Feb. 2019, Art. no. 055006, doi: 10.1088/1361-6560/aafeec.
- [21] S. Castelló-Palacios, C. Garcia-Pardo, M. Alloza-Pascual, A. FornesLeal, N. Cardona, and A. Vallés-Lluch, “Gel phantoms for body microwave propagation in the (2 to 26.5) GHz frequency band,” *IEEE Trans. Antennas Propag.*, vol. 67, no. 10, pp. 6564–6573, Oct. 2019, doi: 10.1109/TAP.2019.2920293.
- [22] M. Lazebnik, E. L. Madsen, G. R. Frank, and S. C. Hagness, “Tissue-mimicking phantom materials for narrowband and ultrawideband microwave applications,” *Phys. Med. Biol.*, vol. 50, no. 18, pp. 4245–4258, Sep. 2005.
- [23] L. Huang et al., “A leg phantom model based on the visible human data for intra-body communication,” *IEEE J. Electromagn., RF Microw. Med. Biol.*, vol. 5, no. 4, pp. 313–321, Dec. 2021, doi: 10.1109/JERM.2020.3043955.
- [24] B. Amin, A. Shahzad, D. Kelly, M. O’Halloran, and M. A. Elahi, “Anthropomorphic calcaneus phantom for microwave bone imaging applications,” *IEEE J. Electromagn., RF Microw. Med. Biol.*, vol. 5, no. 3, pp. 206–213, Sep. 2021, doi: 10.1109/JERM.2020.3029938.

- [25] K. S. Sultan, B. Mohammed, P. C. Mills, and A. Abbosh, "Anthropomorphic durable realistic knee phantom for testing electromagnetic imaging systems," *IEEE J. Electromagn., RF Microw. Med. Biol.*, vol. 5, no. 2, pp. 132–138, Jun. 2021, doi: 10.1109/JERM.2020.3023027.
- [26] A. Malliori, A. Daskalaki, A. Dermitzakis, and N. Pallikarakis, "Development of physical breast phantoms for X-ray imaging employing 3D printing techniques," *Open Med. Imag. J.*, vol. 12, pp. 1–10, 2020.
- [27] M. Lazebnik et al., "A large-scale study of the ultrawideband microwave dielectric properties of normal, benign and malignant breast tissues obtained from cancer surgeries," *Phys. Med. Biol.*, vol. 52, no. 20, pp. 6093–6115, Oct. 2007.
- [28] J. Lacik, V. Hebelka, J. Velim, Z. Raida, and J. Puskely, "Wideband skin-equivalent phantom for V- and W-Band," *IEEE Antennas Wireless Propag. Lett.*, vol. 15, pp. 211–213, Jun. 2015, doi: 10.1109/LAWP.2015.2438441.
- [29] A. T. Mobashsher and A. M. Abbosh, "Artificial human phantoms: Human proxy in testing microwave apparatuses that have electromagnetic interaction with the human body," *IEEE Microw. Mag.*, vol. 16, no. 6, pp. 42–62, Jul. 2015, doi: 10.1109/MMM.2015.2419772.
- [30] R. Aminzadeh, M. Saviz, and A. A. Shishegar, "Theoretical and experimental broadband tissue-equivalent phantoms at microwave and millimetrewave frequencies,"

- Electron. Lett.*, vol. 50, no. 8, pp. 618–620, Apr. 2014.
- [31] A. Mirbeik-Sabzevari and N. Tavassolian, “Ultrawideband, stable normal and cancer skin tissue phantoms for millimeter-wave skin cancer imaging,” *IEEE Trans. Biomed. Eng.*, vol. 66, no. 1, pp. 176–186, Jan. 2019, doi: 10.1109/TBME.2018.2828311.
- [32] A. Mirbeik-Sabzevari, S. Li, E. Garay, H. T. Nguyen, H. Wang, and N. Tavassolian, “Synthetic ultra-high-resolution millimeter-wave imaging for skin cancer detection,” *IEEE Trans. Biomed. Eng.*, vol. 66, no. 1, pp. 61–71, Jan. 2019, doi: 10.1109/TBME.2018.2837102.
- [33] B. Khalesi, G. Tiberi, N. Ghavami, M. Ghavami, and S. Dudley, “Skin cancer detection through microwaves: Validation on phantom measurements,” in *Proc. IEEE Int. Conf. Imag. Syst. Techn.*, 2018, pp. 1–6, doi: 10.1109/IST.2018.8577109.
- [34] L. Kranold, J. Boparai, L. Fortaleza, and M. Popović, “A comparative study of skin phantoms for microwave applications,” in *Proc. 42nd Annu. Int. Conf. IEEE Eng. Med. Biol. Soc.*, Jul. 2020, pp. 4462–4465.
- [35] J. Boparai, L. Kranold, L. Fortaleza, and M. Popović, “Dielectric properties of skin-mimicking tissue models in the 5–20 GHz range,” in *Proc. IEEE Int. Symp. Antennas Propag. North Amer. Radio Sci. Meeting*, Jul. 2020, pp. 1623–1624.
- [36] A. Mirbeik-Sabzevari, R. Ashinoff, and N. Tavassolian, “Ultra-wideband millimeter-

- wave dielectric characteristics of freshly excised normal and malignant human skin tissue,” *IEEE Trans. Biomed. Eng.*, vol. 65, no. 6, pp. 1320–1329, Jun. 2018, doi: 10.1109/TBME.2017.2749371.
- [37] E. Porter, J. Fakhoury, R. Oprisor, M. Coates, and M. Popović, “Improved tissue phantoms for experimental validation of microwave breast cancer detection,” in *Proc. 4th Eur. Conf. Antennas Propag.*, 2010, pp. 1–5.
- [38] P. Oltulu, B. Ince, N. Kokbudak, S. Findik, and F. Kilinc, “Measurement of epidermis, dermis, and total skin thicknesses from six different body regions with a new ethical histometric technique,” *Turkish J. Plast. Surg.*, vol. 26, no. 2, pp. 56–61, 2018.
- [39] A. Laurent et al., “Echographic measurement of skin thickness in adults by high frequency ultrasound to assess the appropriate microneedle length for intradermal delivery of vaccines,” *Vaccine*, vol. 25, no. 34, pp. 6423–6430, Aug. 2007.
- [40] S. P. Paul, “Micromelanomas: A review of melanomas ≤ 2 mm and a case report,” *Case Rep. Oncological Med.*, vol. 2014, 2014, Art. no. 206260, doi: 10.1155/2014/206260.
- [41] A. Bono et al., “Small nodular melanoma: The beginning of a lifethreatening lesion. A clinical study on 11 cases,” *Tumori J.*, vol. 97, no. 1, pp. 35–38, 2011.
- [42] T. Wortman, F. Hsu, and A. Slocum, “A novel phantom tissue model for skin elasticity quantification,” *J. Med. Devices*, vol. 10, no. 2, Jun. 2016.

-
- [43] P. Roma et al., “Slow-growing melanoma: Report of five cases,” *J. Dermatological Case Rep.*, vol. 1, no. 1, pp. 1–3, Dec. 2007, doi: 10.3315/jdcr.2007.1.1001.
- [44] J. M. Firnhaber, “Diagnosis and treatment of basal cell and squamous cell carcinoma,” *Amer. Fam. Physician*, vol. 86, no. 2, pp. 161–168, Jul. 2012.
- [45] C. Gabriel and A. Peyman, “Dielectric measurement: Error analysis and assessment of uncertainty,” *Phys. Med. Biol.*, vol. 51, no. 23, pp. 6033–6046, Dec. 2006.
- [46] B. N. Taylor and C. E. Kuyatt, *Guidelines for Evaluating and Expressing the Uncertainty of NIST Measurement Results*. US Dept. Commerce, Tech. Administration, Nat. Inst. Std. Tech., 1994.
- [47] A. L. Gioia, S. Salahuddin, M. O’Halloran, and E. Porter, “Quantification of the sensing radius of a coaxial probe for accurate interpretation of heterogeneous tissue dielectric data,” *IEEE J. Electromagn., RF Microw. Med. Biol.*, vol. 2, no. 3, pp. 145–153, Sep. 2018, doi: 10.1109/JERM.2018.2841798.

Chapter 5

Heterogeneous Skin Phantoms for Experimental Validation of Microwave-Based Diagnostic Tools

This chapter is based on the following publication:

J. Boparai and M. Popović, “Heterogeneous Skin Phantoms for Experimental Validation of Microwave-Based Diagnostic Tools,” *Sensors*, vol. 22, pp. 1955, 2022.

Preface to Chapter 5: The focus of work reported in this chapter was the development of phantoms that dielectrically and anatomically represent skin and selected lesions. Emulating such configurations will eventually improve the capability of emerging skin cancer diagnostic prototypes in identifying rare skin conditions, along with diagnosing commonly occurring skin cancer types.

Thus, in this work, we developed and examined dielectric performance of phantom models immitating rare malignant skin lesions, liposarcoma and nonsyndromic multiple

basal cell carcinoma. Moreover, to realize anatomically realistic scenarios and for meaningful comparison, we inserted cancer-mimicking lesions in two different types of skin-mimicking phantoms in three different tumor-skin geometrical arrangements. Further, the two tumor sizes (10 mm and 2 mm in diameter) were selected to analyze the probe's detection capability with tumor size variation, as it implies variation of the complex dielectric distribution in the sensing volume of the probe.

The phantom models were validated by comparing the measured dielectric properties with the reference dielectric properties of excised tissues. The obtained results indicated that the dielectric probe has the ability to identify the cancerous lesions including an occurrence of rare lesions, liposarcoma and nonsyndromic multiple basal cell carcinoma. Additionally, with different heterogeneous tumor-skin geometrical arrangements, there is a presence of different dielectric distributions within the sensing volume of the probe and the probe was able to identify tumor lesions in these scenarios.

Abstract—Considerable exploration has been done in recent years to exploit the reported inherent dielectric contrast between healthy and malignant tissues for a range of medical applications. In particular, microwave technologies have been investigated towards new diagnostic medical tools. To assess the performance and detection capabilities of such systems, tissue-mimicking phantoms are designed for controlled laboratory experiments. We here report phantoms developed to dielectrically represent malign skin lesions such as

liposarcoma and nonsyndromic multiple basal cell carcinoma. Further, in order to provide a range of anatomically realistic scenarios, and provide meaningful comparison between different phantoms, cancer-mimicking lesions are inserted into two different types of skin phantoms with varying tumor–skin geometries. These configurations were measured with a microwave dielectric probe (0.5–26.5 GHz), yielding insight into factors that could affect the performance of diagnostic and detection tools.

Index Terms—biological tissues; dielectric properties; dielectric measurement; liposarcoma; microwaves; nonsyndromic basal cell carcinoma (BCC); tissue-mimicking phantoms; tumor

5.1 Introduction

Over the past decade, microwave reflectometry techniques have been researched for diagnosis and early-stage characterization of malignancies such as subcutaneous masses, skin burn injuries and cancerous lesions in the brain, breast and skin [1–5]. In particular, we focus on techniques that exploit the reported inherent dielectric contrast of healthy and malignant tissues in the microwave frequency range [6,7] to identify cancerous lesions or anomalies. Low-power microwave-based techniques have the advantages of being safe, cost effective and portable. The current modalities which are considered as gold standards, such as magnetic resonance imaging (MRI), X-rays, computed tomography methods or CT scanning and ultrasound, each have their shortcomings. For example: X-rays and CT scans

involve ionizing radiation, limiting frequent screening; MRI is expensive and not suitable for frequent mass screenings; ultrasound imaging is operator-dependent and requires real-time interpretation [8–12]. Further, nonspecificity of available techniques for skin cancer requires biopsies, which are uncomfortable to the patient and invasive. The goal of microwave-based diagnosis is to provide additional insight into the nature of the lesion under investigation, thereby reducing the number of needed biopsies [13]. The development of microwave-based systems for the accurate characterization of abnormalities can assist the physician in diagnostics by providing additional information that can facilitate decision-making with improved confidence. Consequently, the possibly cancerous anomalies can be identified at their early stage, increasing the success rate of the subsequent treatment.

Successful adoption of microwave diagnostic systems requires their systematic testing and validation in a controlled laboratory environment. Here, well-designed tissue phantoms play an important role in the preclinical trial stage. Based on different material compositions, fabrication processes, complexity, stability and cost, several tissue-mimicking phantoms have been reported. These phantoms vary considerably in their shape and structure, ranging from simple geometries such as homogeneous models to heterogeneous models with realistic shapes. In Ref. [14], the authors realized several human tissues with acetonitrile mixtures over the wide frequency range from 0.5 to 18 GHz. In the study of [15], Triton X-100 and distilled water solutions were investigated over a wide-band frequency to reproduce

the dielectric properties of different types of breast tissues. In addition to being subject to dehydration, the liquid-based phantoms pose a challenge for inhomogeneous structure construction [16]. Garrett and Fear proposed carbon and rubber mixtures-based phantoms, which exhibit a wide range of dielectric properties and hence mimic a variety of tissues up to 10 GHz [17,18]. Although these phantoms are electrically and mechanically stable, their material composition is expensive and the fabrication process is complex [19]. In addition, semisolid phantoms are widely adopted for emulating various tissues like fat, muscle and skin due to their ability to achieve better approximations of the targeted tissues. The heterogeneous and stable breast phantom composed of multiple tissues such as skin, fat, muscle and spherical inclusion was reported in [20]. Jelly-type or semisolid-type materials mimicking the dielectric properties of human skin tissues are also commercially available [21]. These are stable over a longer period of time. Recently, there has been an increasing interest in easily reproducible 3D-printed phantoms; however, often the materials that are used in their fabrication are not dielectrically characterized [22]. Previously, we constructed and characterized tumors in skin with diameter sizes ranging from 2 mm to 10 mm at 2 mm increments with underlying thick and thin skin along with irregular-shaped tumor [23].

Our present study is motivated by the need for stable, anatomically and dielectrically accurate heterogeneous phantoms that emulate rare and realistic configurations. This will contribute to the improvement of the efficacy of the emerging diagnostic devices in screening such rare cases, along with the frequently occurring skin cancer forms. Thus, in this work,

we present a methodology of constructing phantoms imitating realistic scenarios such as liposarcoma and nonsyndromic multiple basal cell carcinoma [24–27]. Liposarcoma is a rare type of cancer which sometimes develops as a subcutaneous mass in the fat layer just below the skin. It can begin anywhere in the body but is most commonly found in the abdomen, thigh and behind the knee. Additionally, in some rare conditions like nonsyndromic multiple basal cell carcinoma, an individual can develop multiple lesions at once. Often, surgical excision is advised to identify the nature of tumor or diagnose the lesion with the help of X-rays, MRI, CT scan or ultrasound. In certain cases, there is a risk associated with surgical removal, for example, ruptured lesions can leave cells behind in the tissue which can be carried to other parts of the body through the bloodstream. Microwave techniques based on nonionizing radiation, and low in power, hold promise as diagnostic aids which could help the dermatologist in the decision-making process and in the detection of the subcutaneous lesions. In order to test the capability of microwave diagnostic tools in distinguishing lesions from healthy skin, we constructed phantoms by incorporating tumors in two different types of skin: oil–gelatin (fabricated in-house) and Probingon AB (commercially available). Each phantom model was tested with two tumor sizes: 10 mm and 2 mm in diameter, and 2 mm in thickness for both cases.

5.2 Materials and Methods

5.2.1 Modeling of phantoms

For our study, we emulated rare conditions like liposarcoma and multiple basal cell carcinoma with oil-in-gelatin-based tissue-mimicking materials that have the ability to accurately emulate the dispersive dielectric properties (the frequency dependence of parameter values) of human tissues such as skin, fat and tumor. Moreover, with these materials, we realized heterogeneous configurations to construct realistic anatomical structures to be characterized over the wide frequency range. The oil-gelatin phantoms were fabricated according to the guidelines published in [28]. For completeness, the fabrication procedure is illustrated in Fig. 5.1 and the corresponding steps are briefly listed in Table 5.1.

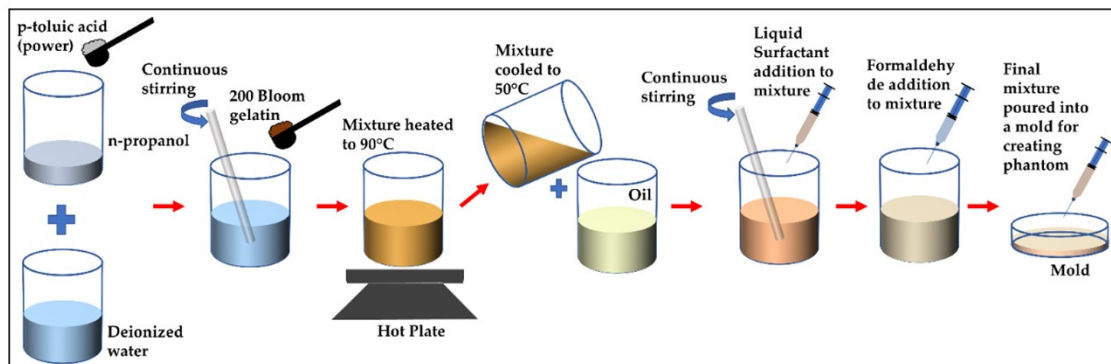


Fig. 5.1: Illustration of fabrication procedure for proposed oil-gelatin phantoms.

To represent the liposarcoma condition, the phantoms were constructed in three stages.

Table 5.1: A summary of steps for constructing oil-in-gelatin-based phantoms.

Step 1.	Add p-toluic acid to n-propanol and heat the solution.
Step 2.	Mix solution of p-toluic acid and n-propanol to deionized water at room temperature.
Step 3.	Add gelatin to the obtained mixture and heat the mixture at 90 °C until it becomes transparent.
Step 4.	Cool the mixture in water bath to 50 °C.
Step 5.	Mix oil (50% safflower and 50% kerosene) separately and heat up to 50 °C.
Step 6.	Combine mixtures of step 4 & 5.
Step 7.	Add Ultra Ivory and formaldehyde to above mixture.
Step 8.	Pour the resultant mixture into mold and allow it to solidify.

In the first stage, we created a fat layer by pouring the fat-mimicking material into the cylindrical mold and a coin-shaped (small, shallow cylinder) void was left at the top of the fat surface, later to be filled up with the tumor-mimicking material. Before proceeding to the next stage, we left the fat to congeal for 24 hours. In the second stage, the void was filled with the tumor-like material and allowed to congeal overnight. In the final stage, skin-like material was added on the top of the fat-layer-containing tumor. The thickness of the subcutaneous fat and skin layer varies depending upon number of factors such as body location, age and gender [29,30]. For this case, we selected the thickness of fat and skin to be 7 mm and 1 mm, respectively, and the diameter of 38.5 mm, which is the diameter of container mold. The two tumor sizes considered for comparison were 10 mm and 2 mm in diameter, each with a 2 mm thickness.

For simulating the condition with multiple BCC lesions, we followed similar steps as mentioned above. In the first stage, the skin-like material is poured into the container with

two coin-shaped voids left at the top surface of the skin, which are later filled with the tumor-mimicking material. In this case, the skin thickness is 2.5 mm and diameter of the entire testing sample is 38.5 mm. Both tumors have a thickness of 2 mm and a diameter of 10 mm. The sketch and the fabricated phantoms depicting both conditions are shown in Fig. 5.2. These phantoms have a shelf-life of several weeks when plastic-wrapped or placed in an airtight container. The phantoms are fabricated according to the compositions in Table 5.2 [31].

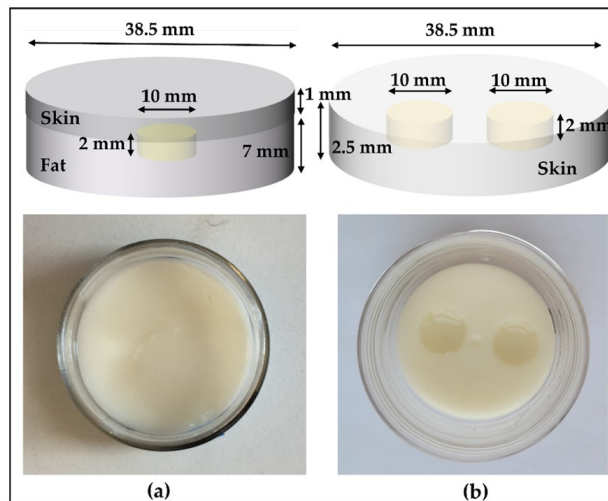


Fig. 5.2: Oil-gelatin phantoms, with sketches shown on the top and the top-view photograph on the bottom: (a) Tumor (10 mm) embedded in fat underneath the skin and (b) multiple tumors in skin.

In an additional experiment, we incorporated tumors in two different skin-mimicking materials: oil-gelatin (following the recipe above) and the Probingon AB [32]. The latter is a commercially available skin phantom with a jelly-like consistency, allowing us to easily incorporate the tumors, and has been characterized for skin-like dielectric properties in the

Table 5.2: Composition used in the fabrication of phantoms shown in Fig. 5.2 [31].

Target Tissue	p-Toluic Acid (g)	n-Propanol (mL)	Deionized Water (mL)	200 Bloom Gelatin (g)	Formadehyde (37% by Weight) (g)	Oil (mL)	Ultra-Ivory Detergent (mL)
Fat	0.133	6.96	132.7	24.32	1.53	265.6	12.0
Skin	0.294	28.69	279.5	50.02	3.33	98.6	5.86
Tumor	0.346	17.0	328.0	58.67	3.72	38.4	2.00

microwave range. We considered three different tumor-skin arrangements: tumor with a top surface coplanar with the skin, tumor within the skin, and tumor raised slightly above the plane of the skin surface. The thickness and diameter of each skin phantom are 2.5 mm and 38.5 mm, respectively. Each tumor phantom was 2 mm thick with two diameter sizes: 10 mm and 2 mm. To avoid dehydration, the phantoms were plastic-wrapped, placed in air-tight containers and stored in the refrigerator.

Fig. 5.3 shows the photograph of both types of skin (oil-gelatin and Probingon AB) with oil-gelatin tumors raised beyond, aligned with the skin surface and embedded within the skin.

5.2.2 Characterization Methodology

The dielectric properties of the proposed tissue-mimicking phantoms were measured using an open-ended coaxial probe [33]. The measurement system (Fig. 5.4) consists of a performance probe (Keysight Technologies, model N1501A) suitable for semisolid materials and a vector network analyzer (VNA) (Keysight Technologies, model N9918A, commonly

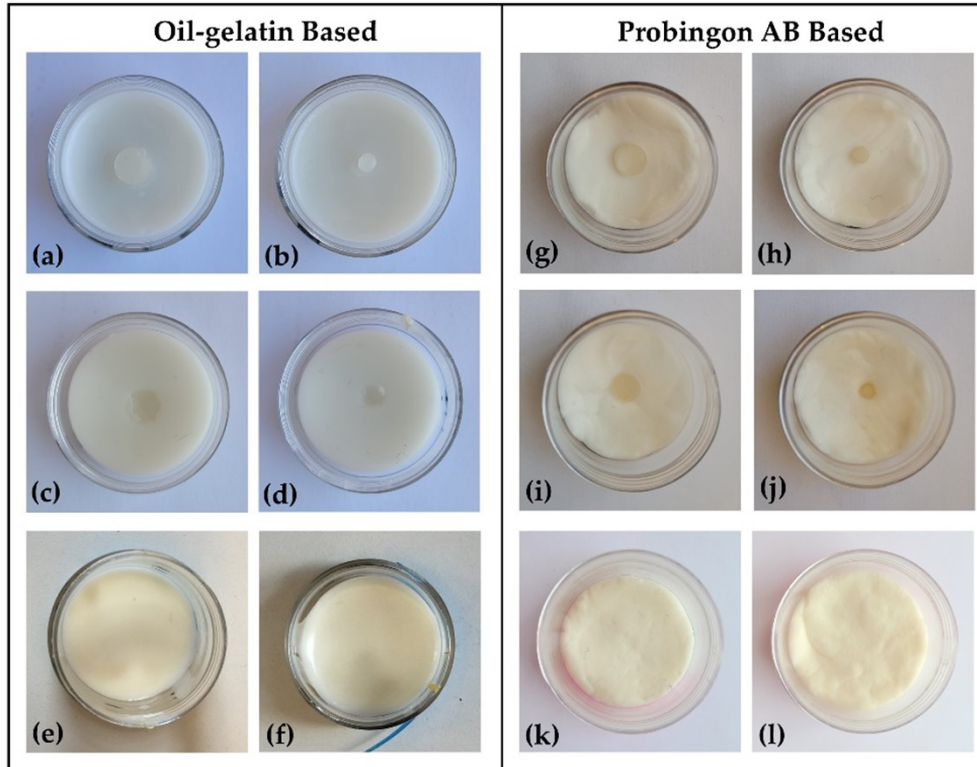


Fig. 5.3: Photograph (top view) of oil-gelatin tumor phantoms in (a–f) oil-gelatin and (g–l) Probingon AB skin. Two tumor sizes in three arrangements are shown: 10 mm diameter (a,g) raised out of skin; (c,i) aligned with the skin surface; (e,k) embedded within the skin; with the same arrangements are shown for the smaller 2 mm tumor in figures (b,h); (d,j); (f,l), respectively.

known as FieldFox Handheld Microwave Analyzer [34]). The open-ended performance probe is connected to the port of the VNA with a coaxial cable which is flexed and stabilized before calibration and measurements. The probe is locked in the mounting bracket of the probe stand to minimize the movement-induced reading errors. A sample elevator stage was used to move the sample under test towards the probe. The dielectric measurements were carried out over the entire VNA frequency range, 500 MHz–26.5 GHz,

and over 1001 frequency points. The reflection coefficient (S11) obtained from the VNA are converted to real (ϵ'_r) and imaginary part (ϵ''_r) of complex permittivity (ϵ_r) using Keysight's materials measurement N1500A software suite. All measurements were performed at room temperature (23 °C).

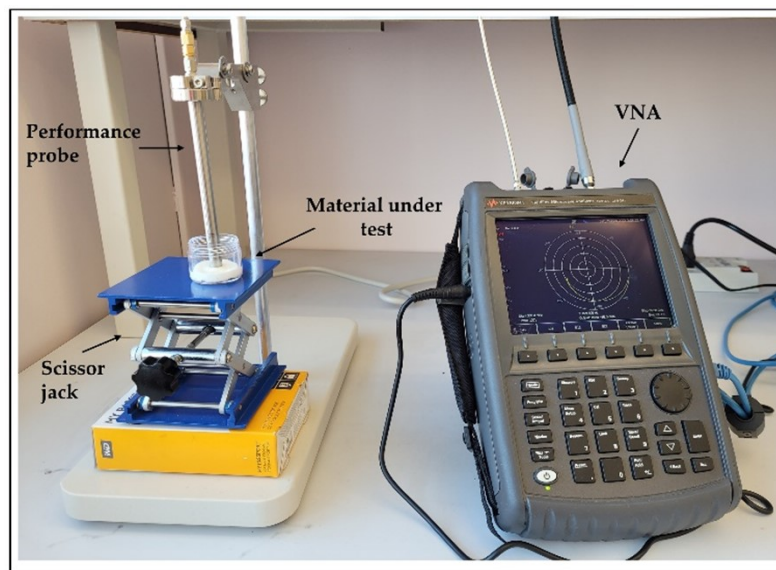


Fig. 5.4: Dielectric measurement setup showing the open-ended performance coaxial probe (left) and a FieldFox vector network analyzer; material under test (MUT) is placed on scissor jack.

A standard three-load calibration using air, short (metal block in Keysight probe kit) and load (deionized water) was used before conducting the measurement of the dielectric properties. The calibration was validated by measuring the dielectric properties of known materials (deionized water and air) before and after each measurement. Calibration was refreshed between the repeated measurements to increase the measurement accuracy, and air was used as the refreshing standard. The power level used was -10 dBm.

Uncertainty analysis was done at each frequency by computing the repeatability and accuracy, as reported in [35,36]. Error due to drift and cable movement is not included in the measurements since our setup is fixed. Repeatability was calculated as the standard deviation of mean of 10 repeated measurements on deionized water and averaging the values over the complete frequency range. Accuracy is calculated as the average percentage difference between the measured values and the reference models reported in the literature over the entire frequency range of 500 MHz to 26.5 GHz. In our study, we tested the accuracy of the measurements using deionized water, as it has well-known dielectric properties presented in the literature [37]. Repeatability uncertainty for permittivity and conductivity was calculated as 0.26% and 0.45%, respectively. Accuracy uncertainty was determined to be 1.78% for permittivity and 1.47% for conductivity. This resulted in the total combined uncertainty of 1.8% and 1.5% for permittivity and conductivity, respectively.

5.2.3 Results and Discussion

In this section, we have assessed the dielectric measurement results of the proposed tissue-mimicking phantoms and validated them using reference models obtained from the literature. Since the dielectric properties are dependent on frequency and temperature, we monitored the temperature of the calibration and validation liquid, i.e., deionized water and the temperature of the sample under test (22.7 ± 0.4 °C), thus ensuring consistent

Table 5.3: One pole cole-cole parameters to compute dielectric data of malignant BCC and fat from literature.

Tissue Type	ε_∞	$\Delta\varepsilon$	τ (ps)	σ_s (S/m)	α
Malignant BCC [38]	6	43.04	7.66	0.05	0.08
Fat Group 3 [39]	4.031	3.645	14.12	0.083	0.055

measurements temperature-wise. The complex permittivity (ε_r), which is comprised of real (ε_r') and imaginary (ε_r'') parts representing the relative permittivity and loss factor, respectively, of the realized phantom models, was computed at room temperature following the guidelines of MINDER [38].

The conductivity (σ_s) is related to the loss factor (ε_r'') and computed using Equation (5.1) as

$$\sigma_s = 2\pi f \varepsilon_r'' \varepsilon_0 \quad (5.1)$$

where f is the frequency of the operation in hertz and ε_0 (8.854×10^{-12} farad/meter) is the permittivity of free space. The dielectric properties of the reference malignant BCC [39] and fat [40] tissues were obtained using the one pole Cole–Cole model described in Equation (5.2) and the Cole–Cole parameters given in Table 5.3.

$$\varepsilon_r = \varepsilon_r' - j\varepsilon_r'' = \varepsilon_\infty + \frac{\Delta\varepsilon}{1 + (j\omega\tau)^{1-\alpha}} + \frac{\sigma_s}{j\omega\varepsilon_0} \quad (5.2)$$

where $\omega = 2\pi f$ is the angular frequency in radians per second, ε_∞ is permittivity of skin at optical frequencies, $\Delta\varepsilon$ is magnitude of skin dielectric dispersion, τ (ps) is the relaxation

time, α is the measure of broadening dispersion and σ_s (S/m) is the skin conductivity. The Cole–Cole parameters (ε_∞ , $\Delta\varepsilon$, τ , α , σ_s) are determined by minimizing the function given as:

$$c = \frac{\sum_{i=1}^N \left| \frac{\varepsilon'_r(\omega_i) - \varepsilon'_{rc}(\omega_i)}{(\varepsilon'_r(\omega_i))} \right| + \sum_{i=1}^N \left| \frac{\varepsilon''_r(\omega_i) - \varepsilon''_{rc}(\omega_i)}{(\varepsilon''_r(\omega_i))} \right|}{N} \quad (5.3)$$

where N is the number of frequency points, $\varepsilon'_r(\omega_i)$ and $\varepsilon''_r(\omega_i)$ are values measured at frequency (ω_i) and the values of $\varepsilon'_{rc}(\omega_i)$ and $\varepsilon''_{rc}(\omega_i)$ are obtained from (5.2). The fitting procedure is performed in MATLAB using the Levenberg-Marquardt algorithm [39].

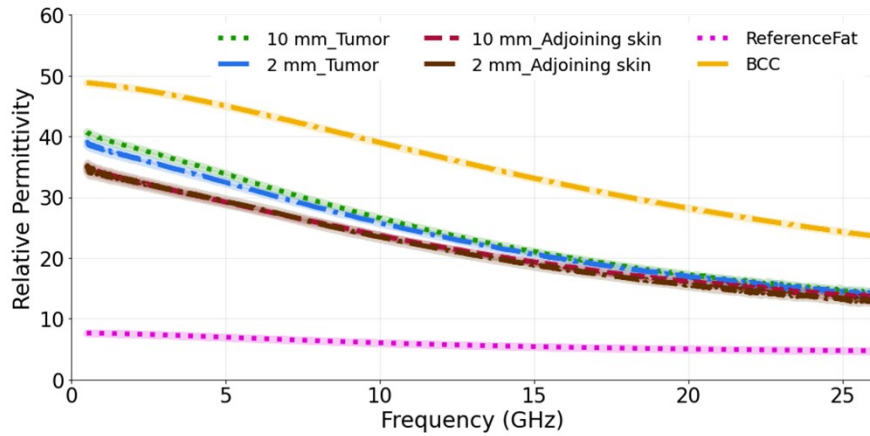
The resulting data, shown in the sections that follow, are plotted with mean and standard deviations in measurements across the complete microwave frequency range of interest. We performed 10 consecutive measurements on each MUT by placing the probe at the same point and mean, and two standard deviations are calculated. The mean values are represented by lines and these lines are bordered by \pm standard deviations (95.5% confidence interval) represented by a shaded area. Before and after the MUT dielectric measurement, the procedure was recalibrated by measuring the dielectric properties of known materials (air and deionized water). We divided our measurement study in three parts, as detailed in the following subsections.

5.2.4 Study 1: Tumors Embedded within the Fat–Skin Layer—Liposarcoma

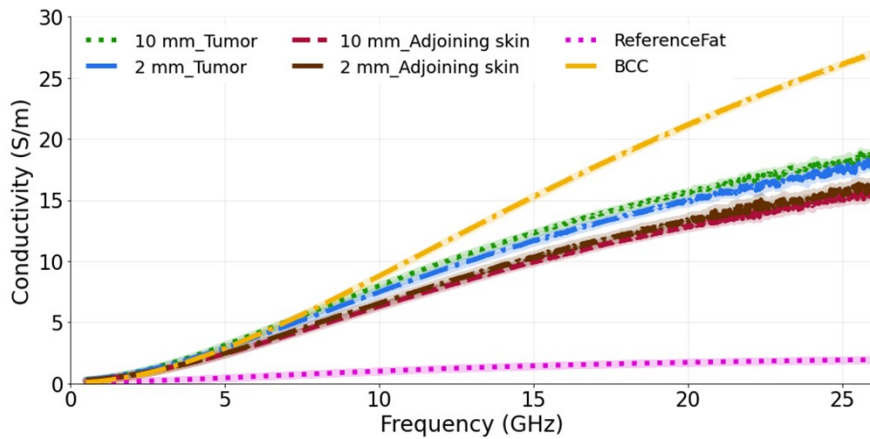
In our first study, we measured phantom models emulating the liposarcoma condition.

This study was done to analyze the dielectric response when the lesion is in the fat layer underneath the skin. Two separate models were taken: one with a 10 mm tumor (diameter) and the other with a 2 mm tumor (diameter) to observe the ability of the probe to sense large and small tumors. The thickness of both tumors is 2 mm. The probe was held lightly against the skin under which the tumor was present, and it was ensured that the entire aperture of the probe was in contact with the skin. The relative permittivity and conductivity are plotted in Fig. 5.5 a, b. From the graphs, it is observed that the measured dielectric values are nearly the same for the two tumor sizes. The measurements were also performed on the adjoining skin of each tumor and it can be seen that there is a slight difference in the dielectric properties of the adjoining skin and the tumor phantoms up to a frequency of 15 GHz in terms of permittivity, which can be utilized to identify the lesion. This difference shows that the underlying tumor and fat layers influence, as expected, the result, as the probe is then averaging (with unknown weights) the dielectric properties of the skin, fat and tumor. Similarly, for the conductivity, the measured value remains approximately the same for both tumor sizes over the entire frequency band. However, when the adjoining skin is measured, the difference is observed between the tumor in the fat under the skin and in the adjoining skin from 10 GHz to 26.5 GHz.

The computed results are also compared with the reference BCC and reference fat values obtained from literature [39,40]. As expected, the measured permittivity and conductivity values are lower than the reference BCC values and higher than the reference fat tissue,



(a)



(b)

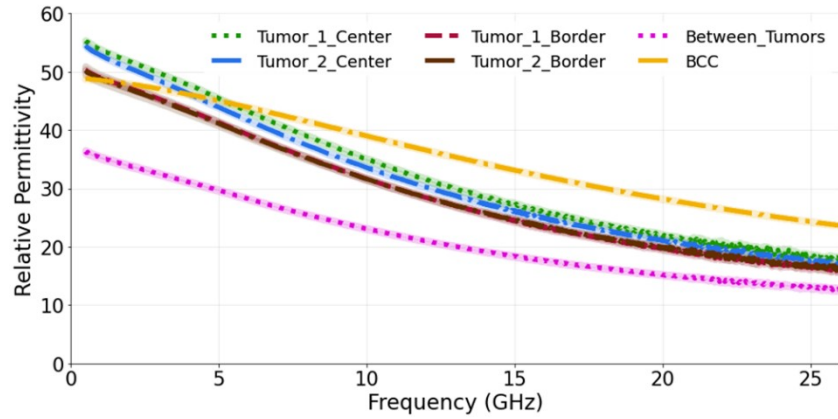
Fig. 5.5: (a) Relative permittivity and (b) conductivity measurements of tumors present in the fat underneath the skin and adjoining skin compared with the reference BCC and fat data from [39,40]. For each phantom model, two tumor sizes are taken: 10 mm and 2 mm.

as the probe perceives a value averaged among the individual components of the complex dielectric distribution.

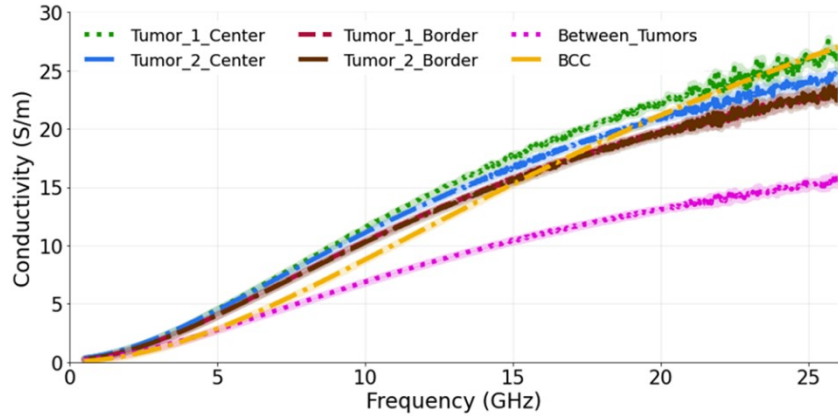
5.2.5 Study 2: Multiple-Lesion Arrangement on the Skin Surface

The aim of second study is to observe how the presence of more than one tumor affects the dielectric measurements. Therefore, in this case more than one tumor (10 mm in diameter) is placed so that its upper surface is coplanar with the surface of the skin. We label them as T1 and T2. The measurements were conducted for three probe locations: at the center, at the border of each tumor and in-between (equidistantly) the two tumors. As is seen from the Fig.5.6 a, b, when the dielectric measurements are performed at the center of each tumor, the relative permittivity and conductivity are higher in comparison to when the measurements are conducted at the border of each tumor. Again, these results are expected, since when measuring at the border, the probe averages the dielectric properties of both skin and tumor, as both of these materials are present within its sensing volume. Similar, but not identical, averaging of properties occurs when the probe is placed between the tumors, thereby sensing yet another heterogeneous dielectric distribution. We observe that the permittivity of tumors, when measured at the center, closely matches the reference BCC value. The percentage difference between T1 measured at the center and the reference BCC is calculated as 14.6% and 32.7% for the permittivity and conductivity, respectively. Similarly, T1, when measured at the border, has the difference of 20.9% and 22.9% with reference BCC for the permittivity and conductivity, respectively. The percentage difference measured in-

between T1 and T2 and the reference BCC is 41.2% and 29.6% for the permittivity and conductivity, respectively.



(a)



(b)

Fig. 5.6: (a) Relative permittivity and (b) conductivity measurements at the center of each tumor, at the border of each tumor and in-between the tumors compared with the reference data from [39]. The diameter of both tumors is 10 mm.

5.2.6 Study 3: Testing Two Skin Phantoms: Oil-Gelatin and Probingon AB

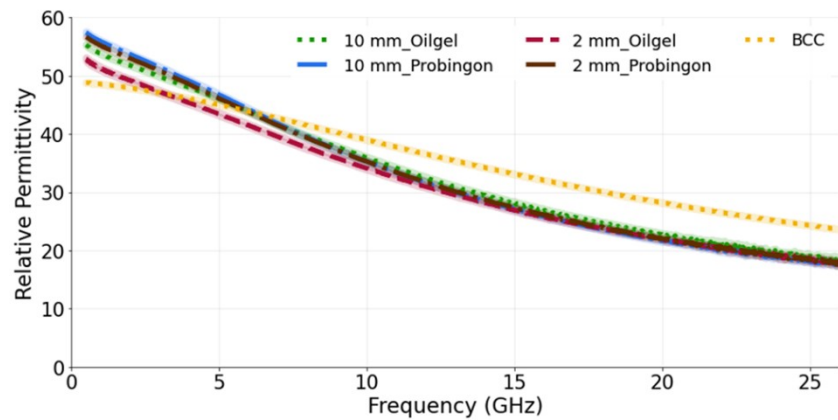
The objective of this study is to identify the detection capability of the probe when the tumor is placed in two different types of skin (oil-gelatin and Probingon AB) at three different locations relative (in alignment with the surface of skin, embedded in the skin and raised out of skin) to the skin. For each case, we have considered tumor sizes of 10 mm and 2 mm in diameter.

Case 1: Tumors Aligned with the Skin Surface

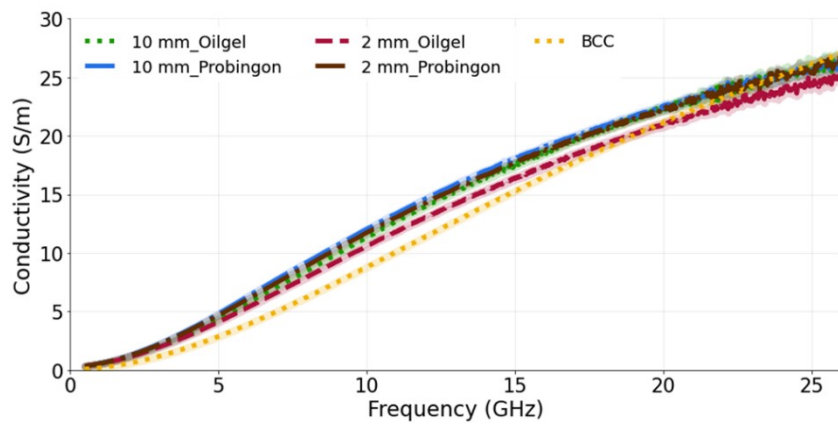
Fig.5.7 a, b shows the relative permittivity and conductivity, respectively, for tumors when placed in alignment with the skin. It can be seen that, for both tumor sizes and their placement in two different types of skin, the dielectric properties are approximately the same. This demonstrates the ability of the probe to identify the tumor (10 mm or 2 mm) regardless of the skin phantom used. While comparing the measured results with the reference BCC dielectric properties, we can see that both models exhibit a similar trend. The computed percentage difference between the 10 mm tumor in alignment with the oil-gelatin skin and the reference BCC is 12.6% and 31.2%; for the 10 mm tumor aligned with the Probingon AB skin model, the values are 15.7% and 37.2% for permittivity and conductivity, respectively.

Case 2: Tumor Embedded within the Skin

In the next case, the tumors (10 mm and 2 mm in diameter) are placed within the oil-gelatin-based and Probingon AB skins. The measured relative permittivity and conductivity are



(a)



(b)

Fig. 5.7: (a) Relative permittivity and (b) conductivity measurements of tumors present in two types of skin: oil-gelatin and Probingon AB. The results are compared with the reference data from [39]. For each case, measurements are performed with two tumor sizes (10 mm and 2 mm in diameter) and the tumor is in alignment with the top surface of the skin.

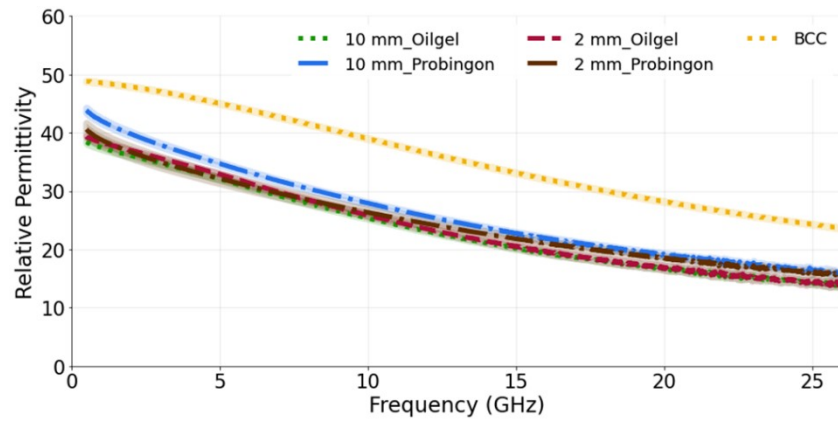
given in Fig.5.8 a, b, both showing values that are lower than the reference BCC tumor values. Clearly, the skin layer surrounding the tumor is sensed by the probe and also contributes to the overall result. The percentage difference for the 10 mm tumor embedded in the oil–gelatin skin, the 10 mm tumor embedded in the Probingon skin and the reference BCC is 35.8% and 26.3%, and 28.2% and 37.0%, in terms of the permittivity and conductivity, respectively.

Case 3: Tumor Raised out of the Skin

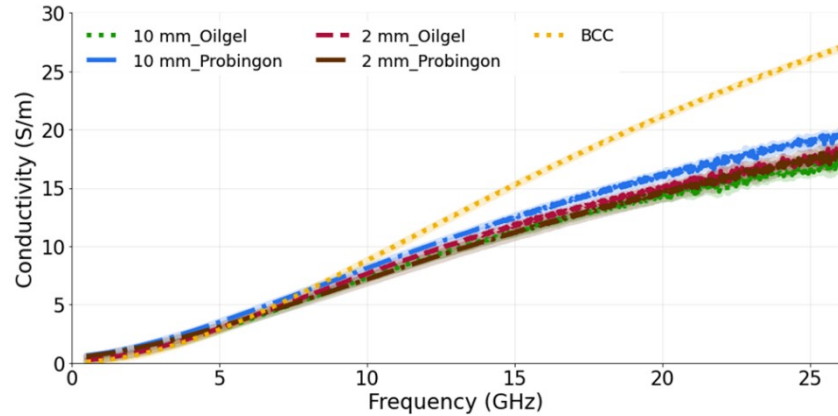
For the last case, the tumor is raised out of skin, again considering two skin phantoms and the 10 mm and 2 mm diameter tumor models. We observe that the 10 mm tumors in both skin models exhibit the same dielectric permittivity and conductivity (as shown in Fig.5.9 a, b). The 10 mm tumor in the Probingon AB and oil–gelatin has perceived higher dielectric properties and are more closely matched to the reference BCC than the 2 mm tumor. In the case of the smaller tumor, the probe’s sensing volume clearly includes more of the skin material. The percentage difference between the 10 mm tumor raised out of the skin models and the reference BCC are 17.8% and 24.1% (oil–gelatin) and 20.9% and 30.7% (Probingon AB) for the permittivity and conductivity, respectively.

5.3 Conclusion

Tissue-mimicking phantoms are needed for the validation and assessment of new diagnostic prototypes in controlled laboratory environments and prior to clinical trials. In this study,

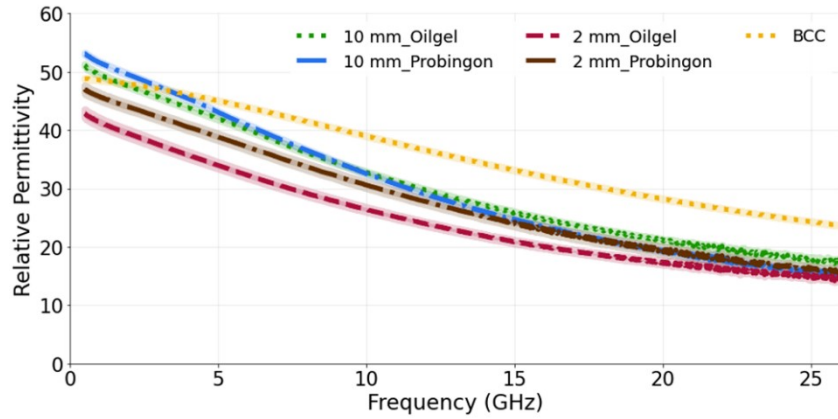


(a)

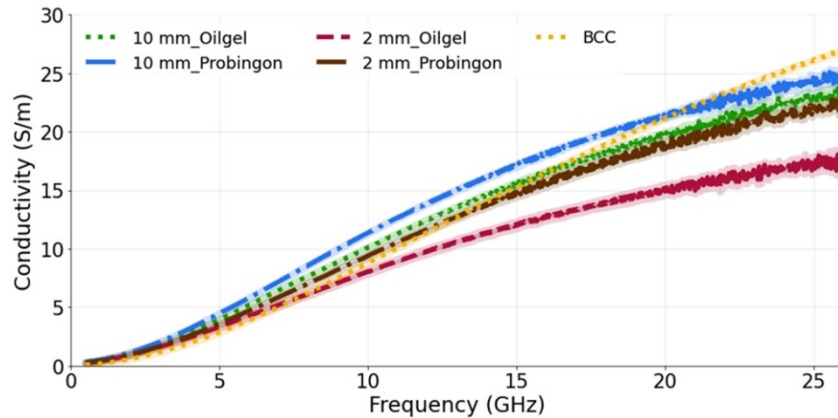


(b)

Fig. 5.8: (a) Relative permittivity and (b) conductivity measurements of tumors present in two types of skin: oil-gelatin and Probingon AB. The results are compared with the reference data from [39]. For each case, measurements are performed with two tumor sizes (10 mm and 2 mm in diameter) and the tumor is embedded within the skin.



(a)



(b)

Fig. 5.9: (a) Relative permittivity and (b) conductivity measurements of tumors present in two types of skin: oil-gelatin and Probingon AB. The results are compared with the reference data from [39]. For each case, measurements are performed with two tumor sizes (10 mm and 2 mm in diameter) and the tumor is raised out of skin.

we developed and examined the dielectric performance of realistic skin tumor phantom models aimed at mimicking these tissues for applications in the microwave frequency range 0.5–26.5 GHz. The phantoms simulated different conditions: liposarcoma condition, where we placed the tumor in the fat underneath the skin, and nonsyndromic multiple basal cell carcinoma condition, where more than one tumor was placed in alignment with the skin surface. Further, we investigated the use of different skin-mimicking materials by placing oil–gelatin-based tumors in two skin models (oil–gelatin and Probingon AB). Each phantom model was tested with two tumor sizes (10 mm and 2 mm in diameter) in order to assess the probe’s ability to identify the tumor, as its size will impact the complex dielectric distribution present in the probe’s sensing volume.

Thus, the goal of our study was to characterize stable heterogeneous phantom models which dielectrically and anatomically represent several skin and tumor geometries. The results have an impact on the meaningful interpretation of the test results for the microwave diagnostic tools aimed to assist the dermatologist in decision-making process. The oil–gelatin phantoms were fabricated with off-the-shelf components and compared to the commercially available Probingon AB skin phantom. The characterization was performed over the 0.5–26.5 GHz range. The resulting phantom model data were compared with the reference excised tissues from the literature, the dispersive properties of which were evaluated using one-pole Cole–Cole parameters. Encouragingly for the microwave-based diagnostic tools under development, our results indicate that, even when

the skin layers surrounding the tumor result in heterogeneous dielectric distribution within the probe's sensing volume, the microwave probe is still able to identify the tumor lesions.

5.4 References

- [1] F. Kazemi, F. Mohanna, J. Ahmadi-Shokouh, "Detection of biological abnormalities using a near-field microwave microscope," *International Journal of Microwave and Wireless Technologies*, vol. 10, no. 8, pp. 933–941, 2018.
- [2] Y. Hayashi, N. Miura, N. Shinyashiki, S. Yagihara, "Free water content and monitoring of healing processes of skin burns studied by microwave dielectric spectroscopy *in vivo*," *Physics in Medicine & Biology*, vol. 50, no. 4, pp. 599-612, 2005.
- [3] S. A. Rezaeieh, A. Zamani, A. M. Abbosh, "3-D wideband antenna for head-imaging system with performance verification in brain tumor detection," *IEEE Antennas and Wireless Propagation Letters*, vol. 14, pp. 910–914, 2014.
- [4] B. L. Oliveira, D. Godinho, M. O'Halloran, M. Glavin, E. Jones, R. C. Conceição, "Diagnosing Breast Cancer with Microwave Technology: Remaining Challenges and Potential Solutions with Machine Learning," *Diagnostics*, vol. 8, no. 2, pp. 36, 2018.
- [5] P. Mehta, K. Chand, D. Narayanswamy, D. G. Beetner, R. Zoughi, W. V. Stoecker, "Microwave reflectometry as a novel diagnostic tool for detection of skin cancers," *IEEE*

- Transactions on Instrumentation and Measurement*, vol. 55, no. 4, pp. 1309–1316, 2006.
- [6] D. O’Loughlin, M. O’Halloran, B. M. Moloney, M. Glavin, E. Jones, M. A. Elahi, “Microwave breast imaging: Clinical advances and remaining challenges,” *IEEE Transactions on Biomedical Engineering*, vol. 65, no. 11, pp. 2580–2590, 2018.
- [7] A. P. O’Rourke, M. Lazebnik, J. M. Bertram, M. C. Converse, S. C. Hagness, J. G. Webster, D. M. Mahvi, “Dielectric properties of human normal, malignant and cirrhotic liver tissue: In vivo and ex vivo measurements from 0.5 to 20 GHz using a precision open-ended coaxial probe,” *Physics in Medicine & Biology*, vol. 52, no. 15, pp. 4707–4719, 2007.
- [8] S. R. M. Shah, N. B. Asan, J. Velandar, J. Ebrahimizadeh, M. D. Perez, V. Mattsson, T. Blokhuis, R. Augustine, “Analysis of thickness variation in biological tissues using microwave sensors for health monitoring applications,” *IEEE Access*, vol. 7, pp. 156033–156043, 2019.
- [9] A. Moradpour, O. Karadima, I. Alic, M. Ragulskis, F. Kienberger, P. Kosmas, “Development of a Solid and Flexible Matching Medium for Microwave Medical Diagnostic Systems,” *Diagnostics*, vol. 11, no. 3, pp. 550, 2021.
- [10] C. Dachena, A. Fedeli, A. Fanti, M. B. Lodi, M. Pastorino, A. Randazzo, “Microwave Imaging for the Diagnosis of Cervical Diseases: A Feasibility Analysis,” *IEEE Journal*

- of Electromagnetics, RF and Microwaves in Medicine and Biology*, vol. 5, no. 3, pp. 277–285, 2020.
- [11] I. Iliopoulos, S. D. Meo, M. Pasian, M. Zhadobov, P. Pouliguen, P. Potier, L. Perregrini, R. Sauleau, M. Ettorre, “Enhancement of penetration of millimeter waves by field focusing applied to breast cancer detection,” *IEEE Transactions on Biomedical Engineering*, vol. 68, no. 3, pp. 959–966, 2020.
- [12] N. Joachimowicz, B. Duchêne, C. Conessa, O. Meyer, “Anthropomorphic breast and head phantoms for microwave imaging,” *Diagnostics*, vol. 8, no. 4, pp. 85, 2018.
- [13] J. B. Wilson, “Excisional Biopsy of Dermal and Subcutaneous Lesions,” *In Illustrative Handbook of General Surgery*, Springer: Berlin/Heidelberg, Germany, pp. 781–791, 2016.
- [14] S. Castelló-Palacios, C. Garcia-Pardo, A. Fornes-Leal, N. Cardona, A. Vallés-Lluch, “Tailor-made tissue phantoms based on acetonitrile solutions for microwave applications up to 18 GHz,” *IEEE Transactions on Microwave Theory and Techniques*, vol. 64, no. 11, pp. 3987–3994, 2016.
- [15] S. Romeo, L. D. Donato, O. M. Bucci, I. Catapano, L. Crocco, M. R. Scarfi, R. Massa, “Dielectric characterization study of liquid-based materials for mimicking breast tissues,” *Microwave and Optical Technology Letters*, vol. 53, no. 6, pp. 1276–1280, 2011.

- [16] F. Topfer, J. Oberhammer, “Millimeter-wave tissue diagnosis: The most promising fields for medical applications,” *IEEE Microwave Magazine*, vol. 16, no. 14, pp. 97–113, 2015.
- [17] J. Garrett, E. Fear, “A new breast phantom with a durable skin layer for microwave breast imaging,” *IEEE Transactions on Antennas and Propagation*, vol. 63, no. 4, pp. 1693–1700, 2015.
- [18] J. Garrett, E. Fear, “Stable and flexible materials to mimic the dielectric properties of human soft tissues,” *IEEE Antennas and Wireless Propagation Letters*, vol. 13, pp. 599–602, 2014.
- [19] A. T. Mobashsher, A. M. Abbosh, “Artificial human phantoms: Human proxy in testing microwave apparatuses that have electromagnetic interaction with the human body,” *IEEE Microwave Magazine*, vol. 16, no. 6, pp. 42–62, 2015.
- [20] L. Joseph, N. B. Asan, J. Ebrahimizadeh, A. S. Chezhan, M. D. Perez, T. Voigt, R. Augustine, “Non-invasive transmission based tumor detection using anthropomorphic breast phantom at 2.45 GHz,” *In Proceedings of the 2020 14th European Conference on Antennas and Propagation (EuCAP)*, Copenhagen, Denmark, 15–20 March 2020, pp. 1–5.
- [21] Probingon, A.B. Patient Centered Diagnostics, Accessed: Dec. 25, 2021. [Online]. Available: <http://www.probingon.com/>.

- [22] B. Amin, A. Shahzad, D. Kelly, M. O'Halloran, M. A. Elahi, "Anthropomorphic calcaneus phantom for microwave bone imaging applications," *IEEE Journal of Electromagnetics, RF and Microwaves in Medicine and Biology*, vol. 5, no. 3, pp. 206–213, 2020.
- [23] J. Boparai, M. Popović, "Development and Characterization of Skin Phantoms at Microwave Frequencies," *IEEE Journal of Electromagnetics, RF and Microwaves in Medicine and Biology* in press, 2022.
- [24] Liposarcoma-NORD (National Organization for Rare Disorders), Accessed: Dec. 25, 2021. [Online]. Available: <https://rarediseases.org/rare-diseases/liposarcoma/>.
- [25] D. H. Kim, H. S. Ko, Y. J. Jun, "Nonsyndromic multiple basal cell carcinomas," *Archives of Craniofacial Surgery*, vol. 18, no. 3, pp. 191-196, 2017.
- [26] Liposarcoma-Symptoms and Causes-Mayo Clinic, Accessed: Dec. 25, 2021. [Online]. Available: <https://www.mayoclinic.org/diseases-conditions/liposarcoma/symptoms-causes/syc-20352632>.
- [27] V. Bartos, "Development of multiple-lesion basal cell carcinoma of the skin: A comprehensive review," *Şişli Etfal Hastanesi tıp Bülteni*, vol. 53, no. 4, pp. 323-328, 2019.
- [28] M. Lazebnik, E. L. Madsen, G. R. Frank, S. C. Hagness, "Tissue-mimicking phantom

- materials for narrowband and ultrawideband microwave applications,” *Physics in Medicine & Biology*, vol. 50, no. 18, pp. 4245-4258, 2005.
- [29] O. Akkus, A. Oguz, M. Uzunlulu, M. Kizilgul, “Evaluation of skin and subcutaneous adipose tissue thickness for optimal insulin injection,” *Journal of Diabetes and Metabolism*, vol. 3, no. 8, pp. 1000216, 2012.
- [30] P. Oltulu, B. Ince, N. Kokbudak, S. Findik, F. Kilinc, “Measurement of epidermis, dermis, and total skin thicknesses from six different body regions with a new ethical histometric technique,” *Turkish Journal of Plastic Surgery*, vol. 26, no. 2, pp. 56-61, 2018.
- [31] E. Porter, J. Fakhoury, R. Oprisor, M. Coates, Popović, “Improved tissue phantoms for experimental validation of microwave breast cancer detection,” *In Proceedings of the Fourth European Conference on Antennas and Propagation*, Barcelona, Spain, 12–16 April 2010, pp. 1–5.
- [32] L. Joseph, M. D. Perez, R. Augustine, “Development of Ultra-Wideband 500 MHz–20 GHz Human Skin Phantoms for Various Microwaves Based Biomedical Applications,” *In Proceedings of the 2018 IEEE Conference on Antenna Measurements & Applications (CAMA)*, Västerås, Sweden, 3–6 September 2018, pp. 1–3.
- [33] Keysight Technologies Inc. N1501A Dielectric Probe Kit, Accessed: Dec. 25, 2021. [Online]. Available: <http://www.keysight.com/en/pd-2492144-pn-N1501A/dielectric->

probe-kit?cc=US&1c=eng.

- [34] Keysight Technologies Inc. N9918A FieldFox Handheld Microwave Analyzer, 26.5 GHz, Accessed: Dec. 25, 2021. [Online].

Available: <https://www.keysight.com/ca/en/product/N9918A/fieldfox-a-handheld-microwave-analyzer-26-5-ghz.html>.

- [35] B. N. Taylor, C. E. Kuyatt, “Guidelines for Evaluating and Expressing the Uncertainty of NIST Measurement Results,” US Department of Commerce, Technology Administration, National Institute of Standards and Technology: Gaithersburg, MD, USA, 1994.

- [36] A. L. Gioia, S. Salahuddin, M. O’Halloran, E. Porter, “Quantification of the sensing radius of a coaxial probe for accurate interpretation of heterogeneous tissue dielectric data,” *IEEE Journal of Electromagnetics, RF and Microwaves in Medicine and Biology*, vol. 2, no. 3, pp. 145–153, 2018.

- [37] N. Piladaeng, N. Angkawisittpan, S. Homwuttiwong, “Determination of relationship between dielectric properties, compressive strength, and age of concrete with rice husk ash using planar coaxial probe,” *Measurement Science Review*, vol. 16, no. 1, pp. 14–20, 2017.

- [38] E. Porter, A. L. Gioia, S. Salahuddin, S. Decker, A. Shahzad, M. A. Elahi, M. O’Halloran, O. Beyan, “Minimum information for dielectric measurements of

- biological tissues (MINDER): A framework for repeatable and reusable data,” *International Journal of RF and Microwave Computer-Aided Engineering*, vol. 28, pp. 21201, 2018.
- [39] A. Mirbeik-Sabzevari, R. Ashinoff, N. Tavassolian, “Ultra-wideband millimeter-wave dielectric characteristics of freshly excised normal and malignant human skin tissues,” *IEEE Transactions on Biomedical Engineering*, vol. 65, no. 6, pp. 1320–1329, 2017.
- [40] M. Lazebnik, D. Popović, L. McCartney, C. B. Watkins, M. J. Lindstrom, J. Harter, S. Sewall, T. Ogilvie, A. Magliocco, T. M. Breslin, “A large-scale study of the ultrawideband microwave dielectric properties of normal, benign and malignant breast tissues obtained from cancer surgeries,” *Physics in Medicine & Biology*, vol. 52, pp. 6093-6115, 2007.

Chapter 6

Numerical and Experimental Models of Melanoma Growth for Assessment of Microwave-Based Diagnostic Tool

This chapter is based on the following publication:

J. Boparai, R. Tchinov, O. Miller, Y. Jallouli and M. Popović, “Numerical and Experimental Models of Melanoma Growth for Assessment of Microwave-Based Diagnostic Tool,” in submission to the *IEEE Transactions on Biomedical Engineering*.

Preface to Chapter 6: Melanoma, considered to be the most fatal form of skin cancer, is identified with radial and vertical growth phases. The most common method to identify a malignant tumor is the visual inspection by physicians following the ABCDE rule, which is not sufficient when there is a case of a tumor with varying thickness.

Thus, the purpose of our study was to assess feasibility of a microwave-based diagnosis of melanoma tumor with varying thickness and radial growth. Therefore, we developed a

tumor progression model representing quantitatively radial and vertical growth of malignant melanoma over the course of time. Based on this model, we then realized oil-in-gelatin semi-solid phantoms representing growth patterns of melanoma.

These fabricated phantoms were characterized using slim-form open-ended coaxial probe in two experiments. The first involved dielectric measurements of a suspicious lesion by moving the dielectric probe over the tumor, also covering the adjoining healthy skin, along a linear segment. In the second experiment, a suspicious lesion was scanned along a grid and a dielectric map was generated to obtain different levels of permittivity and conductivity across the modeled suspicious lesion.

Results indicate the potential ability of the probe to identify variation in dielectric properties with variation in both thickness and diameter of the tumor. The results were also validated with estimated values of dielectric properties of malignant melanoma using Lichtenecker's equation obtained from the literature. It was observed that the measured results follow the same trend as the reference values.

Abstract—Melanoma is the fastest growing cancer worldwide, which has the tendency to metastasize, leading to high mortality rates. Malignant melanoma tumor progression is exhibited by radial and vertical growth phases. The purpose of this study is to provide a feasibility assessment of microwave-based diagnosis of melanoma at different stages of tumor progression. To accomplish this, we developed a model of melanoma primary tumor

progression on the basis of radial and vertical growth patterns of melanoma. Thereafter, oil-in-gelatin experimental phantoms are fabricated. The developed phantoms are evaluated for dielectric properties using a slim-form open-ended coaxial probe by performing a series of measurements across the suspicious region over the frequency range of 0.5 – 26.5 GHz. Furthermore, a dielectric map is generated illustrating different levels of permittivity and conductivity across the suspicious lesion. The obtained results indicate that the system can sense the variation in dielectric properties, with variation of both thickness and radial diameter of tumor. The computed results are compared with the estimated dielectric values of malignant melanoma using Lichtenecker’s mixing equation obtained from the literature.

Index Terms—cancer, conductivity, dielectric properties, melanoma, microwave frequencies, permittivity, skin cancer, tumors

6.1 Introduction

Malignant melanoma, the most life-threatening and aggressive form of skin cancer accounts for merely 1% of all skin cancer cases but is the leading cause of skin cancer deaths [1]. According to the American cancer society, it is estimated that 99,780 new cases of invasive and 97,920 in-situ melanoma cases will be diagnosed in the United States in 2022, and about 7,650 deaths will happen due to this disease [2]. Melanoma starts in body’s pigment cells, known as melanocytes [3-4]. Two growth phases termed as radial and vertical growth phases are commonly observed in the malignant melanoma [5]. In the radial growth phase, malignant

cells grow radially and then begin the vertical growth phase, in which the malignant cells start invading the deeper layers and risk metastasizing [6]. These growth phases are usually described by sequential stages of tumor progression that tell how deep the tumor has grown into the skin and how far it has spread in the radial direction [5]. In the early stage, melanoma cells are confined to the epidermis. This is called stage 0 or melanoma in-situ (MIS). In stages 1 and 2, melanoma cells grow into the layer directly under the epidermis, known as the dermis. At this stage, the malignant cells have not yet spread to the lymph nodes or distant body organs. In the advanced stages 3 and 4, cancer cells reach the lymphatic and blood vessels and can spread and metastasize [6]. According to the study [7], when a cancerous tumor advances in stage and becomes invasive, it will grow faster in depth than radially. Furthermore, melanoma tends to have a reduction in the diameter as they grow deeper into the skin. The phenomenon of tumor progression demonstrating various stages of growth is illustrated in Fig 6.1.

Diagnosis of most melanomas begins with visual inspection of a suspicious looking mole in the skin. The criterion followed by clinicians is to differentiate common moles from melanomas following the ABCDE rule where A describes asymmetry (non uniformity of the shape); B is related to the irregularity of the border (outer edges of mole are notched, blurred or ragged); C is for color variation (mole having shades of tan, brown or black); D is for diameter (if it is ≥ 6 millimeters); and E describes evolution, which means a change in appearance of mole over time [2]. Sometimes, to augment the efficacy of detection of

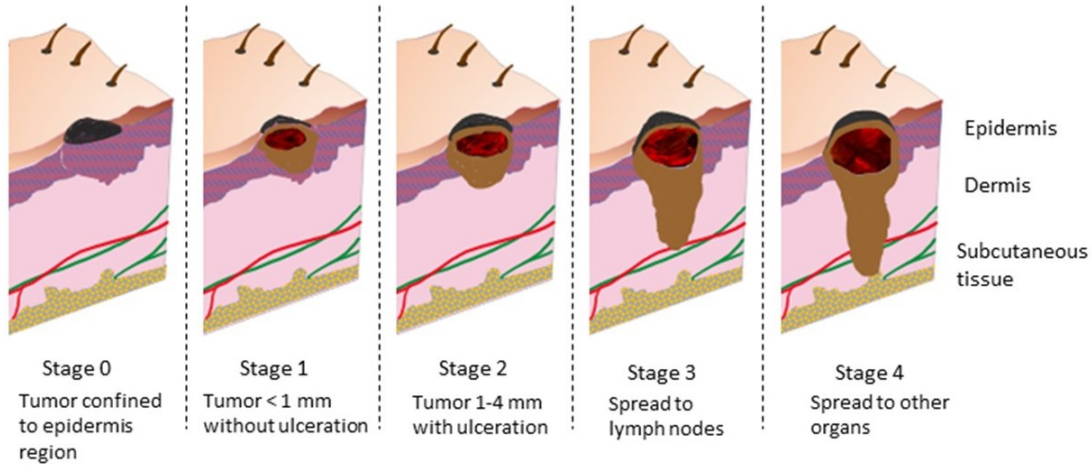


Fig. 6.1: Schematic of stages of melanoma progression with respect to radial and vertical growth.

melanoma, computerized approaches such as acquisition of images using specific magnification devices have been utilized [8-10]. However, for this, there is a requirement of trained and experienced primary care physician [1,11-12]. Tumor thickness (vertical growth of tumor) is an important prognostic factor, that must be taken into consideration while diagnosing malignant melanoma [12-13]. Therefore, although crucial, visual assessment based on the above-mentioned clinical criteria is not sufficient when it comes to the diagnosis of tumors with varying thickness. It will eventually require a full thickness biopsy for adequate pathologic interpretation which is usually performed by examining the tissue under a microscope [3,14]. This process can lead to an increase in the overall cost and delay in treatment [15]. Standard modalities used in diagnosis of skin cancer are X-rays and CT scans, which are associated with radiation exposure, while other modalities, which

are considered to be the gold standard, such as Magnetic Resonance Imaging (MRI), are expensive [16].

Thus, it is imperative to develop a non-invasive, non-ionizing, portable and cost-effective technique which can help dermatologists identify malignant melanoma tumors with varying thickness along with identifying the radial growth features. Such a technique could reduce examination time and lower the number of required biopsies. A promising approach lies in the microwave reflection-based diagnosis methods which utilize dielectric properties, permittivity and conductivity, to discriminate between malignant and benign lesions [17-18]. Microwave-based detection is widely explored in the field of biology and medical applications [19-21]. Malignant tumorous tissues have higher water content, leading to the dielectric contrast between them and the surrounding healthy tissues [22-23].

The development and performance evaluation of any medical diagnostic system require physical structures that accurately imitate electrical and mechanical properties of biological tissues, commonly known as phantoms. To the best of our knowledge, previous studies on skin cancer tumor phantoms for difference in dielectric property-based detection have only considered tumors of uniform thickness. The work of Giulia *et al.* [24] reported melanoma detection in the 39.5-41 GHz range. This paper presents a method of tumor imaging using a CNC machine to create a grid of measurements completely covering the affected area, as well as some of the surrounding healthy tissue phantom. However, the tumor phantom implanted in the skin phantom had a uniform thickness. In a more recent study [25], two canonical-

spherical tumors with diameters of $400 \mu m$ are inserted within skin phantoms. Although having a uniform thickness is important for initial testing, experiments which have also been conducted previously by our laboratory [26-27], melanoma anatomy is of varying thickness.

Thus, the purpose of our study is to assess the effectiveness of microwave-based techniques to identify tumors with non-uniform thickness at any stage of tumor progression, which can help physicians and nurses diagnose melanoma in a clinical setting with high sensitivity. With this aim, we first developed a model of melanoma primary tumor progression based on radial and vertical growth patterns. Then, we fabricated oil-in-gelatin semi-solid phantoms. Finally, we performed dielectric measurements over the fabricated phantoms using a slim-form open-ended coaxial dielectric probe over the frequency range of 0.5 to 26.5 GHz. The results were then compared with effective complex permittivity obtained using Lichteneker's mixing equation from the literature. The model is selected for validation, since there are no reported measured dielectric values available for malignant melanoma.

6.2 Materials and Methods

This section presents the design of tumor progression model that provides quantitatively the radial and vertical growth of malignant melanoma over course of time, calculated with the help of mathematical functions in MATLAB. Then, following this progression model, tissue mimicking phantoms representing growth patterns of melanoma tumor at different stages are constructed. Finally, the dielectric properties of the fabricated phantoms are evaluated

by performing measurements across the suspicious region.

6.2.1 Tumor Progression Model

Melanoma's growth pattern is split up into 3 phases: in-situ, invasive and metastatic. The melanoma in-situ (MIS) phase refers to stage 0 tumors, for which the vertical growth rate is negligible, and is approximated to 0 mm/month [7,29]. MIS is a tumor that is confined in the epidermal layer and is not yet invasive. Second, a melanoma tumor becomes invasive once cancerous cells grow beyond the epidermis and can spread freely [30]. Finally, once the tumor reaches the lymphatic system, the tumor has metastasized.

Taking the above physiological properties of melanoma, we model the growth pattern of melanoma. To prioritize the worst-case scenario of MIS, we choose to create the MIS phantom with the thickness of the epidermis. The MIS tumor is a disc of average epidermal thickness. This is illustrated in Fig. 6.2.

Beyond stage 0 melanoma, the tumor becomes invasive and begins to grow in depth in addition to horizontal expansion. As seen in Fig. 6.1 (stages of malignant melanoma progression), the tumor prioritizes vertical, over horizontal growth. This behavior is expected, as the most rapid way for the tumor to metastasize, is to grow in depth to the lymphatic system [31]. Therefore, the invasive tumor (stage 1 and beyond) is designed as a growing cone, with the base being at the surface of the skin, as shown in Fig. 6.3.

The radial growth of the tumor is uniform and is reported to be on average $5.3 \text{ mm}^2/\text{year}$

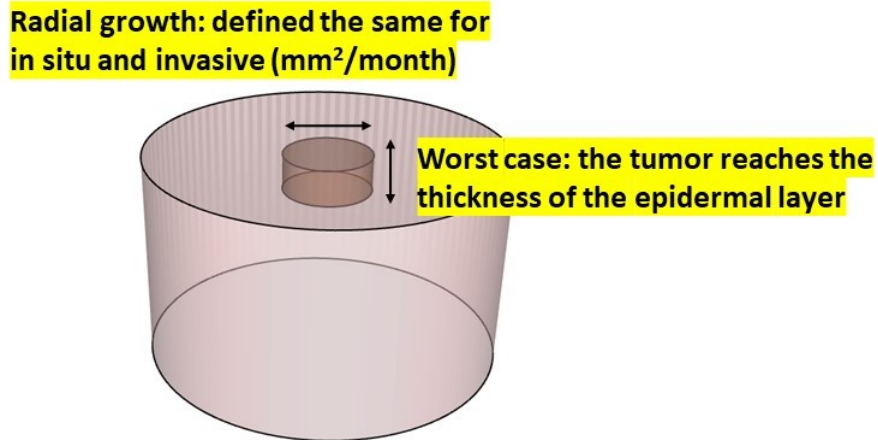


Fig. 6.2: Model for the MIS tumor phantom.

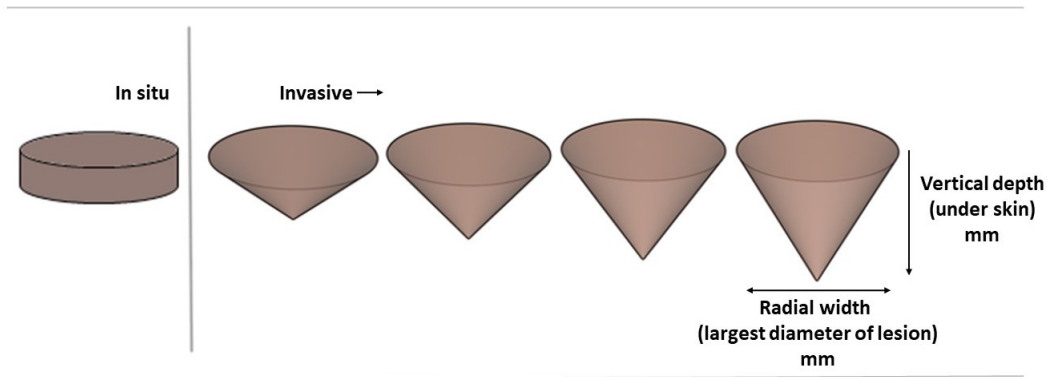


Fig. 6.3: General model for melanoma tumor progression.

[29]. As such, for this circular cross-section model, the monthly increase of the cross-sectional area of the tumor at the skin surface is $5.3/12 = 0.4417 \text{ mm}^2$. Next, the approximation that the tumor cross-sectional area at the skin surface grows uniformly [32] yields the following growth pattern (Eq. 6.1) for the radius of the skin surface cross-section of the tumor. r_k is radius of the tumor at the surface of the skin for month k .

$$\begin{aligned} \pi(r_{k+1}^2 - r_k^2) &= 0.4417 \text{ mm}^2/\text{month} \\ r_{k+1} &= \sqrt{\frac{0.4417 \text{ mm}^2}{\pi} + r_k^2}; \quad k \in \{0, 1, \dots\} \end{aligned} \tag{6.1}$$

The vertical rate of growth (ROG) for the cone model, describing the varying depth of the tumor, is found by averaging the weighted median vertical ROG based on the frequency of melanoma type from two studies [7, 33]. The vertical ROG for our model is 0.18625 mm/month.

Next, the boundary points of the growth model are defined as the initial tumor size at transition from MIS to invasive melanoma, and metastatic tumor size. The transition point from MIS to invasive melanoma is approximated to be a 6 mm diameter tumor. It has been concluded that the odds of a tumor of diameter less than 6 mm metastasizing and spreading is very low. Observing cases of MIS and invasive tumors above 6 mm in diameter, is considered as a routine diagnostic method [34].

The starting diameter of the phantom simulation is 6 mm. MIS tumors may stay “in-situ” for several years before becoming invasive. Additionally, there is no quantitative diameter of a tumor that will induce the invasive nature of a melanoma. This transition depends on mutations that are generally due to individual genetic makeup. Therefore, we have chosen to begin the tumor phantom simulation at a radial diameter of 6 mm on the surface of the skin [35, 36].

The end of the tumor growth phantom simulation is marked by a tumor depth of 4 mm.

Once the melanoma reaches the lymphatic vessel it will drain into a regional lymph node [31]. In stage 4, the cancer has spread to other organs and, since it has reached the lymphatic and blood vessels, it does not grow in depth as quickly. Therefore, we can assume that the maximal depth of the primary tumor would be 4 mm [37].

From the above-stated assumptions, the parameters for the tumor progression model are presented in Table 6.1. These parameters are used to generate appropriate tumor measurements for months 0 to 22 at 2-month intervals, as presented in Table 6.2. Fig. 6.4 illustrates generated tumor models using the measurements of Table 6.2 in MATLAB.

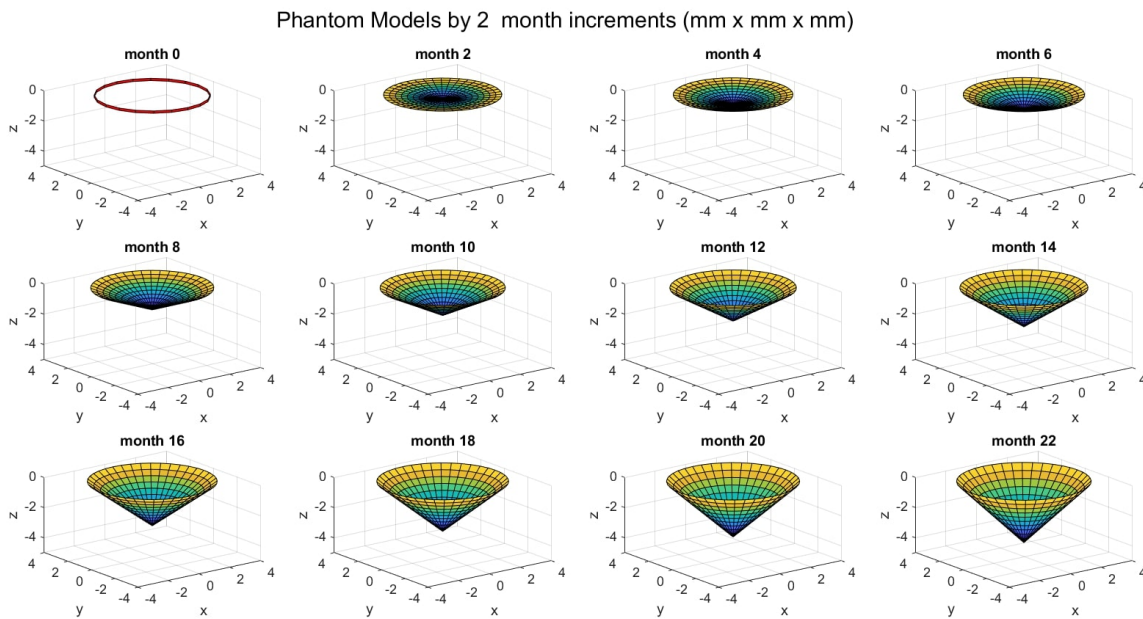


Fig. 6.4: MATLAB-generated progression plots of tumor with bimonthly radial and vertical growth.

Table 6.1: Tumor progression: biological and physiological parameters

Parameter	Explanation	Value	Units
Radial ROG	radial monthly rate of growth (cross-sectional area)	0.44	mm ² /month
Vertical ROG	vertical monthly rate of growth (for invasive tumors)	0.19	mm/month
Initial diameter of tumor	starting diameter of circular cross-section of tumor at the surface of skin	6	mm
Initial depth of tumor	Starting depth/thickness of tumor	0.15	mm
Boundary diameter invasive	Diameter of circular cross-section of tumor at the surface of skin that causes tumor to become invasive	6	mm
Boundary thickness	depth/thickness of tumor that causes tumor to become invasive	0.15	mm
Max depth	depth/thickness of tumor that will terminate the simulation (the cancer cells have reached lymphatic/circulatory system)	4	mm

Table 6.2: MATLAB generated theoretical set of bimonthly tumor phantoms

Month	Shape	Diameter (mm)	Depth (mm)
0	Cylinder	6	0.15
2	Cone	6.09	0.34
4	Cone	6.19	0.71
6	Cone	6.28	1.08
8	Cone	6.36	1.46
10	Cone	6.45	1.83
12	Cone	6.54	2.20
14	Cone	6.62	2.57
16	Cone	6.71	2.95
18	Cone	6.79	3.32
20	Cone	6.87	3.69
22	Cone	6.96	4.06

6.2.2 Phantom Design and Development

Based on the tumor progression model developed in our study, we constructed anatomically and dielectrically realistic phantom models consisting of skin layer with tumor insertions of varying diameters and thicknesses, depicting radial and vertical growth of melanoma. Phantoms emulating actual dielectric properties and anatomy of tissues of interest are extensively required for development and assessment of microwave-based skin cancer detection modalities in a controlled environment. A comprehensive review of tissue-emulating phantoms based on different recipes, formulations, textures (i.e. liquid, semi-solid and solid) at diverse frequencies is reported in [38]. Development of physical phantoms by means of 3D printing is also of great interest today but finding materials precisely mimicking dielectric properties of various biological tissues or organs is the

limitation of this technique [39].

For our present study, we have chosen oil-in-gelatin semi-solid materials to realize both skin and tumor insertions, since these materials can be easily tailored to mimic the electrical and physical properties of various biological tissues.

The composition for preparing phantoms was adopted from [40] with the aim to realize both skin layer and tumor insertions and the procedure was followed from [41], summarized here for completeness. Since the epidermis and dermis layer have similar water content [42], we modeled skin as a single layer, combining epidermis and dermis. First, the skin-mimicking material was fabricated by mixing 0.294 g of p-toluic acid (powder) (Sigma-Aldrich, Oakville, Canada) with 28.69 ml of n-propanol (Sigma-Aldrich, Oakville, Canada) and the solution was heated while stirring. The mixture was then added to 279.5 ml of deionized water and 50.02 g (dry mass) of 200 Bloom gelatin at room temperature (Sigma-Aldrich, Oakville, Canada). The resultant mixture was then heated with a double boiler to 90°C, at which point it should become transparent. The mixture was cooled to 50°C before adding 98.6 ml of oil. Stirring vigorously, we then added 5.86 ml of liquid surfactant (Ultra Ivory, Procter and Gamble (P&G), Canada) to form an emulsion, which is then cooled to 40°C. Finally, 3.33 g of formaldehyde was added, and the mixture was cooled to 34°C, before pouring it into container molds with thickness of 15 mm. It is observed in our previous study that underlying skin thickness has not much impact on variation of dielectric properties [26]. The resultant mixture was kept for 24 hours at room temperature in an airtight container for

solidifying.

Carefully designed molds were implanted in the solutions during curing to create perforations for replicating tumor growth in the skin. After the skin phantom solidifies, the mold was removed, and the tumor-equivalent material was poured into the hollow space. The tumor-mimicking tissue is produced similarly, following identical procedural steps, but with the following composition: 0.346 g of p-toluic acid, 17 ml of n-propanol, 328 ml of deionized water. To this 58.67 g of 200 Bloom gelatin, 38.4 ml of oil, 2 ml of surfactant and 3.72 g of formaldehyde were added following the steps outlined above. The tumors representing growth are conical in shape. To realize disk-shaped tumor for month 0, the 6 mm diameter metal ring mold was placed on the top of a uniform skin layer. We fabricated six phantoms representing tumor radial and vertical growth in months 0, 6, 8, 12, 16, 22 and the final dimensions of these fabricated skin phantoms with tumor insertions are given in Table 6.3. Fig. 6.5 (a) shows the skin phantom with tumor inclusion realized in month 12 with diameter, $D = 6.5$ and thickness, $t = 2.2$ mm and Fig. 6.5 (b) illustrates the probe being placed at the skin adjoining to the tumor.

6.2.3 Measurement Set-up

The experimental set-up used in our study for measurement of dielectric properties of fabricated phantoms is comprised of Keysight slim-form open-ended coaxial probe (N1501A) [43] and Keysight FieldFox microwave analyzer (N9918A) [44], connected using a

Table 6.3: Dimensions of the proposed melanoma tumor phantoms

Month	Shape	Diameter, D (mm)	Thickness, t (mm)
0	Cylinder	6	0.1
6	Cone	6.2	1.0
8	Cone	6.4	1.5
12	Cone	6.5	2.2
16	Cone	6.8	2.8
22	Cone	7	4

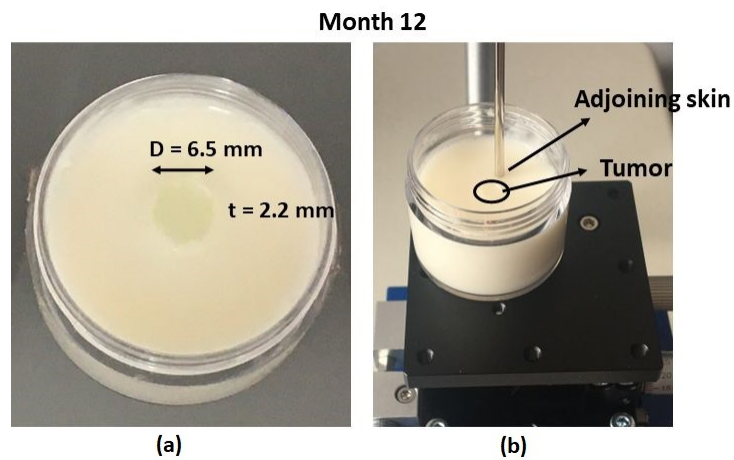


Fig. 6.5: (a) Fabricated skin phantom with tumor inclusion of diameter, $D = 6.5$ mm and thickness, $t = 2.2$ mm (b) Slim-form probe placed at the adjoining skin of tumor.

coaxial cable (N1501A-202). The schematic diagram is shown in Fig. 6.6 and in the inset of the picture is shown the fabricated phantom model placed on the combination of XYZ-stage and vertical lift jack which precisely controls the movement of the sample. The open-ended coaxial probe method is the most widely adapted technique for dielectric properties measurements due to its non-destructive approach, minimum sample handling requirements and broadband measurement capabilities [45]. The slim form probe is

selected for our observations as it allows to be used with smaller sample sizes and semi-solid materials. The reflection coefficients, acquired using vector network analyzer, are then automatically converted to real ϵ_r' and imaginary ϵ_r'' parts of the complex relative permittivity ϵ_r^* over the complete frequency range of 0.5 – 26.5 GHz, with the help of Keysight Materials Measurement suite (N1500A). The power level was set at -10 dBm to reduce thermal effects and for safe measurements. The IFBW (Intermediate frequency bandwidth) was selected to be 100 Hz for greater accuracy and to acquire greater resolution and the dielectric properties were measured over 1001 linear frequency points. The probe is placed on the surface of the sample with moderate pressure to establish firm contact, as high or low pressure may have adverse effects on the dielectric property measurements.

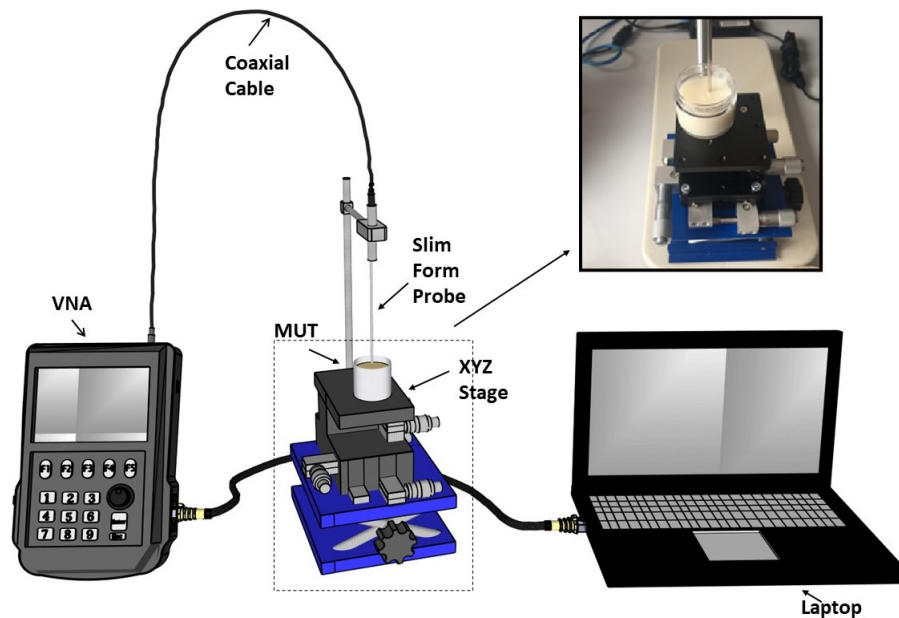


Fig. 6.6: Schematic representation of measurement setup with inset of pictorial view of actual sample under test lying on manually adjustable XYZ-stage.

Before carrying out sample measurements, the system was calibrated using standard three load procedure with Keysight software. Air-short-load technique was utilized for calibration where first, the probe was left open, then short (Keysight metal block) was connected to the probe and lastly probe was immersed into the deionized water (load) at known temperature. Additionally, the validation was performed before and after measuring each sample under test. This is accomplished by measuring dielectric properties of reference materials such as air and deionized water. The accuracy of the system was established by comparing the measured values of deionized water with the literature data which is computed as 1.07% and 0.74% for dielectric constant and conductivity, respectively. On observing any deflections in dielectric properties of validation materials, the calibration and validation were repeated to maintain the accuracy of the system. All dielectric measurements were performed at room temperature and temperature of measurement sample and validation material was monitored with the help of digital thermometer (Thermopro) and temperature remained in the range of 22–23°C). The errors due to accumulation of oil and water at the probe interface during measurements, is usually avoided by cleaning the probe surface with isopropyl and lint free wipes after every measurement. The drift errors due to movement of cables and equipment is also minimized using adjustable XYZ-stage and lift jack for movement of samples.

6.3 Experimental Results and Discussion

This section reports the response of electromagnetic fields in terms of dielectric properties such as relative permittivity and conductivity on characterizing fabricated phantom models depicting tumor growth in the 0.5 – 26.5 GHz frequency band. These dielectric properties were obtained from measured frequency dependent relative complex permittivity, ϵ_r^* , expressed by the formula:

$$\epsilon_r^* = \epsilon_r' - j\epsilon_r'' \quad (6.2)$$

where real part ϵ_r' denotes relative permittivity, also know as dielectric constant describes the ability of material to store energy on application of electric field and the imaginary part ϵ_r'' describes electromagnetic losses in the material due to dissipation of electrical energy [46]. These dielectric losses can be used to deduce electrical conductivity σ with the following formula:

$$\sigma = 2\pi f\epsilon_r''\epsilon_0 \quad (6.3)$$

where $\epsilon_0 = 8.854 \times 10^{-12}$ F/m is the permittivity of free space.

To estimate dielectric properties, we performed two different experiments. In the first experiment, we observed variability in the dielectric properties by moving the probe over the suspicious lesion and adjoining skin on the left and right side of tumor, along the linear segment. In the second experiment, suspicious lesion is characterized in a grid format and

dielectric maps were obtained to observe the response. The reflection coefficients were observed for the tumor region with respect to the adjoining healthy skin.

6.3.1 Tumor profile across a linear segment

The dielectric profile of the tumor region was scanned along the linear segment using the probe as illustrated in the Fig. 6.7. The material to be tested was kept on a manually adjustable XYZ-stage and the probe tip touches the surface of the test sample with even pressure (Fig. 6.5 (b)). The complex reflection coefficients were acquired by moving the XYZ-stage horizontally in the y-direction, so that the probe tip moves along the line over the tumor, with step size of 2 mm. To avoid any damage due to puncturing of probe into the sample, each time the platform was lowered and moved in the y-direction, before placing the probe on next location. The measurements were performed over the five specific locations (Fig. 6.7), starting from the adjoining normal skin (labelled as Left) towards the Right. The measurements were then repeated for tumors presenting radial and vertical growth in months 0, 6, 8, 12, 16 and 22.

Fig. 6.8 (a)–(l) shows the results of the measured relative permittivity and conductivity (at selected five locations) of test samples for each month (0, 6, 8, 12, 16 and 22). As can be observed from the graphs, with progression of time, the tumor grows radially and vertically and the probe is able to sense the dielectric variation. This variation in dielectric properties is anticipated. Considering the locations “Left” and “Right”, which is mostly the skin, the

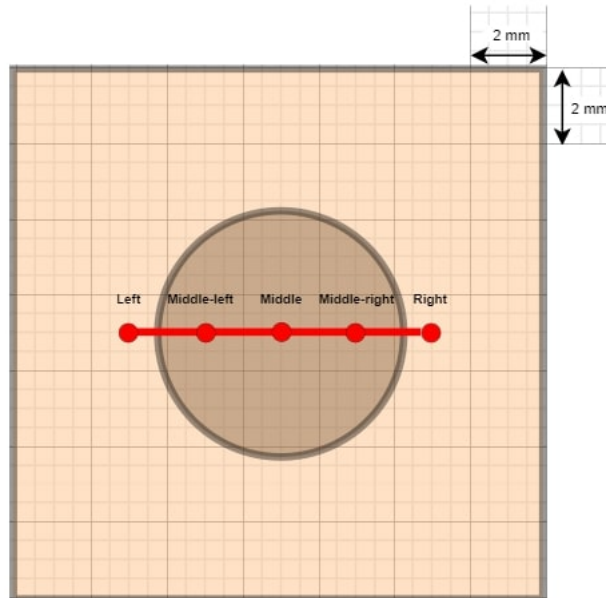


Fig. 6.7: Measurements across the linear segment over the tumor.

dielectric properties are lower than the other locations “Middle-left”, “Middle” and “Middle-right” that covers tumor regions. The dielectric contrast between the tumor region and adjoining skin is expected since malignant tissues are considered to have more water content and consequently the higher dielectric properties than normal tissues. The dielectric property of each location also varies in between months, which indicates that probe is also sensing the thickness variation of tumor. We evaluated the percentage difference between healthy adjoining skin measured on the left side of tumor and middle point of tumor representing different thicknesses of tumor. It is found to be 6.1%, 24.2%, 46.0%, 29.3%, 21.4%, 51.5% in terms of permittivity and 15.8%, 35.2%, 66.9%, 44.8%, 33.4%, 83.7% in terms of conductivity, for months 0, 6, 8, 12, 16 and 22 which clearly captures the variation in the dielectric properties as perceived by the probe. Further, we have observed discrepancy in measuring

“Middle-left” and “Right” locations in month 0 and month 16, which is not present in all other cases. This could be due to the placement error of the probe, which can be avoided by being more careful while placing the probe at the measuring point. Since measured dielectric properties of malignant melanoma were not available in literature, we compared our measured results with estimated dielectric properties of melanoma using Lichtenecker’s model as computed by B. J. Mohammed *et al.* [28]. The complex effective dielectric property of malignant melanoma is determined using Lichtenecker’s mixture formula given as:

$$\hat{\epsilon}_{UNH} = \left(\epsilon_W^{\frac{\beta-\alpha}{1-\alpha}} \epsilon_H^{\frac{1-\beta}{1-\alpha}} \right)' - j \left(\epsilon_W^{\frac{\beta-\alpha}{1-\alpha}} \epsilon_H^{\frac{1-\beta}{1-\alpha}} \right)'' \quad (6.4)$$

where $\hat{\epsilon}_{UNH}$ is the effective dielectric properties of unhealthy skin and ϵ_W and ϵ_H are the dielectric properties of water and healthy skin obtained from literature [47]. Water content information for healthy skin, $\alpha = 0.491$ and unhealthy skin that is malignant melanoma, $\beta = 0.638$ is taken from [48]. The dielectric properties obtained using the above formula were slightly different from the reference. This is expected as the computed value of unhealthy skin depend upon the values assigned for healthy skin and water in the Eq. 6.4, but the trend shown by the curves was similar. The results indicate that the measured permittivity values are lower for all months of 0, 6, 8, 12, 16, 22 as compared to the literature values but, they follow the similar trend. However, conductivity on the other hand, presents closer representation to the literature values for all months considered.

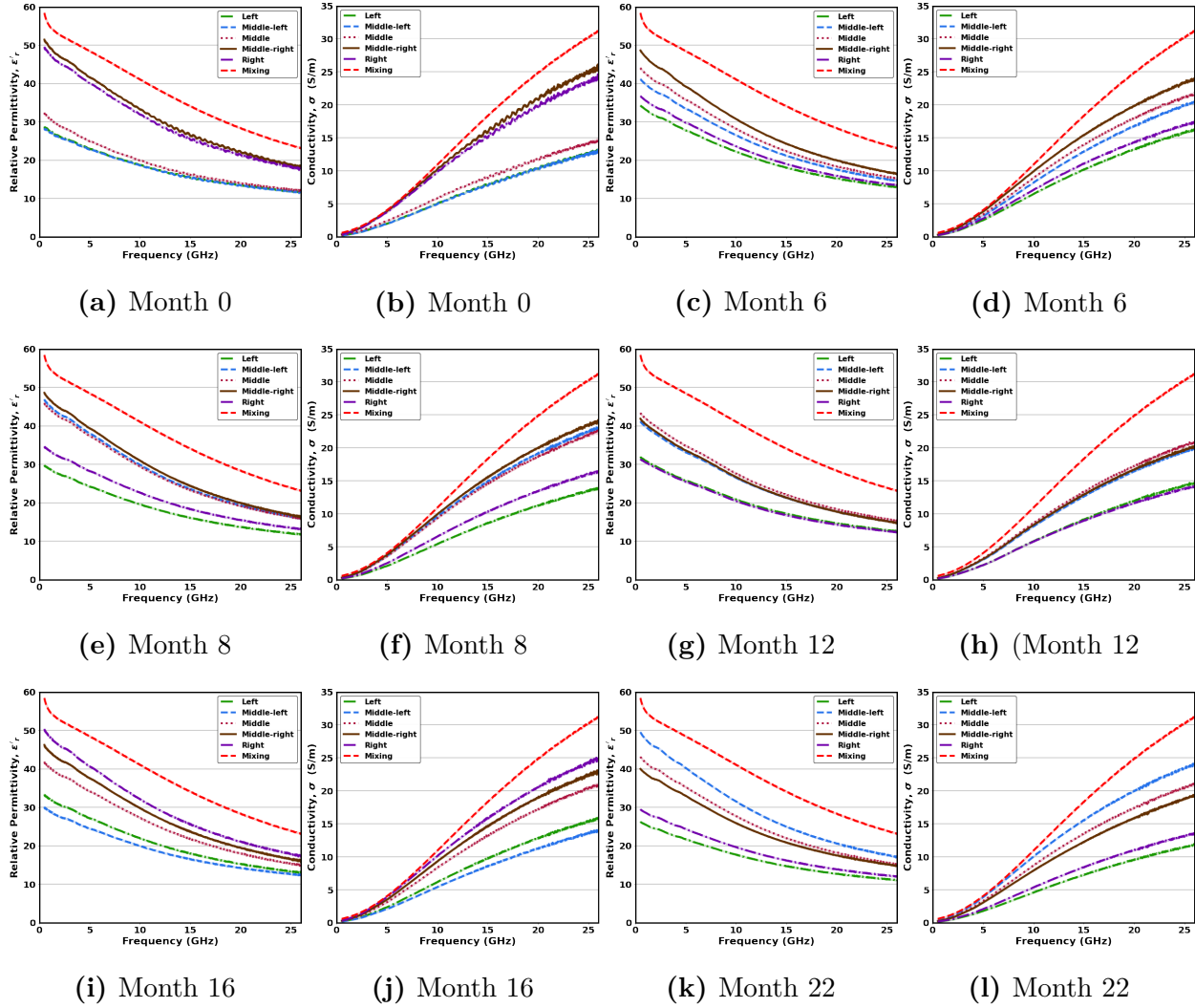


Fig. 6.8: Measured relative permittivity and conductivity of tumor with radial and vertical growth in Month 0 (a) and (b), Month 6 (c) and (d), Month 8 (e) and (f), Month 12 (g) and (h), Month 16 (i) and (j) and Month 22 (k) and (l).

6.3.2 Tumor profile across the grid

Next, the tumor profile is scanned by the probe following a grid of points as given in Fig 6.9. For this, a 10 mm × 10 mm grid is selected, where tumor is located at the center.

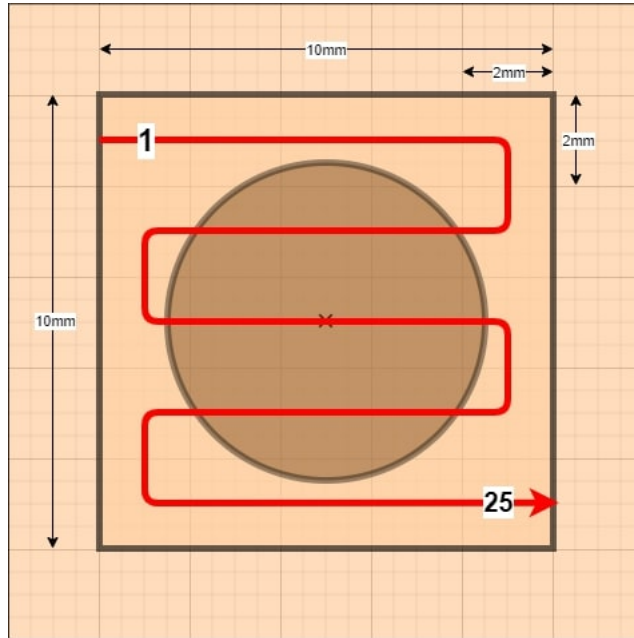


Fig. 6.9: Measurement of tumor profile along the points of a grid.

The area enclosed by the black square in the figure is the area of the test sample observed by the probe. We took measurements by placing the probe centered at the top-left square marked by point 1. Then platform was lowered and moved by 2 mm to align with the next square and step is repeated until the entire grid is spanned, and last square, marked as 25 is measured. The collected data was analyzed in the form of 2D dielectric maps which show relative permittivity and conductivity at each data point. The measurements were repeated for tumor phantoms presenting progression in months 0, 6, 8, 12, 16 and 22. Visualization of the results is accomplished in MATLAB using `contourf()` and `imagesc()` functions. The role of `contourf()` function is to create a continuous surface map from the acquired data using interpolation technique while `imagesc()` function assigns a color to each of the 25 squares

across the 10 by 10 mm grid using a common color scale. These maps are generated for the frequency of 20 GHz as it provides suitable penetration of electric fields which are required to identify tumor in skin. Permittivity and conductivity image maps are shown in Fig 6.10 (a) and (b) respectively.

In these dielectric maps, we see that the location with higher relative permittivity corresponds to the regions shaded in yellow and the location with lower relative permittivity corresponds to the regions shaded in dark blue. Thus, it can be seen that the proposed approach is able to identify tumors in the adjoining healthy skin.

6.4 Conclusion

Skin cancer diagnosis becomes challenging especially when tumor grows vertically. This paper presented a study of observing variation in the dielectric properties of a modeled melanoma tumor with radial and vertical growth at different stages of tumor progression. In order to achieve this, this paper concentrated on the development of a tumor progression model representing radial and vertical growth phases. As the design of phantom models is critical to evaluate the performance of systems intended for medical use, oil-in-gelatin phantom models have been developed based on the developed tumor progression model. These phantoms have been characterized with the Keysight slim form probe, which is chosen due to its small size (with diameter of 2.2 mm) as it is considered to be effective in measuring small sample areas.

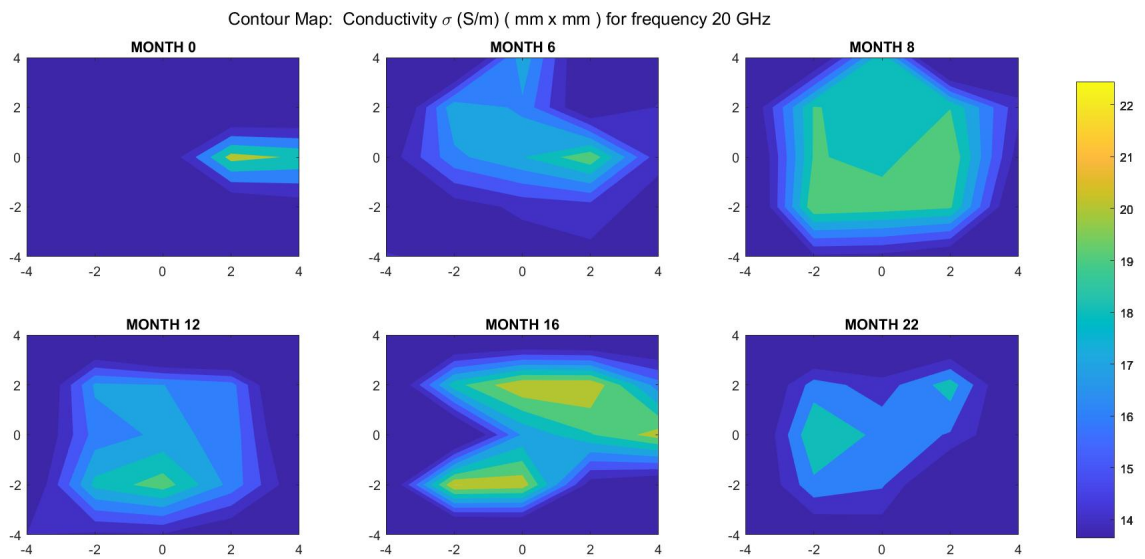
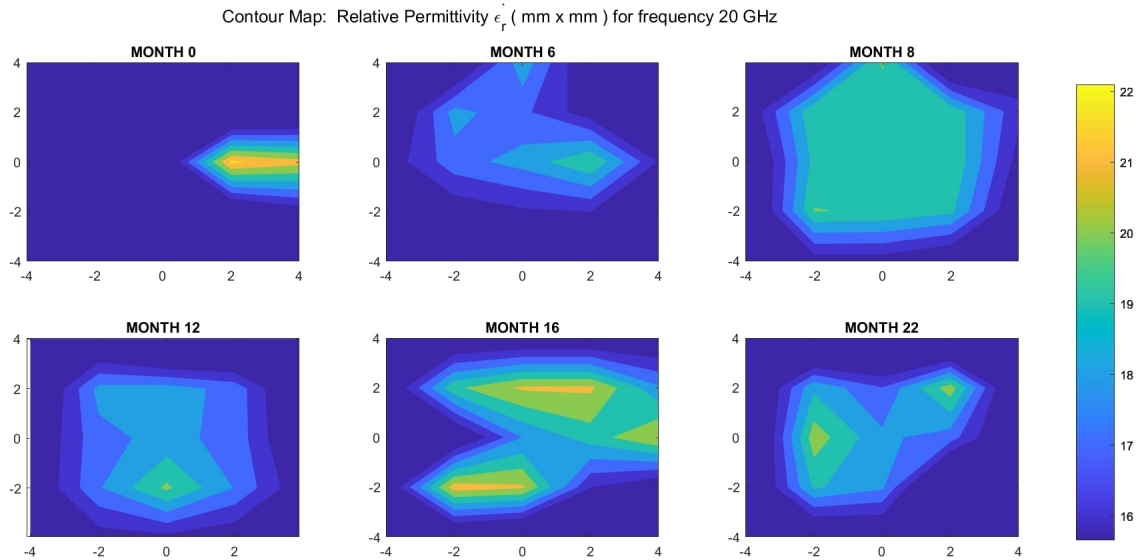


Fig. 6.10: Dielectric permittivity (a) and conductivity maps (b) for suspected region in the Months 0, 6, 8, 12, 16 and 22.

The dielectric properties in two different scenarios were evaluated. First, tumor size variation is observed by moving the probe over the tumor along the linear segment. In the second case, the tumor dielectric profile is observed by spanning the probe over the tumor in a grid format. Results indicate that the probe is able to sense change in dielectric properties of tumors even with non-uniform thickness. Moreover, significant contrast is observed between adjoining healthy skin and malignant tumor. Thus, presented results have the potential to be utilized in identifying tumors of varying size at any stage of tumor progression.

6.5 Acknowledgment

The study was supported in part by the Natural Sciences and Engineering Research Council of Canada (NSERC) Discovery under Grant RGPIN-2019-05850 and in part by Collaborative Research and Development under Grant CRD 521870-17. We extend special gratitude to Dr. Thomas Szkopek (McGill University) for providing the laboratory facilities. The authors would also like to thank Leon Hovsep Baronijan (at the time of this manuscript, undergraduate student at Western University), and Reza Shamsaee Malfajani (Graduate student, Polytechnique Montréal) for valuable discussions.

References

- [1] O. Abuzagheh, B. D. Barkana, and M. Faezipour, “Noninvasive Real-Time Automated

- Skin Lesion Analysis System for Melanoma Detection and Prevention,” *IEEE Journal of Translational Engineering in Health and Medicine*, vol. 3, pp. 1-12, 2015, doi: 10.1109/JTEHM.2015.2419612.
- [2] American Cancer Society, Cancer Facts & Figures 2022, Accessed: July 10, 2022. [Online]. Available: <https://www.cancer.org/content/dam/cancer-org/research/cancer-facts-and-statistics/annual-cancer-facts-and-figures/2022/2022-cancer-facts-and-figures.pdf>.
- [3] R. Zhang, K. Yang, B. Yang, N. A. Abuali, M. Hayajneh, M. Philpott, Q. H. Abbasi and A. Alomainy, “Dielectric and Double Debye Parameters of Artificial Normal Skin and Melanoma,” *Journal of Infrared, Millimeter, and Terahertz Waves*, vol. 40, no. 6, pp. 657-672, 2019, doi: 10.1007/s10762-019-00597-x.
- [4] J. Jaworek-Korjakowska, “Computer-Aided Diagnosis of Micro-Malignant Melanoma Lesions Applying Support Vector Machines,” *BioMed Research International*, vol. 2016, Article ID. 4381972, 2016, doi: 10.1155/2016/4381972.
- [5] C. Urso, “Are growth phases exclusive to cutaneous melanoma?,” *Journal of Clinical Pathology*, vol. 57, no. 5, pp. 560, May 2004, doi: 10.1136/jcp.2003.014852.
- [6] Melanoma Institute Australia, Pathology and Staging, Accessed: July 10, 2022. [Online]. Available: https://melanoma.org.au/wp-content/uploads/2021/10/PATHOLOGY_and_STAGING_FA.pdf.

- [7] M. J. Lin, V. Mar, C. McLean, and J. W. Kelly, "An objective measure of growth rate using partial biopsy specimens of melanomas that were initially misdiagnosed," *Journal of the American Academy of Dermatology*, vol. 71, no. 4, pp. 691-697, 2014, doi: <https://doi.org/10.1016/j.jaad.2014.04.068>.
- [8] A. T. Young, N. B. Vora, J. Cortez, A. Tam, Y. Yeniay, L. Afifi, D. Yan, A. Nosrati, A. Wong, A. Johal, M. L. Wei, "The role of technology in melanoma screening and diagnosis," *Pigment Cell & Melanoma Research*, vol. 34, no. 2, pp. 288-300, 2021, doi: [10.1111/pcmr.12907](https://doi.org/10.1111/pcmr.12907).
- [9] C. Barata, M. E. Celebi, and J. S. Marques, "A Survey of Feature Extraction in Dermoscopy Image Analysis of Skin Cancer," *IEEE Journal of Biomedical and Health Informatics*, vol. 23, no. 3, pp. 1096-1109, 2019, doi: [10.1109/JBHI.2018.2845939](https://doi.org/10.1109/JBHI.2018.2845939).
- [10] J. N. Saeed and S. R. M. Zeebaree, "Skin Lesion Classification Based on Deep Convolutional Neural Networks Architectures", *Journal of Applied Science and Technology Trends*, vol. 2, no. 01, pp. 41 - 51, Mar. 2021.
- [11] F. Töpfer, S. Dudorov, and J. Oberhammer, "Millimeter-Wave Near-Field Probe Designed for High-Resolution Skin Cancer Diagnosis," *IEEE Transactions on Microwave Theory and Techniques*, vol. 63, no. 6, pp. 2050-2059, 2015, doi: [10.1109/TMTT.2015.2428243](https://doi.org/10.1109/TMTT.2015.2428243).
- [12] F. Töpfer, "Micromachined Microwave Sensors for Non-Invasive Skin Cancer

- Diagnostics,” PhD dissertation, KTH Royal Institute of Technology, 2019.
- [13] R. Nakayama-Takeda, S. Sakakibara, M. Kurokawa, K. Hashikawa, and H. Terashi, “Comparison of malignant skin tumor thickness and relative depth of invasion estimates from preoperative MR-microscopy and pathological evaluation,” *Dermatologic Surgery*, vol. 39, no. 12, pp. 1767-1773, Dec 2013, doi: 10.1111/dsu.12371.
- [14] A. Taeb, S. Gigoyan and S. Safavi-Naeini, “Millimetre-wave waveguide reflectometers for early detection of skin cancer”, *IET Microw. Antennas Propag.*, vol. 7, no. 14, pp. 1182-1186, Nov. 2013.
- [15] A. Blundo, A. Cignoni, T. Banfi, and G. Ciuti, “Comparative Analysis of Diagnostic Techniques for Melanoma Detection: A Systematic Review of Diagnostic Test Accuracy Studies and Meta-Analysis,” *Frontiers in Medicine*, vol. 8, Article 637069, April 2021, doi: 10.3389/fmed.2021.637069.
- [16] Cancer Treatment Centers of America, Diagnosing Skin Cancer, Accessed: August 22, 2022. [Online]. Available:<https://www.cancercenter.com/cancer-types/skin-cancer/diagnosis-and-detection>.
- [17] C. Aydinalp, S. Joof, and T. Yilmaz, “Microwave Dielectric Property Based Stage Detection of Skin Cancer,” in *2021 XXXIVth General Assembly and Scientific Symposium of the International Union of Radio Science (URSI GASS)*, 28 Aug.4 - Sept. 2021, pp. 1-4, doi: 10.23919/URSIGASS51995.2021.9560438.

- [18] M. A. Aldhaeabi, K. Alzoubi, T. S. Almoneef, S. M. Bamatraf, H. Attia, and O. M. Ramahi, "Review of microwaves techniques for breast cancer detection," *Sensors*, vol. 20, no. 8, pp. 2390, 2020.
- [19] M. T. Islam, M. Samsuzzaman, S. Kibria, and M. T. Islam, "Experimental Breast Phantoms for Estimation of Breast Tumor Using Microwave Imaging Systems," *IEEE Access*, vol. 6, pp. 78587-78597, 2018, doi: 10.1109/ACCESS.2018.2885087.
- [20] A. Fornes-Leal, C. Garcia-Pardo, M. Frasson, V. Pons Beltrán, and N. Cardona, "Dielectric characterization of healthy and malignant colon tissues in the 0.5–18 GHz frequency band," *Physics in Medicine & Biology*, vol. 61, no. 20, pp. 7334-7346, Oct 21, 2016, doi: 10.1088/0031-9155/61/20/7334.
- [21] S. Huang, W. Cai, S. Han, *et al.*, "Differences in the dielectric properties of various benign and malignant thyroid nodules," *Medical Physics*, vol. 48, no. 2, pp.760-769, 2021, doi: 10.1002/mp.14562.
- [22] F. Töpfer, S. Dudorov, and J. Oberhammer, "Micromachined 100GHz near-field measurement probe for high-resolution microwave skin-cancer diagnosis," *in 2012 IEEE/MTT-S International Microwave Symposium Digest*, 17-22 June 2012, pp. 1-3, doi: 10.1109/MWSYM.2012.6259671.
- [23] H. Arab, L. Chioukh, M. D. Ardakani, S. Dufour, and S. O. Tatu, "Early-Stage Detection of Melanoma Skin Cancer Using Contactless Millimeter-Wave Sensors,"

- IEEE Sensors Journal*, vol. 20, no. 13, pp. 7310-7317, 2020, doi: 10.1109/JSEN.2020.2969414.
- [24] G. Mansutti, A. T. Mobashsher, K. Bialkowski, B. Mohammed, and A. Abbosh, "Millimeter-Wave Substrate Integrated Waveguide Probe for Skin Cancer Detection," *IEEE Transactions on Biomedical Engineering*, vol. 67, no. 9, pp. 2462-2472, Sept. 2020, doi: 10.1109/TBME.2019.2963104.
- [25] A. Mirbeik-Sabzevari, S. Li, E. Garay, H. -T. Nguyen, H. Wang and N. Tavassolian, "Synthetic Ultra-High-Resolution Millimeter-Wave Imaging for Skin Cancer Detection," *IEEE Transactions on Biomedical Engineering*, vol. 66, no. 1, pp. 61-71, Jan. 2019, doi: 10.1109/TBME.2018.2837102.
- [26] J. Boparai and M. Popović, "Development and Characterization of Skin Phantoms at Microwave Frequencies," *IEEE Journal of Electromagnetics, RF and Microwaves in Medicine and Biology*, vol. 6, no. 3, pp. 296-304, Sept. 2022, doi: 10.1109/JERM.2022.3143374.
- [27] J. Boparai and M. Popović, "Heterogeneous Skin Phantoms for Experimental Validation of Microwave-Based Diagnostic Tools," *Sensors*, vol. 22, no. 5, 1955, 2022, doi: 10.3390/s22051955.
- [28] B. J. Mohammed, S. A. R. Naqvi, M. Manoufali, K. Bialkowski and A. M. Abbosh, "Changes in epidermal dielectric properties due to skin cancer across the band 1 to

- 50 GHz,” *2018 Australian Microwave Symposium (AMS)*, 2018, pp. 77-78, doi: 10.1109/AUSMS.2018.8346990.
- [29] J. Beer, L. Xu, P. Tschandl and H. Kittler, “Growth rate of melanoma in vivo and correlation with dermatoscopic and dermatopathologic findings,” *Dermatology Practical & Conceptual*, vol. 1, no. 1, pp. 59-67, 2011, doi: 10.5826/dpc.0101a13.
- [30] W. E. Damsky, L. E. Rosenbaum, M. Bosenberg, “Decoding melanoma metastasis,” *Cancers (Basel)*, vol. 3, no. 1, pp. 126-163, Dec 2010, doi: 10.3390/cancers3010126. PMID: 24212610; PMCID: PMC3756353.
- [31] R. Shayan, M. G. Achen and S. A. Stacker, “Lymphatic vessels in cancer metastasis: bridging the gaps,” *Carcinogenesis*, vol. 27, no. 9, pp. 1729-1738, Sept. 2006, doi: 10.1093/carcin/bgl031.
- [32] A. I. Mendes, C. Nogueira, J. Pereira, and R. Fonseca-Pinto, “On the geometric modulation of skin lesion growth: a mathematical model for melanoma,” *Research on Biomedical Engineering*, vol. 32, no. 1, pp. 44-54, 2016, doi: <http://dx.doi.org/10.1590/2446-4740.02815>.
- [33] W. Liu, J. P. Dowling, W. K. Murray, G. A. McArthur, J. F. Thompson, R. Wolfe and J. W. Kelly, “Rate of growth in melanomas: characteristics and associations of rapidly growing melanomas,” *Archives of dermatology*, vol. 142, no. 12, pp. 1551-1558, 2006, doi:10.1001/archderm.142.12.1551.

- [34] N. R. Abbasi, M. Yancovitz, D. Gutkowicz-Krusin, K. S. Panageas, M. C. Mihm, P. Googe, R. King, V. Prieto, I. Osman, R. J. Friedman, D. S. Rigel, A. W. Kpof, D. Polsky, "Utility of lesion diameter in the clinical diagnosis of cutaneous melanoma," *Archives of dermatology*, vol, 144, no. 4, pp. 469-474, 2008, doi:10.1001/archderm.144.4.469.
- [35] T. A. Martin, L. Ye, A. J. Sanders, J. Lane, and W. G. Jiang, "Cancer invasion and metastasis: molecular and cellular perspective," *In Madame Curie Bioscience Database* [Internet], Landes Bioscience, 2013.
- [36] B. Alberts, A. Johnson, J. Lewis, M. Raff, K. Roberts and P. Walter, "Cancer as a microevolutionary process," *In Molecular Biology of the Cell*, 4th edition, Garland Science, 2002.
- [37] S. B. Edge, D. R. Byrd, C. C. Compton, A. G. Fritz, F. L. Greene and A. Trotti, *AJCC Cancer Staging Manual*, 7th Edition, Springer, New York, 2010.
- [38] K. Guido, C. Matos, J. Ramsey and A. Kiourti, "Tissue-Emulating Phantoms for In Vitro Experimentation at Radio Frequencies: Exploring characteristics, fabrication, and testing methods," *IEEE Antennas and Propagation Magazine*, vol. 63, no. 6, pp. 29-39, Dec. 2021, doi: 10.1109/MAP.2020.3003208.
- [39] A. Malliori, A. Daskalaki, A. Dermitzakis, and N. Pallikarakis, "Development of physical breast phantoms for X-ray imaging employing 3D printing techniques," *The*

- Open Medical Imaging Journal*, vol. 12, pp. 1–10, 2020, doi: 10.2174/1874347102012010001.
- [40] E. Porter, J. Fakhoury, R. Oprisor, M. Coates and M. Popović, “Improved tissue phantoms for experimental validation of microwave breast cancer detection,” *Proceedings of the Fourth European Conference on Antennas and Propagation*, pp. 1-5, 2010.
- [41] M. Lazebnik, E. L. Madsen, G. R. Frank, S. C. Hagness, “Tissue-mimicking phantom materials for narrowband and ultrawideband microwave applications,” *Physics in Medicine & Biology*, vol. 50, no. 18, pp. 4245-4258, Sept. 2005, doi: 10.1088/0031-9155/50/18/001.
- [42] Y. Gao, M. T. Ghasr, M. Nacy and R. Zoughi, “Towards accurate and wideband in vivo measurement of skin dielectric properties,” *IEEE Transactions on Instrumentation and Measurement*, vol. 68, no. 2, pp. 512-524, Feb. 2019, doi: 10.1109/TIM.2018.2849519.
- [43] N1501A Dielectric Probe Kit, Accessed: July 10, 2022. [Online]. Available: <https://www.keysight.com/ca/en/assets/7018-04631/technical-overviews/5992-0264.pdf>
- [44] N9918A FieldFox Handheld Microwave Analyzer, 26.5 GHz, Accessed: July 10, 2022. [Online]. Available: <https://www.keysight.com/ca/en/product/N9918A/fieldfox-a-handheld-microwave-analyzer-26-5-ghz.html>

- [45] A. La Gioia, E. Porter, I. Merunka, A. Shahzad, S. Salahuddin, M. Jones and M. O'Halloran, "Open-Ended Coaxial Probe Technique for Dielectric Measurement of Biological Tissues: Challenges and Common Practices," *Diagnostics (Basel)*, vol. 8, no. 2, pp. 40, June 2018, doi: 10.3390/diagnostics8020040.
- [46] K. S. Zubair, S. A. Alhuwaidi, H. H. Song, Y. G. Shellman, W. A. Robinson, A. J. Applegate and C. M. Amato, "Investigation of dielectric spectroscopy response in normal and cancerous biological tissues using S-parameter measurements," *Journal of Electromagnetic Waves and Applications*, vol. 32, no. 8, pp. 956-971, doi: 10.1080/09205071.2017.1411835.
- [47] S. Gabriel, R. W. Lau, and C. Gabriel, "The dielectric properties of biological tissues: III. Parametric models for the dielectric spectrum of tissues," *Physics in Medicine & Biology*, vol. 41, no. 11, pp. 2271–2293, 1996, doi: 10.1088/0031-9155/41/11/003.
- [48] A. Mirbeik-Sabzevari, R. Ashinoff, R. and N. Tavassolian, "UltraWideband Millimeter-Wave Dielectric Characteristics of Freshly-Excised Normal and Malignant Human Skin Tissues," *IEEE Transactions on Biomedical Engineering*, vol. 65, no. 6, pp. 1320-1329, June 2018, doi:10.1109/TBME.2017.2749371.

Chapter 7

Numerical Analysis of Characterized Skin Phantoms and SAR Evaluation

This chapter is based on the following manuscript:

J. Boparai, Y. Wei, M. Mokhtari and M. Popović, “Numerical Analysis of Characterized Skin Phantoms and SAR Evaluation,” in submission to the *IEEE Microwave and Wireless Components Letters*.

Preface to Chapter 7: This chapter describes how we compare the experimental characterization of skin-fat phantom models (skin thickness variation 0.5 – 5 mm at 0.5 mm increments) with numerical modeling and simulations. The variability of skin thickness is important while designing accurate microwave-based skin anomaly detection prototypes.

To analyze the effect of aperture size of probe on SAR distribution in the biological tissue and to confirm the compliance with the safety standards, probes with different aperture sizes were simulated and analyzed.

Abstract—Consideration of skin thickness variability is vital for the design and development of accurate, reliable and highly sensitive microwave-based skin anomaly detection prototypes. This work presents numerical modeling of a slim-form open-ended coaxial probe terminated by a skin-fat model, where skin thickness varies 0.5 – 5 mm in 0.5 mm increments and compares it to results obtained from measuring experimental phantom models. Next, to assess the electromagnetic field distribution in the biological tissues and to confirm compliance with safety standards, a dielectric probe with different aperture sizes is modeled. It is observed from the results that for all probe sizes, the 1-g average SAR stays well below the safety limit of 1.6 W/kg.

Index Terms—aperture size, dielectric measurements, microwave, open-ended coaxial probe, specific absorption rate (SAR)

7.1 Introduction

Skin is the body’s largest organ that covers its entire surface, varying in thickness due to number of factors like age, gender, race and location on the body [1]. Extensive investigation of impact of variability of skin thickness on dielectric property measurement is required to design a reliable prototype for anomaly diagnosis and to properly assess the interaction of electromagnetic (EM) fields with the human body.

We developed and characterized oil-in-gelatin experimental skin phantoms with thickness

7. Numerical Analysis of Characterized Skin Phantoms and SAR Evaluation¹⁵⁸

ranging 0.5 – 5 mm with 0.5 mm increments, covering all areas of body where skin cancer commonly occurs and placed on a 7 mm fat phantom. The precise thickness of skin phantoms was acquired by constructing 3D printed cylindrical molds [2]. The fabricated phantoms, 3D printed molds and fabrication stage of pouring skin mimicking material in 3D printed cylindrical molds for solidification is shown in Fig. 7.1.



Fig. 7.1: Fabricated skin phantoms with thickness varying 0.5 – 5 mm with 0.5 mm increments and 8 mm thick control skin phantom (top left), 3D printed cylindrical molds (bottom) and skin mimicking material poured into 3D printed molds at final fabrication step (top right).

The present study draws a comparison of the simulated and experimental dielectric measurements of the skin-fat phantom model with varying skin thicknesses using a slim-form open-ended coaxial probe in the microwave frequency range. Further, to confirm compliance with the safety standards, the numerical modeling of the dielectric probe with different aperture sizes is used to assess the electromagnetic field distribution in the biological tissues, which is quantified by the specific absorption rate (SAR) given by the

7. Numerical Analysis of Characterized Skin Phantoms and SAR Evaluation 159

equation 7.1:

$$\text{SAR} = \frac{\sigma |E|^2}{\rho}, \text{ [W/kg]} \quad (7.1)$$

where E is the electric field strength [V/m], σ is the conductivity [S/m] and ρ is the mass density of the tissue [kg/m³].

SAR represents the absorption of energy per unit mass and is expressed as W/kg. A number of organizations such as the Federal Communication Commission (FCC), IEEE Standard C95.1, International Commission on Non-Ionizing Radiation Protection (ICNIRP), set safety limits of peak 10-g averaged SAR <2.0 W/kg (ICNIRP) and peak 1-g averaged SAR <1.6 W/kg (FCC) [3].

7.2 Methodology

7.2.1 Simulation Setup and Permittivity Extraction

Numerical simulations of Keysight slim-form open-ended coaxial probe [4] terminated by a skin-fat model with varying skin thicknesses are performed using Ansys HFSS based on the finite element method (FEM). To best match the experimental probe, the slim form probe is modeled as a Teflon-filled nickel probe with a 2.2 mm diameter as per Keysight's specifications. In our design, the radius of the inner conductor, a is 0.24 mm and the radius of the outer conducting shield, b is 0.8 mm. The length of the probe is 30 mm (due to

7. Numerical Analysis of Characterized Skin Phantoms and SAR Evaluation¹⁶⁰

negligible impact on results), chosen arbitrarily, as the effect of the probe's length on the reflection coefficients (S_{11}) will ultimately be removed by the de-embedding process. This configuration ensures that the characteristic impedance of the probe is 50Ω .

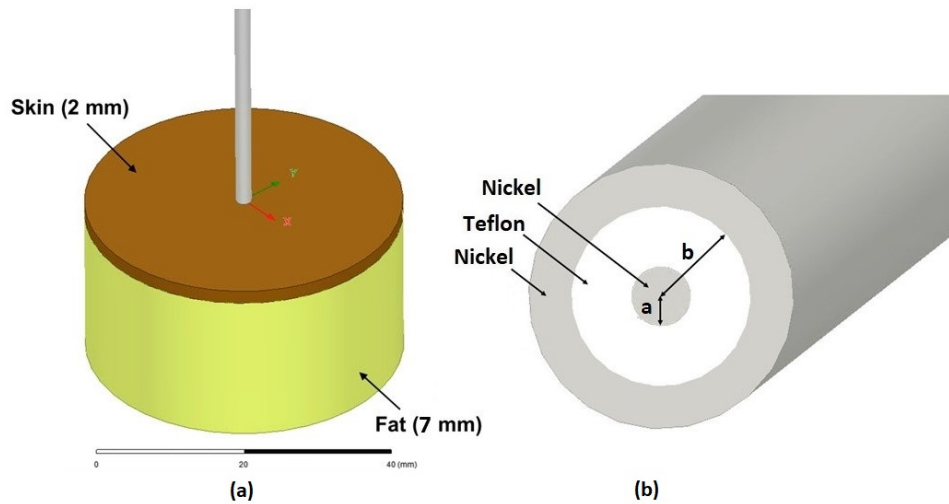


Fig. 7.2: (a) Schematic geometry of the modeled probe in contact with the skin-fat sample under investigation and (b) dimensions (a is the radius of the inner conductor, b is the radius of the outer conductor) and material of the probe.

To replicate the phantom designs used in our experiments, we model the skin and fat phantoms as a double-layered cylinder in the simulation. The frequency-dependent dielectric properties (relative permittivity and loss tangent) of these materials were obtained from the literature [5] and assigned to a simulation model over the frequency range of 0.5 – 26.5 GHz. We set the radius of the cylinder to 20 mm which sufficiently covers the sensing range of the probe. The thickness of the skin layer is the variable parameter of interest in our analysis and the thickness of the fat layer is kept constant at 7 mm. Fig. 7.2(a) shows the schematic

7. Numerical Analysis of Characterized Skin Phantoms and SAR Evaluation 161

geometry of the modeled probe in contact with the skin-fat sample under investigation and Fig. 7.2(b) describes dimensions and material of the probe.

In the simulations, the skin-fat model is placed directly under the probe and complex reflection coefficients (S11) for frequencies 0.5 – 26.5 GHz with a step size of 0.2 GHz were obtained as outputs. During post-processing, the reflection coefficients are de-embedded so that the reference plane is moved from the top of the probe to the aperture plane. This removes confounding phase changes caused by wave propagation within the body of the probe. A parametric analysis of the skin thickness was setup in the simulation environment to obtain outputs for skin thickness ranging from 0 mm (fat layer only) to 5 mm, with 0.5 mm increments.

Finally, the reflection coefficients (S11) obtained from the simulations are converted to complex permittivity (relative permittivity (ϵ_r) and conductivity (σ)) of the tissue under test using the antenna model for the open-ended coaxial probe [6]. The antenna model was chosen due to its high accuracy and low computation time based on preliminary investigations in which extracted permittivity and theoretical results were compared [7]. The calibration of antenna model is performed by measuring reflection coefficients of four reference materials. Hence, we obtained the reflection coefficient values for open, short, water and acetone. We then employed an PyOECF open-source software library [8] with the implemented antenna model to perform the extraction of permittivity and conductivity using the equation 7.2:

7. Numerical Analysis of Characterized Skin Phantoms and SAR Evaluation 162

$$G(\varepsilon_{MUT}^A)^{5/2} + \varepsilon_{MUT}^A + \frac{\Gamma_{MUT,2}\Gamma_{1,3}}{\Gamma_{MUT,1}\Gamma_{3,2}}(\varepsilon_3 + G\varepsilon_3^{5/2}) + \frac{\Gamma_{MUT,3}\Gamma_{2,1}}{\Gamma_{MUT,1}\Gamma_{3,2}}(\varepsilon_2 + G\varepsilon_3^{5/2}) = 0 \quad (7.2)$$

where G is the normalized radial conductance and is given by:

$$G = \frac{-\Gamma_{4,1}\Gamma_{3,2}\varepsilon_4 + \Gamma_{4,2}\Gamma_{1,3}\varepsilon_3 + \Gamma_{4,3}\Gamma_{2,1}\varepsilon_2}{\Gamma_{4,1}\Gamma_{3,2}\varepsilon_4^{5/2} + \Gamma_{4,2}\Gamma_{1,3}\varepsilon_3^{5/2} + \Gamma_{4,3}\Gamma_{2,1}\varepsilon_2^{5/2}} \quad (7.3)$$

7.2.2 Probe Aperture Size Variation and SAR Evaluation

To analyze the effect of the probe aperture size on the SAR distribution within the tested tissues, three probe designs with different aperture sizes are modeled and analyzed using HFSS simulations. The overall configuration for SAR evaluation is identical to the setup described in section 7.2.1. The mass density of the skin is considered to be 1010 kg/m^3 and that of the fat layer be 900 kg/m^3 , based on literature values [9]. The parameters of this study, are given in Table 7.1.

Table 7.1: Probe dimensions for parametric analysis.

Designs	a (mm)	b (mm)
Small probe (Slim probe)	0.24	0.80
Medium probe (Performance probe)	1.41	4.75
Large probe	2.85	9.60

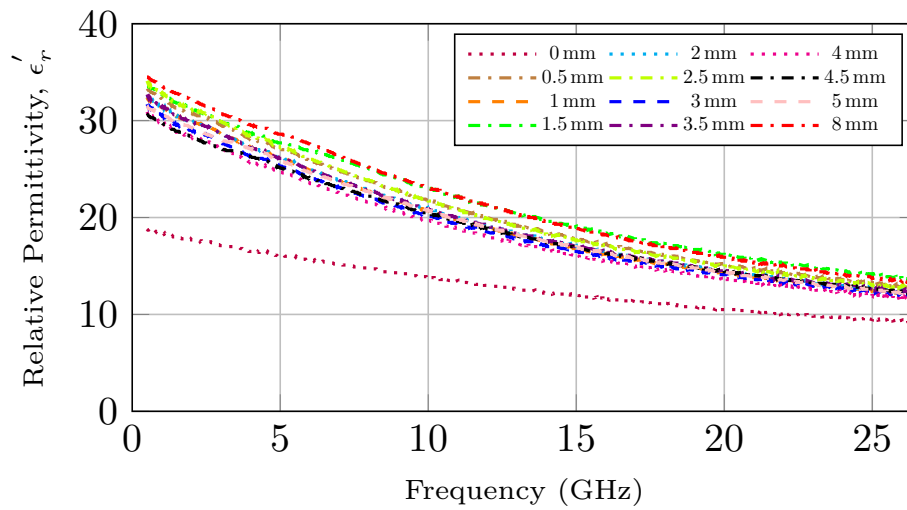
We first determined the SAR distribution within the tissue model across the frequency band of the probe and identified the locations of maximum SAR value. Since the SAR value

7. Numerical Analysis of Characterized Skin Phantoms and SAR Evaluation163

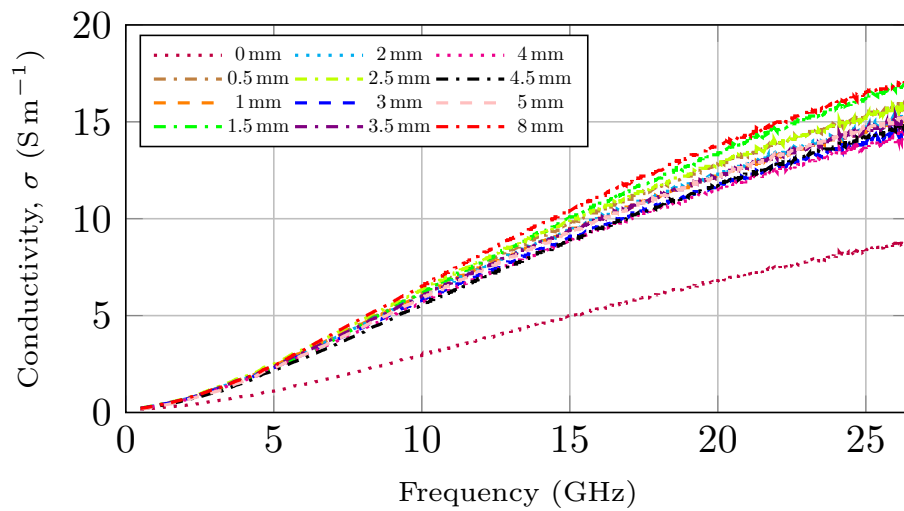
is directly proportional to the square of the electric field, this can be achieved by analyzing the electric field contour profile within the simulated tissue. One cross-sectional plot of the magnitude of electric field is sufficient to represent the field distribution within the entire structure due to the azimuthal symmetry of our configuration in which the coaxial probe is aligned to the axis of the tissue cylinder. The plots of electric field magnitude were obtained for the frequencies 0.5 – 26.5 GHz with a step size of 0.2 GHz. Next, for each design, we plot the peak local SAR values averaged over 1-g of the modelled tissue as a function of frequency for the input power of -10 dBm. The maximum value in the plot corresponds to the highest possible SAR values for a specific probe design, enabling a comprehensive safety assessment of the probe.

7.2.3 Results and Discussion

Fig. 7.3 and Fig. 7.4 illustrate the measured and simulated results of skin phantom models with thickness 0.5 – 5 mm, with 0.5 mm increments, placed on a 7 mm fat phantom model. A close agreement can be observed between the measured and simulated results as they do not deviate more than 15% from each other, across all the simulation and measurement results. The variation in relative permittivity and conductivity in the measured results is more pronounced with the variation of thickness than in the simulated results. This can be attributed to the variation in environmental factors (temperature, placement pressure) not incorporated in the simulations.

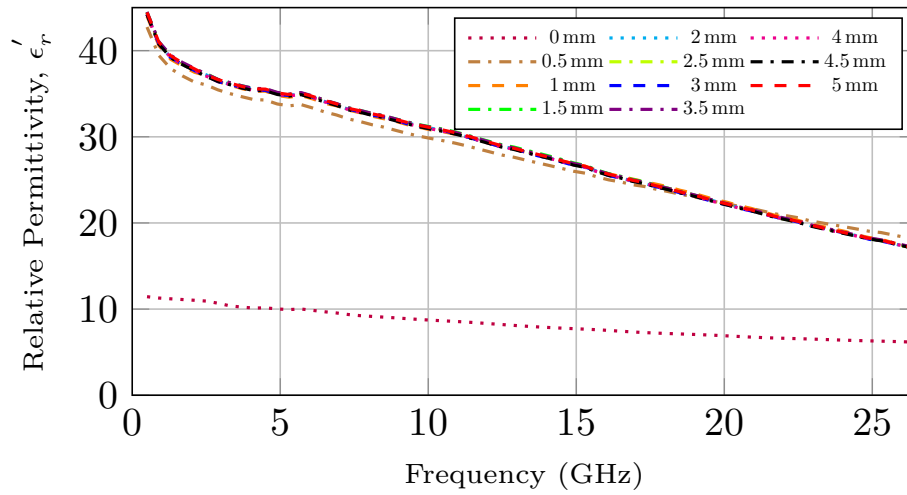


(a)

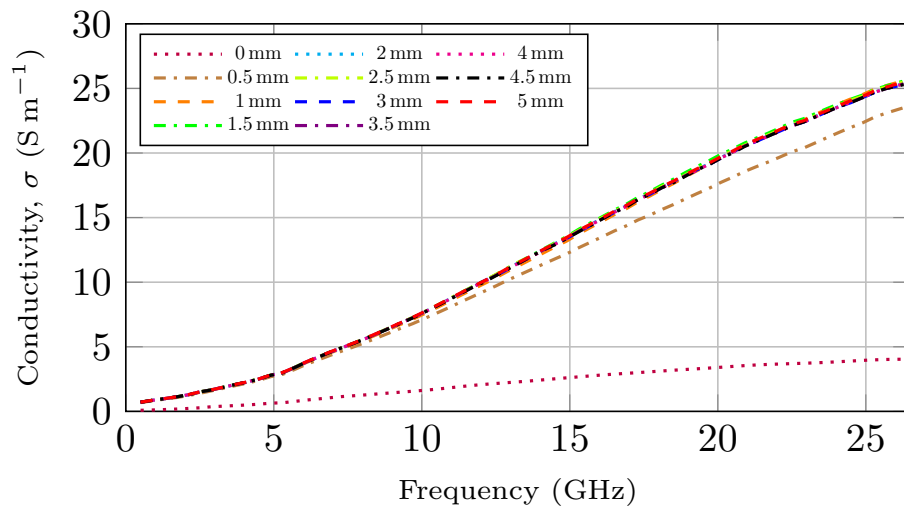


(b)

Fig. 7.3: Measured (a) Relative Permittivity and (b) Conductivity variation as a function of frequency at varying skin phantom thicknesses placed on fat phantom.



(a)



(b)

Fig. 7.4: Simulated (a) Relative Permittivity and (b) Conductivity variation as a function of frequency at varying skin phantom thicknesses placed on fat phantom.

7. Numerical Analysis of Characterized Skin Phantoms and SAR Evaluation 166

Next, to assess the safety of the probe, the 1-g average SAR inside the tissue is calculated over the whole frequency band for input power of -10 dBm and plotted in Fig. 7.5. The simulations are repeated for different sizes of the probe while keeping the input power unchanged. The plot shows that the 1-g average SAR stays well below the safety limit of 1.6 W/kg for all probe sizes. The frequency trend for Fig. 7.5 traces can be explained from equation 7.1. The conductivity is an increasing function of frequency while E-field strength decreases with frequency. The multiplication of the two results in relatively constant values for higher frequencies since their opposite trend cancels out each other. Moreover, the medium probe exhibit higher SAR levels compared to its counterparts. This is a result of the E-field distributions and the spatial averaging done to extract the 1-g average SAR values.

Lastly, Fig. 7.6 depicts the E -field distribution inside the tissue when irradiated by the three probes. Since the input power is unchanged, smaller probes reveal higher electric field levels while the larger probes display higher sensing depths and more uniform distributions. The uniformity and higher levels of E -field in the medium probe in Fig. 7.6(b), contribute to the higher 1-g average SAR in Fig. 7.5; because, in this case, all averaging voxels in the process of taking the spatial average over 1-g of tissue contribute to the resulting SAR value. This is not the case for the small probe in Fig. 7.6(a) as the E -fields decay rapidly as the distance from the probe core increases, resulting in many voxels with low E-field strengths being summed up in the averaging; this lowers the resulting average SAR. The large probe

7. Numerical Analysis of Characterized Skin Phantoms and SAR Evaluation 167

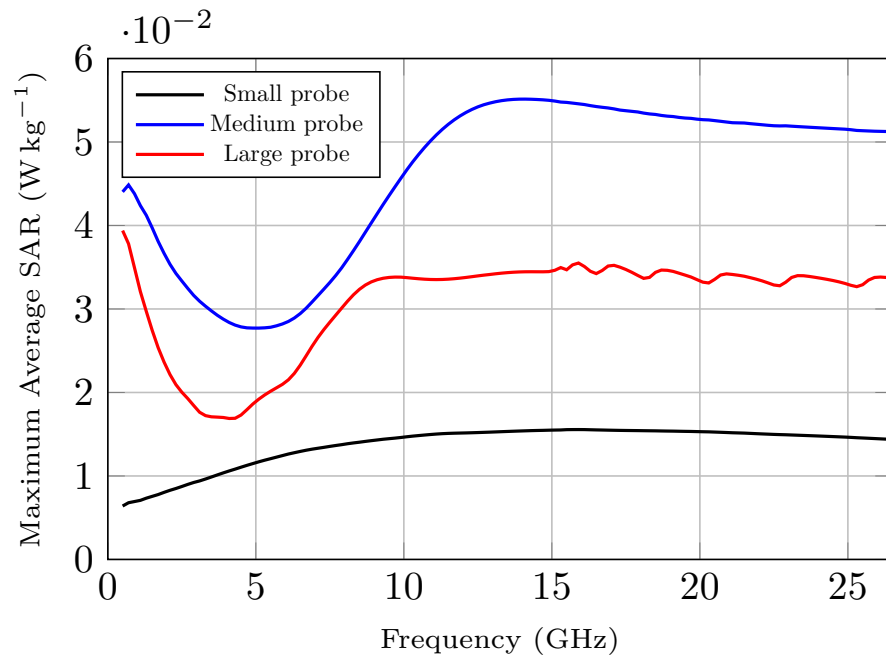
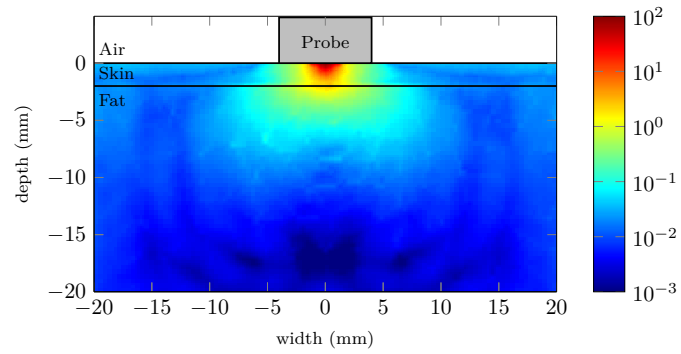
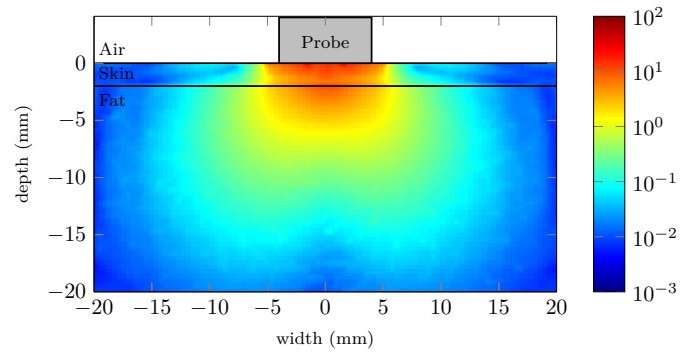


Fig. 7.5: Maximum 1-g average Specific Absorbance Rate (SAR) for the input power of -10 dBm as a function of frequency in the tissue for different probe sizes.

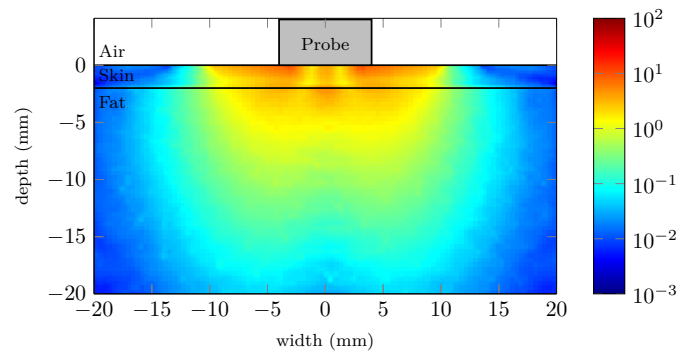
7. Numerical Analysis of Characterized Skin Phantoms and SAR Evaluation 168



(a)



(b)



(c)

Fig. 7.6: E -field distribution (V m^{-1}) at 15 GHz for the input power of -10 dBm inside the tissue for different probe sizes: (a) small probe, (b) medium probe and (c) large probe.

7. Numerical Analysis of Characterized Skin Phantoms and SAR Evaluation 169

of Fig. 7.6(c) shows decreased SAR levels compared to the medium probe, due to the E -field distribution over a larger cross-sectional surface.

7.3 Conclusion

The study presents the numerical modeling of the slim-form open-ended coaxial probe in contact with skin-fat tissue for skin thickness variation 0.5 – 5 mm, with 0.5 mm increments and observed the impact of skin thickness variability on dielectric properties. The permittivity and conductivity are extracted from recorded S11 parameters using the antenna model and compared with the measured results obtained from experimental phantoms. The measured results were found to be consistent with the simulated results. The effect of the aperture size of the probe on electromagnetic field variation in tissues was also studied via examining specific absorption rate (SAR) and E -field distributions inside the tissue for each probe.

7.4 References

- [1] M. C. Ziskin, S. I. Alekseev, K. R. Foster and Q. Balzano, “Tissue models for RF exposure evaluation at frequencies above 6 GHz,” *Bioelectromagnetics*, vol. 39, no. 3, pp.173-189, 2018, doi: 10.1002/bem.22110.
- [2] J. Boparai, Y. Jallouli, O. Miller, R. Tchinov and M. Popović, “Microwave

7. Numerical Analysis of Characterized Skin Phantoms and SAR Evaluation 170

- Characterization and Probe Sensing: Parametric Study with Skin Phantom Thickness,” *2022 IEEE MTT-S International Microwave Biomedical Conference (IMBioC)*, 2022, pp. 138-140, doi: 10.1109/IMBioC52515.2022.9790129.
- [3] K. N. Bocan, M. H. Mickle and E. Sejdić, ”Multi-Disciplinary Challenges in Tissue Modeling for Wireless Electromagnetic Powering: A Review,” *IEEE Sensors Journal*, vol. 17, no. 20, pp. 6498-6509, 15 Oct., 2017, doi: 10.1109/JSEN.2017.2748338.
- [4] Keysight, N1501A Dielectric Probe Kit 10 MHz to 50 GHz: Technical Overview, 2015. [Online]. Available: <http://www.keysight.com/en/pd-2492144-pn-N1501A/dielectric-probe-kit>. Accessed: September 2, 2022.
- [5] IFAC, Calculation of dielectric properties of body tissues in the frequency range 10 Hz-100 GHz, [Online]. Available: <http://niremf.ifac.cnr.it/tissprop/htmlclie/htmlclie.php>. Accessed: September 2, 2022.
- [6] D. Berube, F. M. Ghannouchi, and P. Savard, “A comparative study of four open-ended coaxial probe models for permittivity measurements of lossy dielectric/biological materials at microwave frequencies,” *IEEE Transactions on Microwave Theory and Techniques*, vol. 44, no. 10, pp. 1928–1934, Oct. 1996.
- [7] C. Sneha, “ICRU report 95 – Operational quantities for external radiation exposure,” *Radiation Protection and Environment*, vol. 44, no. 2, pp. 116-119, 2021.

7. Numerical Analysis of Characterized Skin Phantoms and SAR Evaluation**171**

- [8] T. J. Yoon, K. A. Maerzke, R. P. Currier, and A. T. Findikoglu, “PyOECP: A flexible open-source software library for estimating and modeling the complex permittivity based on the open-ended coaxial probe (OECP) technique,” 2021, [Online]: Available: <https://arxiv.org/abs/2109.14889>.
- [9] F. Fidanza, “Body fat in adult man: semicentenary of fat density and skinfolds,” *Acta Diabetol*, vol. 40, pp. S242-S245, October, 2003, doi: 10.1007/s00592-003-0076-0.

Chapter 8

Conclusion and Future Work

Skin cancer, the most common form of cancer, has been rising worldwide. Early detection and effective treatment is a key to improve the survival rate of patients. Currently, the skin cancer diagnosis relies mainly on the dermatologist's experience and pathological analysis of the excised samples.

To this aim, non invasive, non-ionizing and low power microwave techniques are of considerable interest to help dermatologists improve the diagnostic accuracy. Further, testing and performance evaluation of these microwave-based systems require experimental models that accurately mimic dielectric properties and anatomy of human tissues. These models provide controlled testing and repeatable environment.

Therefore, the presented study provided mathematical modeling and development of comprehensive set of phantoms for feasibility assessment of the emerging medical diagnostic devices. Moreover, to assess the interaction of electromagnetic fields with the human tissues and to perform the safety assessment of the probe, numerical modeling of dielectric properties

with different aperture sizes was performed. In this chapter, the overview of the thesis, summary of research performed and several recommendations for further research directions are presented.

8.1 Key Contributions

The key contributions of the work presented in this thesis are as follows:

- First, we presented consistent comparison of two types of skin-mimicking phantoms (Carbon-polyurethane based, fabricated in the lab and commercially available Probingon AB) in three different geometrical configurations (a thicker 20-mm block, thinner 2-mm sample and 2-mm skin placed on fat-mimicking phantom). It was observed that both the phantoms demonstrate dielectric properties within the range of human skin measurements and choice of phantom depends on different requirements like stability, dielectric accuracy, complexity, shape and application.
- In the next study, we explored a range of skin-tumor geometries presenting dielectric and anatomical representation of healthy and malignant human skin. We developed a comprehensive set of experimental phantoms where tumors were combined with skin at three different locations with tumor size variation from 2 mm to 10 mm and two different sizes of underlying skin. Further, tumor with irregular border was also developed. The dielectric measurements of fabricated phantoms presented acceptable representation of excised malignant BCC and SCC tissues obtained from literature.

Thus, in this work we provided a range of anatomical and dielectrically realistic phantoms with systematic variation in size, shape and location of tumor.

- Another aspect of our study was to realize selected skin lesions to assess the detection capability of emerging prototypes for skin cancer detection. Here, we investigated rare malignant skin lesions like liposarcoma (subcutaneous mass present in the fat layer underneath the skin) and nonsyndromic multiple basal cell carcinoma (multiple lesions at the same time). Also, to provide meaningful comparison between various phantoms, tumor-mimicking lesions were incorporated in two different skin mimicking phantoms with varying tumor-skin geometries. From the computed results, it was observed that the dielectric probe was not only able to identify these rarely occurring lesions but also lesions in different heterogeneous tumor-skin geometrical configurations.
- The next section presents the design of tumor progression model which is based on the radial and vertical growth patterns of the melanoma. We then, based on this model, developed tissue-mimicking phantoms at set time intervals and evaluated their dielectric properties using slim-form open-ended coaxial probe. We observed dielectric properties variability by moving the probe over the suspicious lesion and adjoining skin in the linear segment. In another experiment, we generated dielectric map by moving the probe over the suspicious lesion in grid format. It was observed that the probe was able to identify the variation in dielectric properties with variation in both radial and vertical growth. The results were further validated by comparing them with estimated

values of malignant melanoma using Lichtenecker's mixing reference model.

- In the last section, we observed the impact of the variability of skin thickness on dielectric measurements and estimated the sensing depth of the dielectric probe. Further, we simulated the dielectric probe terminated by a skin-fat model, where the skin thickness was varied 0.5 – 5 mm with 0.5 mm increments. It was observed that simulated results agreed well with the experimental results. Finally, we analyzed the effect of probe aperture size on the electromagnetic field distribution in the biological tissues and SAR values for safety assessment.

8.2 Discussion

A comprehensive set of different types of dielectrically realistic tissue-mimicking phantom models reflecting different geometrical combinations and more anatomically realistic scenarios was developed and analyzed with an aim to evaluate the detection limits of emerging microwave-based skin cancer diagnostic systems and eventually resulting in more effective system. Therefore, we focused our efforts in modeling the phantoms with homogeneous configurations of skin with varying thicknesses and then heterogeneous configurations of skin and tumor. The study includes tumors varying in size, shape and location, realization of rare conditions like non-syndromic basal cell carcinoma and liposarcoma. In addition, tumor models emulating malignant melanoma growth in terms of

radial and vertical growth was realized. Another focus of study was to evaluate the sensing depth and safety assessment of the probe in terms of specific absorption rate, which are important parameters to consider in design of any medical diagnostic systems.

Open-ended coaxial probe is the most suited and well adapted technique for microwave characterization of these phantoms for intended application of skin cancer diagnosis, than other techniques such as transmission line, resonant cavity and free-space methods due to number of advantages associated with it. First, this measurement method allows both *in vivo* and *ex vivo* measurements. Second, tissues mostly have semi-solid nature and coaxial probes are best to use with semi-solid materials. Third, by optimizing the probe dimensions and materials; intended sensitivity, sensing depth and lateral resolution can be acquired.

Obtained experimental results from different configurations suggest that the reflected signals provide specific information that on analysis helps in predicting the presence or absence, size, shape, location and malignancy of tumor. Also, the information embedded in signals tell about the vertical and radial growth of tumor by sensing the variation in dielectric properties with variation of thickness and diameter of tumor. Results from systematic investigation of skin thickness variation on dielectric properties implied that a diagnostic tool designed based on microwave skin spectroscopy can be effective irrespective of the skin thickness in contact with the measurement probe. Results analyzed advances the knowledge and understanding of microwave backscattered signals in discriminating malignant tissues from healthy tissues with respect to several configurations, thus, showing

the promise of using these phantoms in evaluation of the effectiveness of emerging microwave-based diagnostic systems.

Although results are promising, *in vivo* studies are required in order to extend microwave based diagnostic techniques from controlled laboratory experiments to clinical trials. Although phantoms provide repeatable base for systematic testing of system under controlled conditions, but measurements with patients is important as it takes into consideration, natural variations and complexity of tissues. Sensitivity of the device can be improved further by optimizing its dimension and materials.

8.3 Future Work

For the development of microwave-based skin cancer diagnostic prototype, there are many avenues worth exploring. Some of them are summarized as follows:

- Consideration of development of extensive database of dielectric properties of skin (healthy and malignant) for a range of patients. For development of accurate and reliable microwave-based skin cancer diagnostic systems, extensive database of healthy and malignant skin that includes dielectric response from a diverse group of patients with varying skin types, ages, and tumor types is required. Based on these dielectric responses, machine learning algorithms can be trained to better differentiate between healthy and malignant skin tissues. The database will also help improve understanding

of various skin conditions and phantom models precisely mimicking dielectric properties can be developed.

- To observe the difference in dielectric properties of tissues post-excision, large scale measurements on malignant lesions *in vivo* and *ex vivo* can be performed. The dielectric properties of *in vivo* tissues are expected to be different from *ex vivo* tissues due to number of reasons. This can be due to dehydration, temperature variation, time between excision (e.g., storage conditions), and measurement. Therefore, it is important to study dielectric variation between measurements done directly on patients and excised tissue samples.
- For the development of microwave-based tool for skin anomaly detection, there is a requirement of design and simulation of a sensing radiating element. This will overcome the limitations of dielectric probe, improving ease of use and portability. While dielectric probes have demonstrated excellent ability to distinguish between normal and malignant tissues, there are some limitations to their use. Based on the requirement of the system, sensing element can be designed for particular frequency range with high sensitivity, lateral resolution and desired sensing volume. Moreover, sensing radiating element can be optimized to obtain more patient-friendly, portable and cost-effective system.
- For further improvements of the system and result analysis, machine learning

algorithms can be incorporated. Machine learning algorithms trained to detect patterns of dielectric responses in large and complex datasets that may be difficult for humans to discern can revolutionize skin cancer diagnostic research by enabling more accurate predictions and earlier detection of tumors.

Bibliography

- [1] Cancer Facts & Figures, American Cancer Society, 2022, Accessed: July 8, 2022. [Online]. Available: <https://www.cancer.org/content/dam/cancer-org/research/cancer-facts-and-statistics/annual-cancer-facts-and-figures/2022/2022-cancer-facts-and-figures.pdf/>
- [2] Skin Cancer, American Academy of Dermatology Association, 2022, Accessed: July 8, 2022. [Online]. Available: <https://www.aad.org/media/stats-skin-cancer>
- [3] Skin Cancer Facts & Statistics, Skin Cancer Foundation, 2022, Accessed: July 8, 2022. [Online]. Available: <https://www.skincancer.org/skin-cancer-information/skin-cancer-facts/>
- [4] Cancer Stat Facts: Melanoma of the Skin, National Cancer Institute, 2022, Accessed: July 8, 2022. [Online]. Available: <https://seer.cancer.gov/statfacts/html/melan.html>
- [5] P. Mehta, K. Chand, D. Narayanswamy, D. G. Beetner, R. Zoughi, and W. V. Stoecker, “Microwave reflectometry as a novel diagnostic tool for detection of skin cancers,”

- Transactions on Instrumentation and Measurement*, vol. 55, no. 4, pp. 1309-1316, 2006, doi: 10.1109/TIM.2006.876566.
- [6] Skin Cancer, Centers for Disease Control and Prevention, Accessed: July 8, 2022. [Online]. Available: https://www.cdc.gov/cancer/skin/basic_info/screening.htm
- [7] Skin Cancer: Screening U.S. Preventive Services Task Force, Accessed: July 8, 2022. [Online]. Available: <https://www.uspreventiveservicestaskforce.org/uspstf/recommendation/skin-cancer-screening>
- [8] A. W. Kopf, M. Mintzis, and R. S. Bart, "Diagnostic Accuracy in Malignant Melanoma," *Archives of Dermatology*, vol. 111, no. 10, pp. 1291-1292, 1975, doi: 10.1001/archderm.1975.01630220055001.
- [9] A. C. Kak and M. Slaney, "Principles of computerized tomographic imaging," in *Classics in Applied Mathematics*, R. F. Cotellessa, Ed., New York, NY, USA: IEEE Press, 1988.
- [10] N. Ghavami, G. Tiberi, M. Ghavami, S. Dudley, and M. Lane, "Huygens principle based UWB microwave imaging method for skin cancer detection," in *2016 10th International Symposium on Communication Systems, Networks and Digital Signal Processing (CSNDSP)*, 20-22 July 2016, pp. 1-4, doi: 10.1109/CSNDSP.2016.7573969.
- [11] I. Iliopoulos, S. D. Meo, M. Pasian, M. Zhadobov, P. Pouliguen, P. Potier, L. Perregrini, R. Sauleau, M. Ettorre, "Enhancement of Penetration of Millimeter Waves by

- Field Focusing Applied to Breast Cancer Detection,” *IEEE Transactions on Biomedical Engineering*, vol. 68, no. 3, pp. 959-966, 2021, doi: 10.1109/TBME.2020.3014277.
- [12] F. Töpfer, L. Emtestam, and J. Oberhammer, “Diagnosis of malignant melanoma by micromachined near-field millimeter-wave probe,” in *2016 41st International Conference on Infrared, Millimeter, and Terahertz waves (IRMMW-THz)*, 25-30 Sept. 2016, pp. 1-2, doi: 10.1109/IRMMW-THz.2016.7758369.
- [13] A. Mirbeik-Sabzevari, R. Ashinoff, and N. Tavassolian, “Ultra-Wideband Millimeter-Wave Dielectric Characteristics of Freshly Excised Normal and Malignant Human Skin Tissues,” *IEEE Transactions on Biomedical Engineering*, vol. 65, no. 6, pp. 1320-1329, Jun 2018, doi: 10.1109/tbme.2017.2749371.
- [14] E. C. Fear, J. Bourqui, C. Curtis, D. Mew, B. Docktor, and C. Romano, “Microwave Breast Imaging With a Monostatic Radar-Based System: A Study of Application to Patients,” *IEEE Transactions on Microwave Theory and Techniques*, vol. 61, no. 5, pp. 2119-2128, 2013, doi: 10.1109/TMTT.2013.2255884.
- [15] A. Zamani, S. A. Rezaeieh, and A. M. Abbosh, “Lung cancer detection using frequency-domain microwave imaging,” *Electronics Letters*, vol. 51, no. 10, pp. 740-741, 2015.
- [16] S. Y. Semenov and D. R. Corfield, “Microwave Tomography for Brain Imaging: Feasibility Assessment for Stroke Detection,” *International Journal of Antennas and Propagation*, 2008.

- [17] J. Kanitakis, "Anatomy, histology and immunohistochemistry of normal human skin," *European Journal of Dermatology*, vol. 12, no. 4, pp. 390-399, quiz 400-1, Jul-Aug 2002.
- [18] P. A. J. Kolarsick, M. A. Kolarsick, and C. Goodwin, "Anatomy and Physiology of the Skin," *Journal of the Dermatology Nurses' Association*, vol. 3, no. 4, pp. 203-213, 2011, doi: 10.1097/JDN.0b013e3182274a98.
- [19] Medscape, Skin Anatomy, Overview, Accessed: 19 July 2022. [Online]. Available: <https://emedicine.medscape.com/article/1294744-overview?reg=1>
- [20] National Cancer Institute, Visuals Online, Skin, Accessed: 19 July 2022. [Online]. Available: <https://visualsonline.cancer.gov/details.cfm?imageid=1809>
- [21] J. L. Leveque, P. Corcuff, J. de Rigal, and P. Agache, "In vivo studies of the evolution of physical properties of the human skin with age," *International Journal of Dermatology*, vol. 23, no. 5, pp. 322-329, Jun 1984, doi: 10.1111/j.1365-4362.1984.tb04061.x.
- [22] P. Oltulu, B. Ince, N. Kokbudak, S. Findik, F. Kilinc, "Measurement of epidermis, dermis, and total skin thicknesses from six different body regions with a new ethical histometric technique," *Turkish Journal of Plastic Surgery*, vol. 26, no. 2, pp. 56-61, 2018, doi: 10.4103/tjps.TJPS_2_17.

- [23] R. Y. Ha, K. Nojima, W. P. Adams, Jr., and S. A. Brown, "Analysis of facial skin thickness: defining the relative thickness index," *Plastic and Reconstructive Surgery*, vol. 115, no. 6, pp. 1769-1773, May 2005, doi: 10.1097/01.prs.0000161682.63535.9b.
- [24] Dermatology, Anatomy of the Skin, Accessed: 19 July 2022. [Online]. Available: https://www.utmb.edu/pedi_ed/CoreV2/Dermatology/page_03.htm
- [25] H. Yousef, M. Alhajj, S. Sharma, "Anatomy, Skin (Integument), Epidermis," [Updated 2021 Nov 19]. In: StatPearls [Internet]. Treasure Island (FL): StatPearls Publishing; Jan. 2022. Available from: <https://www.ncbi.nlm.nih.gov/books/NBK470464/>
- [26] Y. Gao, M. T. Ghasr, M. Nacy, and R. Zoughi, "Towards Accurate and Wideband In Vivo Measurement of Skin Dielectric Properties," *IEEE Transactions on Instrumentation and Measurement*, vol. 68, no. 2, pp. 512-524, Feb 2019, doi: 10.1109/TIM.2018.2849519.
- [27] National Cancer Institute, What is Cancer?, Accessed: 19 July 2022. [Online]. Available: <https://www.cancer.gov/about-cancer/understanding/what-is-cancer>
- [28] American Cancer Society, What are Basal and Squamous Cell Skin Cancers? Accessed: 19 July 2022. [Online]. Available: <https://www.cancer.org/cancer/basal-and-squamous-cell-skin-cancer/about/what-is-basal-and-squamous-cell.html>
- [29] Cancer Quest, Skin Cancer, Accessed: 19 July 2022. [Online]. Available: <https://www.cancerquest.org/patients/cancer-type/skin-cancer>

- [30] T. D. Wortman, “LesionAir: a low-cost tool for automated skin cancer diagnosis and mapping,” (Doctoral dissertation, Massachusetts Institute of Technology), June 2016.
- [31] Skin Cancer Foundation, Squamous Cell Carcinoma Overview, Accessed: 19 July 2022. [Online]. Available: <https://www.skincancer.org/skin-cancer-information/squamous-cell-carcinoma/>
- [32] American Academy of Dermatology Association, Skin Cancer Types: Squamous Cell Carcinoma Overview,” Accessed: 19 July 2022. [Online]. Available: <https://www.aad.org/public/diseases/skin-cancer/types/common/scc>.
- [33] American Cancer Society, What is Melanoma Skin Cancer?, Accessed: 19 July 2022. [Online]. Available: <https://www.cancer.org/cancer/melanoma-skin-cancer/about/what-is-melanoma.html>
- [34] Canadian Cancer Society, Types of melanoma skin cancer, Accessed: 19 July 2022. [Online]. Available: <https://cancer.ca/en/cancer-information/cancer-types/skin-melanoma/what-is-melanoma/types-of-melanoma>
- [35] W. H. Clark, Jr., L. From, E. A. Bernardino, and M. C. Mihm, “The histogenesis and biologic behavior of primary human malignant melanomas of the skin,” *Cancer Research*, vol. 29, no. 3, pp. 705-727, March 1969.

- [36] A. Breslow, "Thickness, cross-sectional areas and depth of invasion in the prognosis of cutaneous melanoma," *Annals of Surgery*, vol. 172, no. 5, pp. 902-908, Nov 1970, doi: 10.1097/00000658-197011000-00017.
- [37] C. Garbe, K. Peris, A. Hauschild, P. Saiag, M. Middleton, A. Spatz, J. Grob, J. Malvehy, J. Newton-Bishop, A. Stratigos, H. Pehamberger, A. Eggermont, "Diagnosis and treatment of melanoma: European consensus-based interdisciplinary guideline," *European Journal of Cancer*, vol. 46, no. 2, pp. 270-283, Jan 2010, doi: 10.1016/j.ejca.2009.10.032.
- [38] R. P. Braun, J. Mangana, S. Goldinger, L. French, R. Dummer, and A. A. Marghoob, "Electrical Impedance Spectroscopy in Skin Cancer Diagnosis," *Dermatologic Clinic*, vol. 35, no. 4, pp. 489-493, Oct 2017, doi: 10.1016/j.det.2017.06.009.
- [39] J. Dinnes et al., "Dermoscopy, with and without visual inspection, for diagnosing melanoma in adults," *Cochrane Database Syst Rev*, vol. 12, no. 12, p. CD011902, Dec 2018, doi: 10.1002/14651858.cd011902.pub2.
- [40] A. Mirbeik-Sabzevari and N. Tavassolian, "Tumor Detection Using Millimeter-Wave Technology: Differentiating Between Benign Lesions and Cancer Tissues," *IEEE Microwave Magazine*, vol. 20, no. 8, pp. 30-43, August 2019, doi: 10.1109/MMM.2019.2915472.

- [41] H. D. Heibel, L. Hooey, and C. J. Cockerell, "A Review of Noninvasive Techniques for Skin Cancer Detection in Dermatology," *American Journal of Clinical Dermatology*, vol. 21, no. 4, pp. 513-524, Aug 2020, doi: 10.1007/s40257-020-00517-z.
- [42] S. R. M. Shah, N. B. Asan, J. Velandar, J. Ebrahimizadeh, M. D. Perez, V. Mattsson, T. Blokhuis and R. Augustine, "Analysis of Thickness Variation in Biological Tissues Using Microwave Sensors for Health Monitoring Applications," *IEEE Access*, vol. 7, pp. 156033-156043, 2019, doi: 10.1109/ACCESS.2019.2949179.
- [43] M. Lazebnik et al., "A large-scale study of the ultrawideband microwave dielectric properties of normal, benign and malignant breast tissues obtained from cancer surgeries", *Physics in Medicine and Biology*, vol. 52, no. 20, pp. 6093-6115, Oct. 2007.
- [44] T. Sugitani, S. Kubota, S. Kuroki, K. Sogo, K. Arihiro, M. Okada, T. Kadoya, M. Hide, M. Oda and T. Kikkawa, "Complex permittivities of breast tumor tissues obtained from cancer surgeries", *Applied Physics Letters*, vol. 104, no. 25, pp. 253702, June 2014.
- [45] A. Fornes-Leal, C. Garcia-Pardo, M. Frasson, V. Pons Beltrán and N. Cardona, "Dielectric characterization of healthy and malignant colon tissues in the 0.5-18 GHz frequency band", *Physics in Medicine and Biology*, vol. 61, no. 20, pp. 7334-7346, 2016.
- [46] A. P. O'Rourke, M. Lazebnik, J. M. Bertram, M. C. Converse, S. C. Hagness, J. G. Webster, D. M. Mahvi, "Dielectric properties of human normal, malignant and cirrhotic

- liver tissue: in vivo and ex vivo measurements from 0.5 to 20GHz using a precision open-ended coaxial probe,” *Physics in Medicine and Biology*, vol. 52, pp. 4707–4719, 2007.
- [47] H. Choi, J. Nylon, S. Luzio, J. Beutler, J. Birchall, C. Martin and A. Porch, ”Design and in vitro interference test of microwave noninvasive blood glucose monitoring sensor”, *IEEE Transactions on Microwave Theory and Techniques*, vol. 63, no. 10, pp. 3016-3025, Oct. 2015.
- [48] A. Cataldo *et al.*, ”Portable Microwave Reflectometry System for Skin Sensing,” *IEEE Transactions on Instrumentation and Measurement*, vol. 71, pp. 1-8, 2022, Art no. 4003308, doi: 10.1109/TIM.2022.3154804.
- [49] Y. Hayashi, N. Miura, N. Shinyashiki and S. Yagihara, ”Free water content and monitoring of healing processes of skin burns studied by microwave dielectric spectroscopy in vivo”, *Physics in Medicine and Biology*, vol. 50, no. 4, pp. 599-612, Jan. 2005.
- [50] A. Taeb, S. Gigoyan and S. Safavi-Naeini, ”Millimetre-wave waveguide reflectometers for early detection of skin cancer”, *IET Microwaves, Antennas and Propagation*, vol. 7, no. 14, pp. 1182-1186, Nov. 2013.
- [51] F. Topfer and J. Oberhammer, ”Millimeter-wave tissue diagnosis: The most promising fields for medical applications”, *IEEE Microwave Magazine*, vol. 16, no. 4, pp. 97-113, 2015.

- [52] H. N. Mayrovitz, S. R. Gildenberg, P. Spagna, L. Killpack and D. A. Altman, "Characterizing the tissue dielectric constant of skin basal cell cancer lesions", *Skin Research and Technology*, vol. 24, no. 4, pp. 686-691, Nov. 2018.
- [53] A. L. Gioia, E. Porter, I. Merunka, A. Shahzad, S. Salahuddin, M. Jones, M. O'Halloran, "Open-Ended Coaxial Probe Technique for Dielectric Measurement of Biological Tissues: Challenges and Common Practices," *Diagnostics*, vol. 8, no. 2, 2018, doi: 10.3390/diagnostics8020040.
- [54] F. Töpfer, L. Emtestam, and J. Oberhammer, "Long-Term Monitoring of Skin Recovery by Micromachined Microwave Near-Field Probe," *IEEE Microwave and Wireless Components Letters*, vol. 27, no. 6, pp. 605–607, 2017.
- [55] A. La Gioia, "Accurate dielectric characterisation of biological tissues in the microwave range using the open-ended coaxial probe technique," (Doctoral dissertation, NUI Galway), 2019.
- [56] K. Shibata, K. Tani, O. Hashimoto, et al., Measurement of Complex Permittivity for Liquid Phantom by Transmission Line Method Using Coaxial Line," *IEICE Transactions on Electronics*, vol. 87-C, no. 5, pp. 689-693, 2004.
- [57] T. Reinecke, L. Hagemeyer, V. Schulte, et al., Quantification of Edema in Human Brain Tissue by Determination of Electromagnetic Parameters," in *IEEE Sensors*, Baltimore, MD, 2013, pp. 1-4.

- [58] S. Begley, Electromagnetic Properties of Materials: Characterization at Microwave Frequencies and Beyond, Accessed: 19 July 2022. [Online]. Available: <https://player.slideplayer.com/5/1526640/#>
- [59] Keysight Technologies, Basics of Measuring the Dielectric Properties of Materials, Accessed: 19 July 2022. [Online]. Available: https://www.cmc.ca/wp-content/uploads/2019/08/Basics_Of_MeasuringDielectrics_5989-2589EN.pdf
- [60] Speag, DAK (4 MHz – 67 GHz), Accessed: 03 March 2022. [Online]. Available:<https://speag.swiss/products/dak/dak-probes/>
- [61] A. Campbell and D. V. Land, “Dielectric properties of female human breast tissue measured in vitro at 3.2 GHz,” *Physics in medicine and biology*, vol. 37, no. 1, pp. 193-210, 1992.
- [62] IEEE Standard for safety levels with respect to human exposure to radio frequency electromagnetic fields 3 kHz to 300 GHz. IEEE International Committee on Electromagnetic Safety (SCC 39); 2005.
- [63] International Commission on Non-Ionizing Radiation Protection (ICNIRP), “Guidelines for limiting exposure to time varying electric, magnetic and electromagnetic fields (up to 300 GHz)”. *Health physics*, 1998; 74(4): 494–522.

[64] FCC, "In the Matter of Reassessment of Federal Communications Commission Radio Frequency Exposure Limits and Policies," FCC 13–39, March 2013.

[65] Specific Absorption Rate (SAR) Information, Accessed: 19 July 2022. [Online]. Available: <https://support.realwear.com/knowledge/specific-absorption-rate-sar-information>